1-1-2017

Identifying the Relevance of C-Reactive Protein Conformers and the Advancement of a Membrane Curvature Binding Assay

Carrie Leine Moon
University of Denver

Identifying the Relevance of C-Reactive Protein Conformers and the Advancement of a Membrane Curvature Binding Assay

Abstract

Lipid membranes play a vital role in cell signaling processes. Membrane shape and lipid content affect interactions between cellular membranes and proteins. This research focuses on characterizing those interactions and their impact by using various biochemical and biophysical assays. These assays were applied to C-reactive protein (CRP), an immune system protein that interacts with lipid membranes and has at least two forms with different properties. Native, pentameric CRP (pCRP) is found in blood serum and is commonly used as a marker for inflammation. The modified form of CRP (mCRP) binds to the protein C1q, which activates the complement immune response. There is a gap in our knowledge of the biochemical information for the two forms of CRP and several different methods are used to make mCRP in the lab. In this work, we analyzed the pCRP to mCRP conversion using three biochemical denaturants: guanidine hydrochloride, urea with ethylenediaminetetraacetic acid (EDTA), and heating with dilute sodium dodecyl sulfate (SDS). After comparing results from biochemical assays to determine structural and functional differences, mCRP treated with dilute SDS and heat was the form that both significantly bound C1q and had an intrinsic tryptophan fluorescence level as anticipated for an intermediate form.

After characterizing biochemical differences between functional mCRP and native pCRP forms, binding of pCRP and mCRP to curved membranes was analyzed with an in vitro membrane mimic assay that starts with a nanoscale pattern on a glass coverslip to create curvature for a supported lipid bilayer to coat. By using fluorescent nanoparticles of a specific size, curvature based interactions can be visualized and quantified. Results show that the amount of CRP binding is not only dependent on protein conformation but also on membrane curvature size.

Expanding the membrane curvature assay, used to visualize CRP membrane binding, to allow for cellular experiments was achieved by first melting the nanoparticles and then coating them with silicon dioxide, creating a permanent nanoparticle patterned substrate. Custom chambers were created and added to the nanoparticle patterned coverglass to reduce the required volume. Characterizations of the silicon dioxide coated surface were done with analysis of fluorescent lipids in supported lipid bilayers. The assays and results from this research not only contribute to better biochemical knowledge of CRP, but will be useful for future studies of proteins involved in cellular processes that have membrane interactions.

Document Type

Dissertation

Degree Name

Ph.D.

Department

Chemistry and Biochemistry

First Advisor

Michelle K. Knowles, Ph.D.

Keywords

Biophysics, Cell signaling processes, C-reactive protein

IDENTIFYING THE RELEVANCE OF C-REACTIVE PROTEIN CONFORMERS AND THE ADVANCEMENT OF A MEMBRANE CURVATURE BINDING ASSAY

_____

A Dissertation

Presented to

the Faculty of Natural Sciences and Mathematics

University of Denver

_____

In Partial Fulfillment

of the Requirements for the Degree

Doctor of Philosophy

_____

by

Carrie L. Moon

June 2017

Advisor: Michelle K. Knowles

Author: Carrie L. Moon
Title: IDENTIFYING THE RELEVANCE OF C-REACTIVE PROTEIN CONFORMERS AND THE ADVANCEMENT OF A MEMBRANE CURVATURE BINDING ASSAY
Advisor: Michelle K. Knowles
Degree Date: June 2017

ABSTRACT

Lipid membranes play a vital role in cell signaling processes. Membrane shape and lipid content affect interactions between cellular membranes and proteins. This research focuses on characterizing those interactions and their impact by using various biochemical and biophysical assays. These assays were applied to C-reactive protein (CRP), an immune system protein that interacts with lipid membranes and has at least two forms with different properties. Native, pentameric CRP (pCRP) is found in blood serum and is commonly used as a marker for inflammation. The modified form of CRP (mCRP) binds to the protein C1q, which activates the complement immune response. There is a gap in our knowledge of the biochemical information for the two forms of CRP and several different methods are used to make mCRP in the lab. In this work, we analyzed the pCRP to mCRP conversion using three biochemical denaturants: guanidine hydrochloride, urea with ethylenediaminetetraacetic acid (EDTA), and heating with dilute sodium dodecyl sulfate (SDS). After comparing results from biochemical assays to determine structural and functional differences, mCRP treated with dilute SDS and heat was the form that both significantly bound C1q and had an intrinsic tryptophan fluorescence level as anticipated for an intermediate form.

After characterizing biochemical differences between functional mCRP and native pCRP forms, binding of pCRP and mCRP to curved membranes was analyzed with an *in vitro* membrane mimic assay that starts with a nanoscale pattern on a glass

coverslip to create curvature for a supported lipid bilayer to coat. By using fluorescent nanoparticles of a specific size, curvature based interactions can be visualized and quantified. Results show that the amount of CRP binding is not only dependent on protein conformation but also on membrane curvature size.

Expanding the membrane curvature assay, used to visualize CRP membrane binding, to allow for cellular experiments was achieved by first melting the nanoparticles and then coating them with silicon dioxide, creating a permanent nanoparticle patterned substrate. Custom chambers were created and added to the nanoparticle patterned coverglass to reduce the required volume. Characterizations of the silicon dioxide coated surface were done with analysis of fluorescent lipids in supported lipid bilayers. The assays and results from this research not only contribute to better biochemical knowledge of CRP, but will be useful for future studies of proteins involved in cellular processes that have membrane interactions.

ACKNOWLEDGEMENTS

I would like to thank Dr. Michelle Knowles for her excellent guidance and mentorship during my doctoral degree. Additionally, her expertise with microscopy and overall scientific knowledge enhanced the research presented here. I am grateful to my defense committee, Dr. Joseph Angleson, Dr. Dinah Loerke, and Dr. David Patterson, and my chair, Dr. Matthew Gordon, for their thoughtful input and encouragement. I would also like to thank Dr. John Latham for his assistance with Chimera and Dr. Xin Fan for sputter coating our samples. With appreciation, I acknowledge Dr. Scott Barbee for a valuable rotation project with molecular biology research of Fragile X syndrome. The research presented here and the writing benefitted from collaborations, ideas, and edits from countless professors and fellow graduate students at the University of Denver in the departments of Chemistry and Biochemistry, Biology, and Physics and Astronomy. With gratitude, I acknowledge their assistance and the wonderfully collaborative nature of the Molecular and Cellular Biophysics Program.

TABLE OF CONTENTS

LIST OF TABLES

LIST OF FIGURES

LIST OF ABBREVIATIONS

ABS ..... acrylonitrile butadiene styrene

AFM ..... atomic force microscopy

ANS ..... 1-anilinonaphthalene-8-sulfonic acid

APS ..... ammonium persulfate

Biotin-X-DHPE ..... N-((6-(biotinoyl)amino)hexanoyl)-1,2-dihexadecanoyl-sn-glycero-3-phosphoethanolamine

BSA ..... bovine serum albumin

CD ..... circular dichroism

Chol ..... cholesterol

CRP ..... C-reactive protein

CVD ..... cardiovascular disease

DLS ..... dynamic light scattering

EDTA ..... ethylenediaminetetraacetic acid

ELISA ..... enzyme linked immunosorbent assay

FL-DHPE ..... fluorescein 1,2-dihexadecanoyl-sn-glycero-3-phosphoethanolamine

FRAP ..... fluorescence recovery after photobleaching

GndHCl ..... guanidine hydrochloride

HEPES ..... 4-(2-hydroxyethyl)-1-piperazineethanesulfonic acid

HRP-Strep ..... streptavidin linked horse radish peroxidase

LDL ..... low density lipoprotein

lysoPC ..... lysophosphatidylcholine

MB-DHPE ..... marina blue 1,2-dihexadecanoyl-sn-glycero-3-phosphoethanolamine

mCRP ..... modified C-Reactive protein

PAGE ..... polyacrylamide gel electrophoresis

PBS ..... phosphate buffered saline

PBST ..... phosphate buffered saline with Tween-20

PC ..... phosphatidylcholine

pCRP ..... pentameric C-reactive protein

PEG ..... polyethylene glycol

PETG ..... polyethylene terephthalate

PIPES ..... piperazine-N,N′-bis(2-ethanesulfonic acid)

PLA ..... polylactic acid

POPC 1-palmitoyl-2-oleoyl-sn-glycero-3-phosphocholine

R_g ..... radius of gyration

R_H ..... hydrodynamic radius

ROC ..... radius of curvature

ROI ..... region of interest

R.T. ..... room temperature

SB-DHPE ..... Strep-Biotin-X-DHPE

SDS ..... sodium dodecyl sulfate

SEM ..... standard error of the mean

SLB ..... supported lipid bilayer

TIRF ..... total internal reflection fluorescence

TMB ..... 3,3’,5,5’-tetramethylbenzidine

Trp ..... tryptophan

CHAPTER ONE: INTRODUCTION

Molecular interactions on a cellular level are directly related to function. While some molecular interactions have been well studied and characterized, others still need extensive research. Of particular interest are interactions between immune system proteins and cells or bacteria that cause a clearance response. Improper clearance can be the cause of health problems, e.g. the buildup of atherosclerotic plaque leading to heart disease. Besides immune pathways, there are other pathways in the cell that are dependent on protein and membrane interactions. Examples include clathrin-dependent endocytosis, the SNARE protein complex interacting with synaptic vesicles, and the binding of microtubule associated proteins. Working to understand the steps of cellular pathways on a molecular level not only increases biochemical knowledge, but also brings medical insight that can lead to future treatments for diseases impacted by interaction problems.

In this work, the binding interactions of C-reactive Protein (CRP), a member of the innate complement immune response, were characterized. CRP interacts both with lipid membranes and protein partners, and all these interactions depend on the conformational state of CRP. To assess these interactions, it was first necessary to determine a method for making a modified CRP conformational state in the lab. This CRP conformer was characterized and tested for biological relevance using a protein binding assay. To identify CRP-lipid interactions, the two CRP conformational states

were used in a membrane curvature binding assay with different curvature sizes and lipid compositions. Beyond the characterization of CRP interactions, the work herein describes advancements to the curved membrane binding assay, specifically the addition of custom made chambers reducing the volume and the use of silicon dioxide coated melted nanoparticles for permanency. These substrates can be used for both supported lipid bilayers and for cellular assays in future research projects.

1.1 Lipids and Membranes

Lipids play an important role in cellular and organelle membranes both functionally and structurally. Model membranes are commonly used to study lipid and membrane properties. Each lipid membrane assay used in the lab can be broken down into one of three formation categories: micelles, liposomes, and bilayers, the third category applies to the work presented here. An early assay for lipid studies is Langmuir's film balance for measuring surface tension (1). Initial work with liposomes, originally referred to as phospholipid spherules, focused on how steroids, antibiotics, detergents, etc. would either stabilize or disrupt the liposome structures (2).

While preliminary studies focused on characterizing lipid membranes, usually from methods that involved fractionating cells (3), current research utilizes bilayers and liposomes with both cellular and artificial membranes to study the interactions of those membranes. Advancements in cellular membrane isolation have allowed for most of the plasma membrane proteins and lipids to remain intact. One technique involves starting with cells that have been stuck to a glass surface and then disrupting them with a sonicator so that sheets of plasma membrane are left behind and other cellular

components are washed off (4). Since transmembrane proteins are still present, it is possible to use this model to do assays of complex membrane functions, such as endocytosis (4).

Although the membrane sheet model is useful for assays that require transmembrane proteins and various lipids to be present, the complexity of the cell membrane can make it difficult to identify the exact lipid-protein interaction that is taking place. Simple lipid bilayers can be made using a technique referred to as supported lipid bilayers (SLB). The process starts with creating liposomes out of the lipid mixture and depositing them onto a surface, a process that depends on the conditions and charge of the vesicle (5). If specific sizes of liposomes are needed, lipids are extruded through polycarbonate membrane filters (6). Different conditions can cause the liposomes to split open and lay flat so they form a bilayer when attaching to the surface, to form a vesicular layer, or to fail to attach. Although the term attach is being used to describe the liposomes and SLB interacting with the surface, there is a small layer of water ranging from 0.5-1 nm cushioning the lipids (7). Calcium ion concentration is important for negatively charged and zwitterionic liposomes to form SLBs (5). To introduce features into bilayers, SLBs can be formed on top of flat cover plates, lithographed textured surfaces, and plates that have areas with nanoparticles (either set on top or partially melted onto the surface) (8, 9). These options for studying flat and curved interactions, as well as the ability to vary the lipid mixture and proteins present, make SLBs a versatile tool for studying interactions between curved membranes, lipid composition, and/or proteins.

1.2 Protein-Lipid and Lipid-Membrane Interactions

Interactions being studied between proteins and membranes with a SLB type of assay usually involve peripheral membrane proteins, which interact with the cell membrane surface either through specific headgroup binding or through insertion of the peripheral protein into the membrane (hydrophobic interactions). Binding of certain peripheral proteins to specific lipids can cause activation or inhibition of cellular processes (10).

Besides SLB membrane assays, other assays used to study protein-lipid interactions include surface plasmon resonance, circular dichroism, electron paramagnetic resonance spectroscopy, and Fourier transform infrared spectroscopy (11). Fluorescence techniques can also be used for studying peripheral membrane protein interactions with lipids. Fluorescence recovery after photobleaching (FRAP) on lipid tethers from giant unilamellar vesicles has been used to study interactions of endophilin, an N-BAR domain protein involved in clathrin-mediated endocytosis, with curvature on a tubular membrane (12).

The idea that BAR domains and other peripheral membrane proteins can sense regions of curvature suggests that there are specific regions where certain lipids and proteins are favored. Lipid and protein sorting can be attributed to lipid microdomains or membrane shape. Lipid rafts were originally envisioned as a way to explain the delivery of lipids selectively to the apical or basolateral surfaces of an epithelial cell (13). Lipid raft models are usually done on a larger scale to study their effect; however, in cells, lipid rafts are proposed to be less than 10 nm in diameter. Despite these differences, both *in*

vitro and *in vivo* models have benefitted from the idea of lipid rafts for studying lipid domains, which have high concentrations of cholesterol and sphingolipids.

One proposed mechanism for lipid sorting into microdomains as well as areas of curvature is by the intrinsic shape of the molecule, based on the concept that molecules will favor locations where they minimize loss of energy due to spaces between lipids. A lipid may favor a particular curvature based on head or tail shape or size as seen in studies of simulated self-assembly of lipids with different head sizes (14). Despite these calculations, other research has not shown lipid sorting based on molecular shape (15). There is a proposed mechanism of proteins recognizing defects in the lipid membrane, which are found at regions of curvature, with the example of crescent-shaped BAR domains binding at curved membranes (16).

1.3 C-Reactive Protein

Besides BAR domains, there are many other proteins that bind to membranes as part of cellular processes. One such protein is C-reactive protein (CRP), an immune system protein involved in inflammation and clearance. CRP has been shown to bind to lipids on highly curved low density lipoprotein (LDL) mimics made from liposome coated gold nanoparticles (17). Binding of CRP to LDL in the body would likely activate the classical complement pathway, tagging LDL for clearance.

1.3.1 CRP and the Classical Complement Immune Response

Due to its role in the classical complement pathway and apoptosis, it is not surprising that CRP is found all over the body, despite being produced mainly in hepatocyte cells. Normal levels of CRP are considered to be around 0.8 mg/L, however,

during inflammation CRP levels can increase rapidly and reach 1000 fold in 48 hours (18). When bacteria or apoptotic cells are present, the circulating CRP binds to their cell membranes. CRP has established interactions with phosphocholine, which is found on a number of bacterial and eukaryotic membranes (19). CRP is known to bind to apoptotic cells in the presence of Ca^{2+}, and C1q, a protein with a collagen-like stem and six head groups (20), is required for clearance of those cells (21). When C1q binds to CRP, the classic complement pathway (Figure 1) is activated, ending with the membrane attack complex creating pores in the membrane allowing the flow of fluid and ions and the cell to lyse (19, 20).

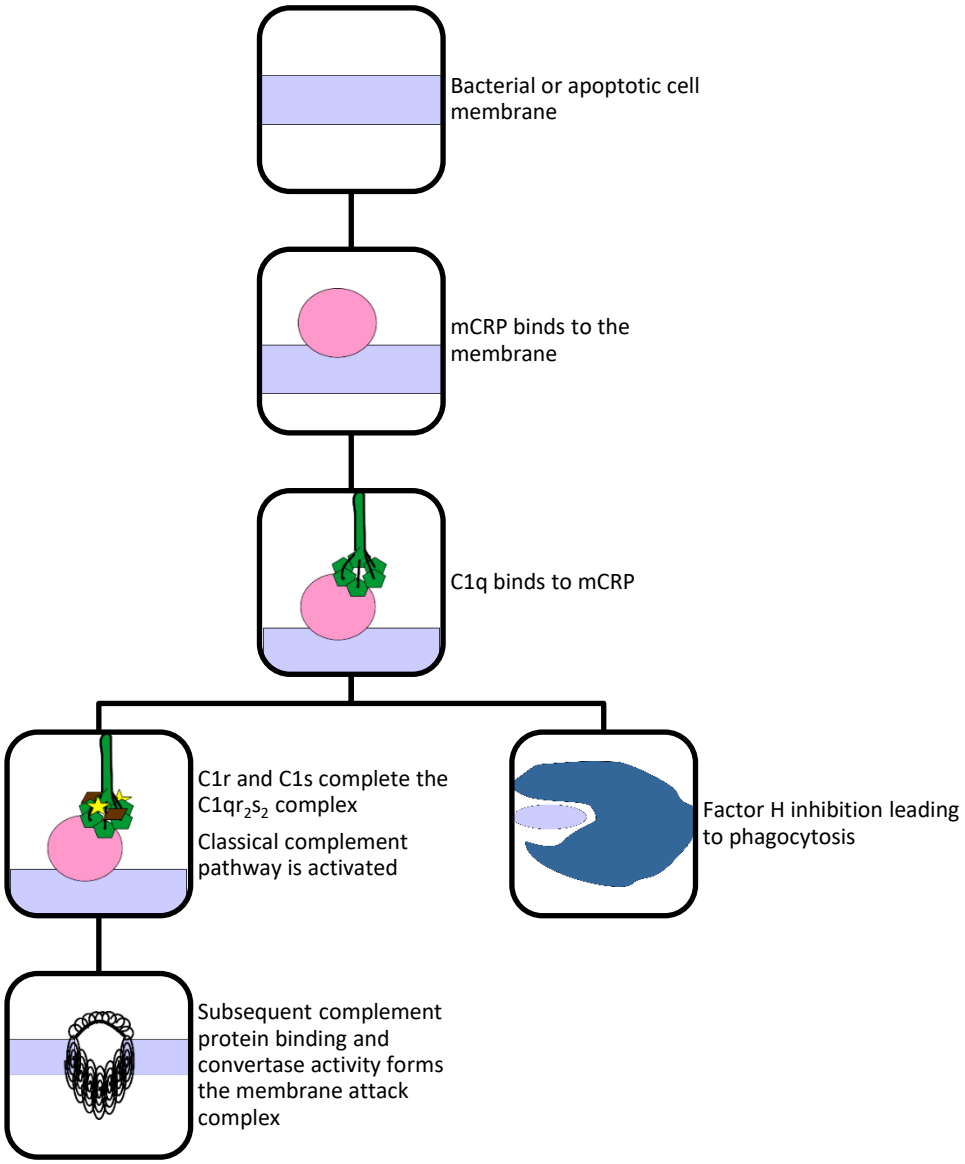

Figure 1. Diagram overview of the classical complement pathway with CRP activation. CRP first binds to the membrane and then recruits C1q. Once the rest of the C1complex binds, the classical complement pathway is activated, ending with cell lysis from the membrane attack complex (20). *Factor H inhibits the classical complement pathway and leads to the alternative pathway, ending in phagocytosis.*

Beyond this role with C1q in the classical complement pathway, CRP has been found to promote phagocytosis (functioning as an opsonin) through recruitment of Factor H, which is a regulator of the complement system (22). CRP gene expression is regulated

by interleukin-6 (IL-6), which controls the expression of many acute phase proteins. CRP has pro-inflammatory and anti-inflammatory features, which are predicted to be from the pentameric (pCRP) and modified (mCRP) conformers, respectively (23, 24). With the multiple features of CRP, it is no surprise that in addition to being produced in hepatocyte cells, CRP synthesis has been discovered in atherosclerotic plaques, lymphocytes, monocytes, and neurons.

1.3.2 CRP and Cardiovascular Disease

Of all the areas of the body where CRP is found, the location of atherosclerotic plaque is of particular interest due to a link between high CRP levels and cardiovascular disease (CVD) risk (19, 25, 26). Elevated CRP levels can be caused by acute infection or a chronic illness. If the inflammation decreases with time or treatment, the CRP levels should return to a normal range. Inflammation of the endothelium can cause atherosclerosis due to the expression of adhesion molecules (27), indicating that some types of inflammation can trigger plaque formation. Furthermore, some treatments for CVD, such as statins to lower cholesterol, have been shown to decrease inflammatory markers such as CRP.

Inflammation is a major part of atherosclerosis, regulating the protective fibrous cap and the plaque thrombogenicity (27–29). Atherosclerotic plaque contains the mCRP conformer, as measured by antibodies that bind specifically to the modified form. In contrast, healthy vessels have neither form of CRP, and pCRP is found in serum (23). Research suggests that conversion of pCRP to mCRP is localized to inflamed endothelia, and plays a vital role in atherogenesis (30). A necessary process of clearing LDL from

plaques involves the transformation of macrophages into foam cells. CRP has been found to assist macrophages in taking up native LDL and becoming foam cells (31). Initially a rise in CRP levels should help clear atherosclerotic plaques. However, if the recruitment of Factor H by CRP is high, then C3 convertase formation will be blocked, which prevents the membrane attack complex from being formed as well as opsonins (20). This prevention may leave cells in a necrotic or semi-apoptotic state without phagocytosis to completely clear out debris.

CRP is known to bind to apoptotic cell membranes (19, 23, 32) and the contents of the core of atherosclerotic plaque include uncleared apoptotic cells as well as mCRP (23, 33). Characteristics of apoptotic cells that could induce binding include membrane shape and lipid composition (blebbing, phosphatidylserine or oxidized lipids being present) (34, 35). Apoptotic cells have been shown to convert pCRP to mCRP (23). However, it is unclear if mCRP takes the form of a monomer, loose pentamer, or oligomer (36, 37). Research in this field has been hampered due to the absence of information regarding what triggers conversion in biological systems. The results from the experiments outlined below contribute to a better knowledge of the pCRP and mCRP conformational states and their interactions with curved membranes.

As mentioned above, CRP has been shown to bind highly curved LDL mimics (38), and LDL may play a role in atherosclerosis and CRP conversion (39). In these studies, pCRP binds preferentially on LDL mimics with a diameter less than 28nm, converts to mCRP, and can bind C1q (40). CRP recognizes membrane curvature, and

membrane shape is able to cause conformational changes in the absence of lipid oxidation or other proteins (38).

Current literature is unclear on the precise interactions of mCRP and pCRP at sites of inflammation with other inflammatory components. The research performed here includes an *in vitro* assessment of specific interactions of conformers with membrane curvature and lipid composition. A strength of the membrane curvature assay is the unique ability to isolate components involved in apoptotic membranes and analyze the binding of CRP in the isolated system. Once individual components are studied, it is useful to return to a cellular membrane approach, which can be accomplished with the expansions to the membrane curvature assay.

CHAPTER TWO: COMPARISON OF BIOCHEMICALLY PREPARED MODIFIED C-REACTIVE PROTEIN

2.1 Introduction

C-reactive protein (CRP) is a mediator of inflammation and plays an active role in the complement immune response to clear foreign material and apoptotic cells from the body (19). The amount of CRP in serum is related to numerous disease states, such as coronary heart disease (41), Alzheimer's disease (42) and autoimmunity (43, 44). In many diseases, elevated CRP levels are related to increased risk (*i.e.* coronary heart disease, Alzheimer's disease) and CRP is often measured as a marker for chronic disease. In other diseases (*i.e.* arthritis, multiple sclerosis) overexpression of CRP in mouse models has been shown to be protective (45, 46). Although elevated CRP levels reveal inflammation, the activity of CRP is necessary for immune system regulation.

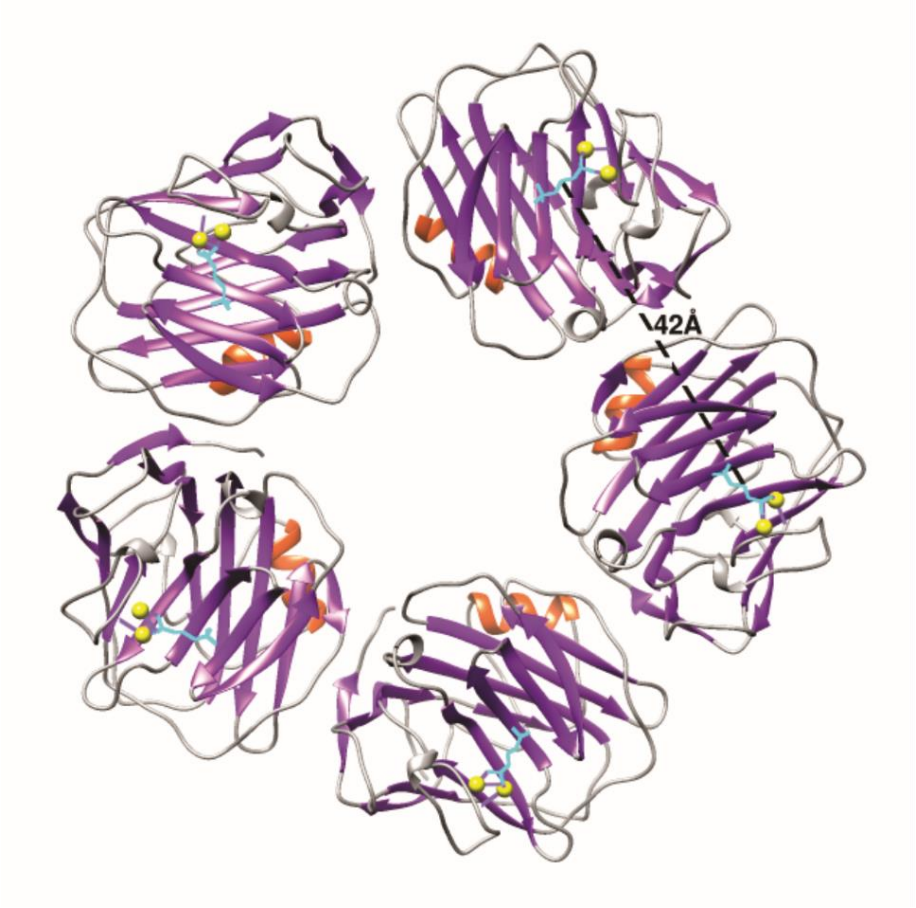

Figure 2. pCRP has rotated protomers and PC binding sites, as seen by the secondary structure. Secondary structure of pCRP includes α-helices (orange) and β-sheets (purple) along with calcium (yellow) dependent PC (blue) to PC binding site (47, 48). *Distance from center of PC binding between protomers is 4.2 nm.*

Native, pentameric CRP (pCRP) is a stable, soluble, homopentamer present in serum. CRP binds to damaged cell membranes and foreign pathogens to activate an immune response for clearance (19, 49, 50). It has been proposed that cellular damage exposes phosphatidylcholine (PC) headgroups and this allows CRP to bind (19) through Ca^{2+} dependent binding sites present on each monomer (48) shown in Figure 2. Upon binding membranes, CRP activation of the complement immune response likely involves pentamer dissociation to reveal neoepitopes (23, 36). The new form of CRP is referred to

as modified CRP (mCRP), but the precise structure of this conformation is not known. In response to the new portions of CRP that are exposed, binding partners, such as C1q, recognize CRP and the complement immune response is initiated (51). The majority of recent research points to membrane bound CRP binding the globular head region of C1q (32, 50, 52, 53). However, mCRP has been shown to bind both the globular head and collagen-like region, with higher binding for the collagen-like region (50). To activate C1q, it is predicted that multivalent binding needs to occur through the globular heads (54). In the pentameric state the pCRP presents only one binding site for the large C1q, so multiple copies are needed (53). One pentamer that dissociates into membrane bound mCRP could lead to multivalent C1q binding. In support of this, other studies have shown that the native form of CRP is incapable of binding C1q and a modified form is required (32, 55).

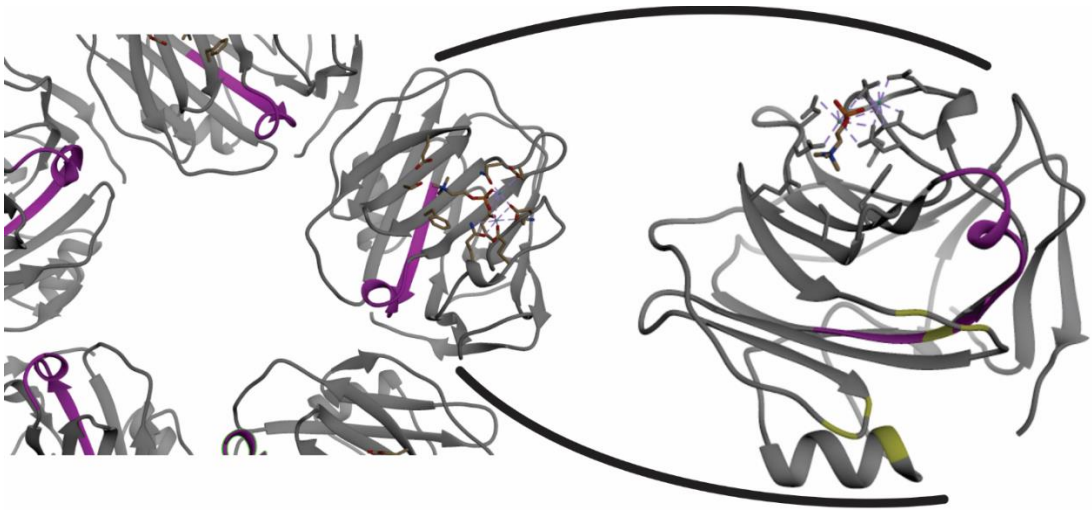

Figure 3. Binding sites of CRP ligands. Two orientations of pCRP and mCRP showing PC bound near the top of the monomer. The cholesterol binding sequence (56) *is highlighted in magenta in both structures and the amino acids residues thought to bind C1q are highlighted in yellow on the monomer* (53). *Imaging utilized UCSF Chimera software with the 1B09 CRP protein data bank file* (47, 48).

The conformation of CRP affects biochemical reactivity and likely has different physiological effects (57). In most patient studies, the soluble, pentameric form of CRP is measured, but there is clear evidence that the conformational state of CRP affects function (32, 37, 58, 59). Multiple forms of CRP have been measured in patient samples, where atypical forms of CRP were identified in patient serum by gel electrophoresis and correlated to obesity (60). Modified forms, as recognized by antibodies that are specific for epitopes that are not exposed in pCRP, have also been found in plaque (23), suggesting an active role of modified CRP in cardiovascular disease.

The causes and effects of CRP conformational changes are not well understood. Proposed causes of conformational change include membrane binding to specific lipids and/or the presence of an acidic environment, like those at sites of inflammation (61, 62). Membrane shape may also play a role in CRP conformational change since certain forms of CRP have curvature preferences (38, 63). In general, binding to membranes likely stabilizes the transition from a pentamer to monomer by allowing for insertion into membranes to stabilize hydrophobic portions of the protein, like the cholesterol binding domain (64), that are newly exposed in the transition from p to m.

The main purpose of this work was to design a method for CRP conversion in the laboratory and an assay for creating a form of CRP that mimics mCRP activity. Since one physiological purpose of CRP is to activate C1q, we have chosen our readout for making an active, modified form of CRP as one that can bind C1q. To determine the best method for CRP conversion, we built upon the work of others where mCRP was made biochemically with 8 M urea and 10 mM EDTA (32, 58, 64–66), with Guanidine HCl

(67) or by dilute SDS and heat (40, 59). We compared a variety of methods for synthesizing mCRP from serum purified pCRP and then tested each method for the ability to produce a form of CRP that: 1) runs differently than pCRP on a non-denaturing polyacrylamide gel and 2) binds C1q, one downstream binding partner of CRP in the complement immune response. The change in conformation was also assessed by tryptophan (Trp) and 1-anilinonaphthalene-8-sulfonic acid (ANS) fluorescence, which show clear differences in conversion methods for mCRP. These methods build upon the work of others that have characterized CRP states by non-denaturing PAGE methods (59) and adds functional relevance through ELISA based assays with C1q. We conclude that dilute SDS/heat treated pCRP consistently produces a functional form of mCRP, whereas only certain concentrations of GndHCl and urea/EDTA have the possibility of being functional mCRP.

2.2 Method

Experimental Contributions

The ANS fluorescence assays were performed by Dr. Aml Alnaas and the circular dichroism of CRP was done by Yuheng Cai. The remaining experiments were done by Carrie Moon.

Materials

C-reactive protein was purchased from Academy Bio-Medical Company (#30P-CRP110) and stored at 4 °C for up to 6 months. Standard CRP concentration used was 57.5 μg/mL unless otherwise noted. C1q was purchased from Complement Technologies (#A099). Standard buffers used for the majority of these experiments were 30 mM

HEPES or PIPES (J.T. Baker), 2 mM calcium chloride, 140 mM sodium chloride, pH 6.4. Chemicals were purchased from Thermo Fisher Scientific or Sigma Aldrich unless otherwise noted. Stock denaturant solutions of 6 M GndHCl and 8 M urea, 10 mM ethylenediaminetetraacetic acid (EDTA) were made in standard buffer (pH 6.4). GndHCl and urea CRP conversion samples were allowed to incubate for 2 hours at room temperature prior to analysis. Dilute sodium dodecyl sulfate (SDS) treated mCRP was made by combining CRP in standard buffer with 0.01% SDS and heating for 1 hour at 80 °C (40). All error values are standard error of the mean.

Structural Analysis

The published crystal structure of CRP with bound PC was used for all structural illustrations and analysis (48). Renderings were done using the UCSF Chimera software (47).

Non-denaturing PAGE

CRP forms were visualized using a non-denaturing polyacrylamide gel electrophoresis (PAGE) assay previously established (40) Standard Laemmli conditions were followed (68) with the exception of using 0.005% SDS in the gel and using native sample buffer (no SDS, β-mercaptoethanol, or heat). These modifications ensured a non-denaturing gel. Standard tris-glycine running buffer containing 0.1% SDS was used. The amount of CRP loaded into each well was 0.43 μg. Gels were run at 80 V for 2 hours and then silver stained. Relative molecular weights for denatured proteins were marked for comparison by using Precision Plus Dual Color Standards (Bio-Rad #1610374). Gels shown are representative of at least 4 experiments.

Tryptophan Fluorescence Spectroscopy

All fluorescence measurements were measured in a Tecan Infinity M1000 Plate Reader using black polystyrol half area 96 well plates (Corning #3694). The intrinsic fluorescence of CRP was measured using 57.5 µg/mL of CRP, which was compared with 3.06 µg/mL tryptophan (the equivalent concentration for the amount of CRP used based on 6 tryptophan residues per monomer). Excitation wavelength was 280 nm with a bandwidth of 2.5 nm. Emission spectra were collected from 300-400 nm with a step size of 5 nm and a bandwidth of 5 nm (Figure 4). The fluorescence intensity from 300-400 nm was integrated and then each value was normalized to the integrated pCRP intensity. Data points were not included when they fell more than two standard deviations from the mean value. The GndHCl denaturation curve was fit to the following equation (69):

$$F = \frac{(F_N + m_N[D]) + (F_U + m_U[D]) * e^{-\left(\frac{\Delta G^\circ_{N/U} + m_G[D]}{RT}\right)}}{1 + e^{-\left(\frac{\Delta G^\circ_{N/U} + m_G[D]}{RT}\right)}}$$

Where F is measured fluorescence, F_N, and F_U are the fluorescence of the native state, and the unfolded state, respectively. The slopes are for the native (m_N) and unfolded (m_U) states of the protein. [D] is the concentration of denaturant. $\Delta G^\circ_{N/U}$ is the Gibbs free energy of unfolding. R is the universal gas constant (8.314 J mol^{-1} K^{-1}) and the temperature (T) used for calculations was 298 K.

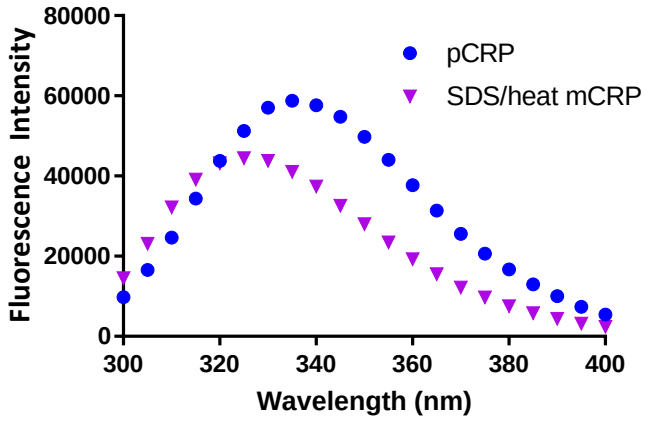

Figure 4. Sample fluorescence spectra from pCRP and mCRP made with SDS and heat. Data from each spectrum was integrated from 300 to 400 nm to give a single value for each well, those values were normalized to the pCRP value for that day. Combined data is plotted with averages and SEM in Figure 5 and Figure 7.

Dynamic Light Scattering

Dynamic light scattering (DLS) was performed on a DynaPro Plate Reader II with Dynamics version 7 software (Wyatt Technology) using a 384 well glass bottom plate (Greiner Bio-One Sensoplate #781892). CRP (500 µg/mL in pH 6.4 PIPES buffer, details above) was placed into 4 wells for measurements (50 µL). The plate was centrifuged at 200 rpm for 2 min. Readings were performed at 25 °C using a 5 s acquisition time with auto-attenuation. The solvent setting for the system used was based on phosphate buffered saline with a refractive index of 1.333 (at 589 nm for 20 °C) and a viscosity of 1.019 cP. Each well had 10 acquisitions. A Rayleigh spheres model was used to fit the data with the Dynamics software.

Circular Dichroism

CRP samples of pCRP and $mCRP_{Heat}$ were prepared for circular dichroism (CD) by dilution in standard HEPES buffer at pH 7.4 to a concentration of 19.6 µg/mL. Dilute

SDS samples contained 19.6 µg/mL of CRP in phosphate buffer (10 mM disodium phosphate, 2.7 mM potassium chloride, 1.8 mM monopotassium phosphate, 1 mM calcium chloride, pH 7.6) with 0.005% SDS. CD spectra from 207-250 nm was recorded using a JASCO J-1500 Circular Dichroism Spectrometer. Samples with SDS were heated and measured at 5-degree intervals from 20 to 80 °C and then allowed to cool to room temperature (20 °C) before the final scan. Background CD spectra from buffers was subtracted for all samples.

ANS Fluorescence Assay

1-Anilinonaphthalene-8-sulfonic acid (ANS), a hydrophobic fluorescent probe purchased from Cayman Chemical (Ann Arbor, MI), was used to monitor the conformational changes of CRP after treating the protein with different denaturants. The stock solution of 100 mM ANS was dissolved in DMSO and diluted to a final concentration of 190 µM with Millipore water. CRP (50 µg/mL) was incubated with the GndHCl or urea/EDTA denaturants in HEPES buffer (pH 6.4) for 2 hours at 37 °C. Dilute SDS CRP samples were heated for 1 hour at 80 °C with 0.01% SDS in HEPES buffer (pH 6.4). The control pCRP sample was diluted in TBS buffer (50 mM Tris-HCl, 150 mM NaCl, 0.1 mM CaCl2, pH 7.2). Fluorescence intensity of ANS was measured using an excitation wavelength of 390 nm, and emission spectra were measured from 440 nm to 650 nm. The same plate reader and plates listed above in tryptophan fluorescence were used for ANS experiments.

Enzyme Linked Immunosorbent Assay (ELISA)

The binding of CRP to C1q was measured by performing an ELISA with C1q as a capture at a concentration of 1 µg/mL, following previously published procedures (40). Bovine serum albumin (BSA, 1 µg/mL) was used as a control in place of the C1q capture. BSA or C1q were diluted in coating buffer (30 mM sodium carbonate, 70 mM sodium bicarbonate, pH 9.6, Sigma Aldrich). 100 µL of coating solution was added to the microwells in a Microlon 600 96W high binding clear microplate (either Greiner Bioscience 655081 or Nunc Maxisorp Immuno Plate 446612). Control wells were tested with plain coating buffer (no protein) which resulted in similar results as with BSA due to the BSA block. Fish gelatin at 3% was tested as an alternative blocking agent, however since this failed to block non-specific binding, BSA or fatty acid free BSA was used as a blocking agent. After a 2 hour incubation at 37 °C or an overnight incubation at 4 °C, wells were washed three times with 300 µL of phosphate buffered saline with 0.05% Tween-20 (PBST; Acros Organics) and once with 300 µL of phosphate buffered saline (PBS). Next, 300 µL of blocking buffer (3% w/v BSA in PBST) was added and the plate was incubated at room temperature for 2 hours. In between each step in the assay, wells were washed as described above (three times with PBST and once with PBS). 100 µL of CRP (1.8 µg/mL) in diluting buffer (1% w/v BSA in PBS) was added and incubated for 1 hour at 37 °C. The antibody, a biotinylated polyclonal anti-CRP (Academy Biomedical Co. #CRP30BG1), was diluted at a ratio of 1:5,000 in diluting buffer and 100 µL was added and incubated for 1 hour at 37 °C. After washing, 100 µL of a 1:10,000 dilution of HRP-Strep was added to each well and incubated for 30 minutes at 37 °C. A final wash

sequence was followed by the addition of 100 µL of 3,3',5,5'-tetramethylbenzidine (TMB) substrate. After the color was allowed to develop (5-10 min) at room temperature, the reaction was stopped by the addition of 100 µL of 0.5 M sulfuric acid, turning the reaction solution from blue to yellow. Absorbance was measured at 450 nm, with a reference absorbance of 620 nm on a Microplate reader (Tecan infinite-M1000 PRO). Data was normalized by day to either 0 M denaturant (pCRP) or mCRP with SDS and heat absorbance values.

2.3 Results

To determine the stability of the native, pentameric form of CRP, we denatured CRP using two common denaturants, urea/EDTA and GndHCl. The intrinsic tryptophan fluorescence was measured and found to decrease with increasing denaturant, as expected, for most concentrations (Figure 5A and Figure 5B). The change in fluorescence occurs as some of the 6 Trp residues (per monomer of CRP) go from a hydrophobic protein environment to a more aqueous environment. Denaturation with GndHCl led to a clear transition (Figure 5A) between 2 and 2.75 M GndHCl, however, the gradual decline in fluorescence from 0 to 2 M suggests conformational changes are occurring even at low concentration. Interestingly, tryptophan fluorescence increases at GndHCl concentrations higher than 4.25 M (see Figure 6A), so only data ≤ 4.25 M GndHCl was used for fitting. A slight change in the appearance of the band with non-denaturing gel is observed at higher concentrations of GndHCl (Figure 6B). The change in fluorescence was fit, as described in the methods, to give a Gibbs free energy of unfolding ($\Delta G°_{N/U}$) of 32 ±12 kJ/mol and a m value of -13 ±5 kJ/mol. With a weaker denaturant, urea/EDTA, the

decrease in fluorescence is more gradual and lacks a clear transition. If pCRP was completely denatured, the expected Trp fluorescence would be equal to the same amount of free Trp in buffer. The integrated fluorescence intensity for free tryptophan based on the concentration of CRP present was measured in the denaturants for comparison with CRP samples, as shown in Figure 5A, Figure 5B, and Figure 7C. It is interesting to note that the tryptophan fluorescence of CRP treated with 4 M GndHCl falls below that of free tryptophan, while 7 M urea treated CRP and free Trp have similar integrated fluorescence intensities.

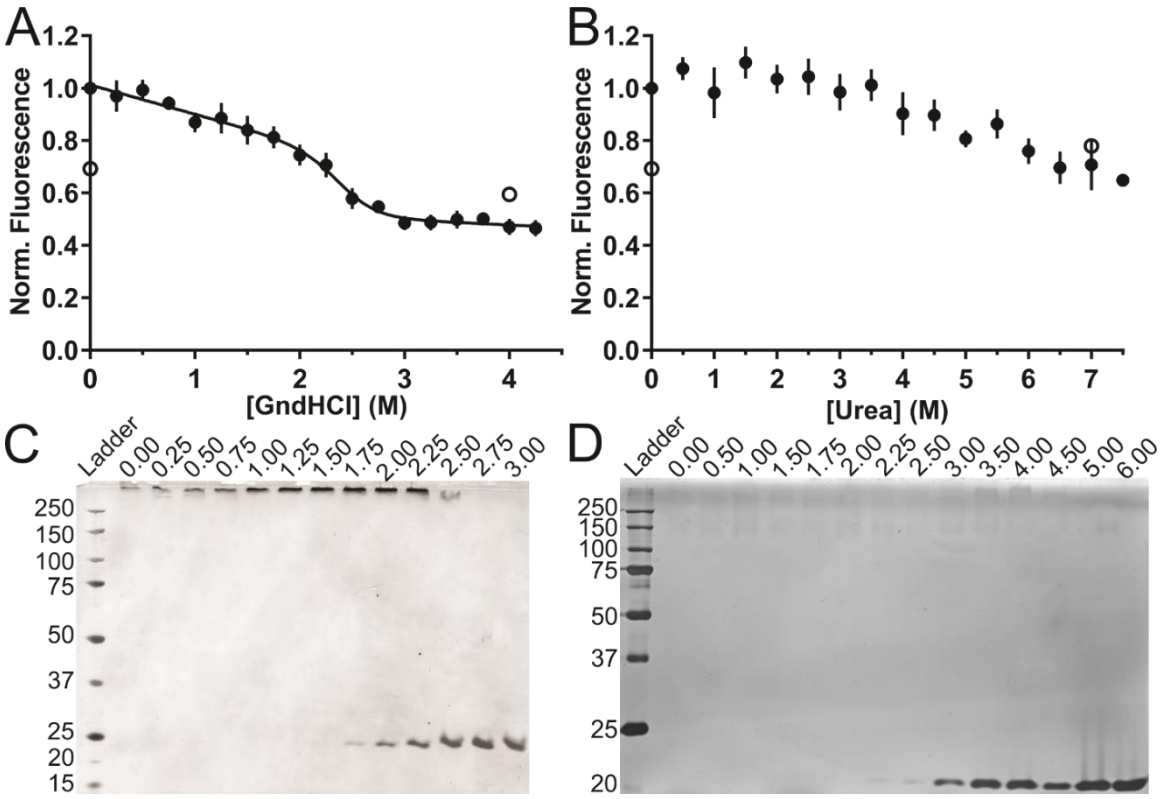

Figure 5. Intrinsic fluorescence and non-denaturing PAGE assays of CRP treated with GndHCl and urea. Intrinsic, tryptophan fluorescence was measured by exciting solutions at 280 nm and recording fluorescence from 300-400 nm for both GndHCl (N=8, A) and urea/EDTA (N=10, B) treated CRP (black filled circles) as well as select concentrations for free tryptophan (open circles). The integrated fluorescence was normalized to the 0 M denaturant data point. The solid line in A is a fit used to determine the energy of unfolding as described in the Experimental Procedures. Error bars are ± SEM. Non-denaturing PAGE of CRP treated with GndHCl (C) and urea/EDTA (D) after two hours of incubation. The ladders shown are SDS-PAGE (denatured) protein standards for relative molecular weight comparison. Gels shown are representative of at least 4 experiments.

After measuring the intrinsic fluorescence to identify changes in the exposure of Trp residues to an aqueous environment, samples were loaded onto a non-denaturing polyacrylamide gel to assess the presence of different states of CRP. Non-denaturing gel conditions were used because mCRP fails to appear under native gel conditions that contained no SDS, which has been confirmed by others (59). Both the molecular mass and the charge affect migration in this assay. In Figure 5C and D, a clear transition occurs

where a modified form of CRP begins to show, running similar to the 20 kDa standard. Although the gels shown in Figure 5 appear to have slightly different running distances for the mCRP band, comparisons of all gels run do not show a consistent difference. With GndHCl treatment, this band first shows up at 1.75 M GndHCl and is fully present at 2.75 M, matching the profile of intrinsic fluorescence in Figure 5A. When pCRP is treated with urea/EDTA, a clear transition exists in the gel from 2.25 to 4.00 M urea. The mCRP band increases over this range and the pCRP (not shown but retained in the stacking portion of the gel) disappears. pCRP is a 115 kDa pentamer with a pI of 6.4 that changes to 5.6 upon monomerization with urea (67). The pentameric form has less charge density, is larger, and therefore does not run well into the gel. A haze of protein is also observed in the gel and this fully disappears at 4.00 M. This could be due to alternative states of pCRP that have not been fully characterized and these are present in the absence of urea (Figure 5D, 0.00 M).

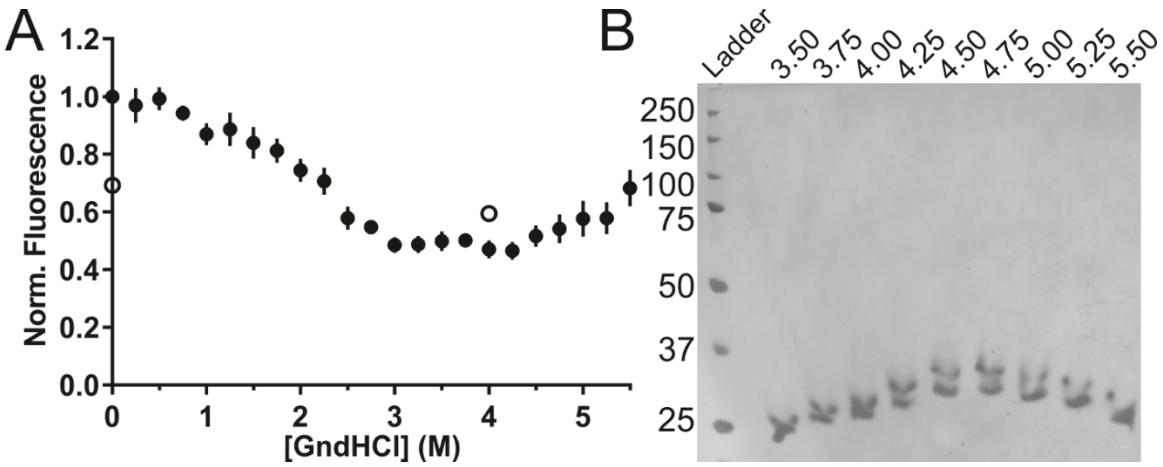

Figure 6. Higher concentrations of GndHCl lead to changes in intrinsic tryptophan fluorescence and non-denaturing gel bands. A) The integrated, normalized tryptophan fluorescence of GndHCl treated CRP (black filled circles), N=8. Free tryptophan was measured for pCRP (0 M GndHCl) and 4 M GndHCl treated CRP (open circles), N=9. All error is SEM. B) Non-denaturing PAGE of higher GndHCl concentrations with shift in bands of mCRP at higher concentrations. Gel is representative of 4 gels.

To determine if other denaturants can be used to make a functional form of mCRP, dilute amounts of detergent (SDS) were tested along with heat. Non-denaturing PAGE reveals a band around 20 kDa for mCRP made from exposure to 0.01% SDS with heat and a high band for pCRP (Figure 7A). Since pCRP remains in and near the stacking portion of the non-denaturing PAGE gel, dynamic light scattering (DLS) was used to confirm that pCRP is not aggregating. 99.85% ± 0.09 of the results for the hydrodynamic radius fell between 0 and 10 nm, with an average radius from that range is 4.12 ± 0.15 nm (Figure 7B). DLS with SDS and heat treated mCRP gave results that indicated aggregation due to the high concentration (500 μg/mL) needed to run the experiment. The different properties of dilute SDS and heat treated CRP are evident when free tryptophan and CRP levels of all the denaturants are compared. Only mCRP made with SDS and heat has a normalized integrated fluorescence between the pCRP and free tryptophan levels (Figure 7C).

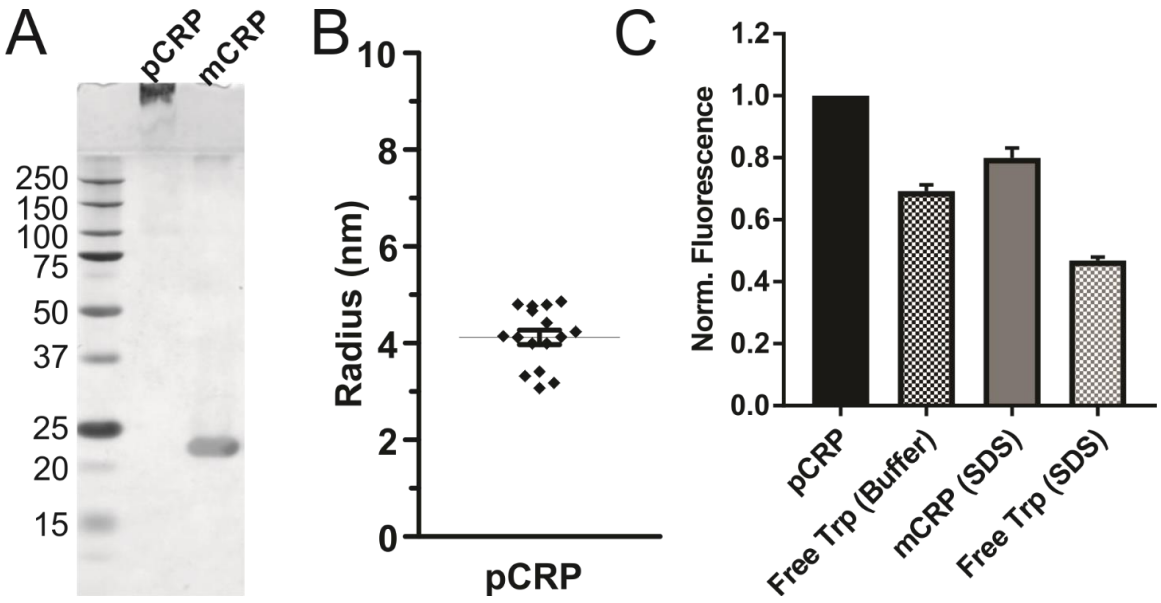

Figure 7. Dilute SDS with heat treatment leads to monomeric CRP. A) Non-denaturing PAGE of pCRP and CRP heated with 0.01% SDS (mCRP) demonstrates that the two forms have different electrostatic properties. B) Data on the graph is from the 0-10 nm radius range and represents 99.85% ± 0.09 mass detected by dynamic light scattering. Average radius measured is 4.12 ± 0.15 nm. C) Comparison of intrinsic tryptophan fluorescence for pCRP and SDS with heat mCRP with fluorescence of free tryptophan. Normalized to pCRP, N=9. All error is SEM.

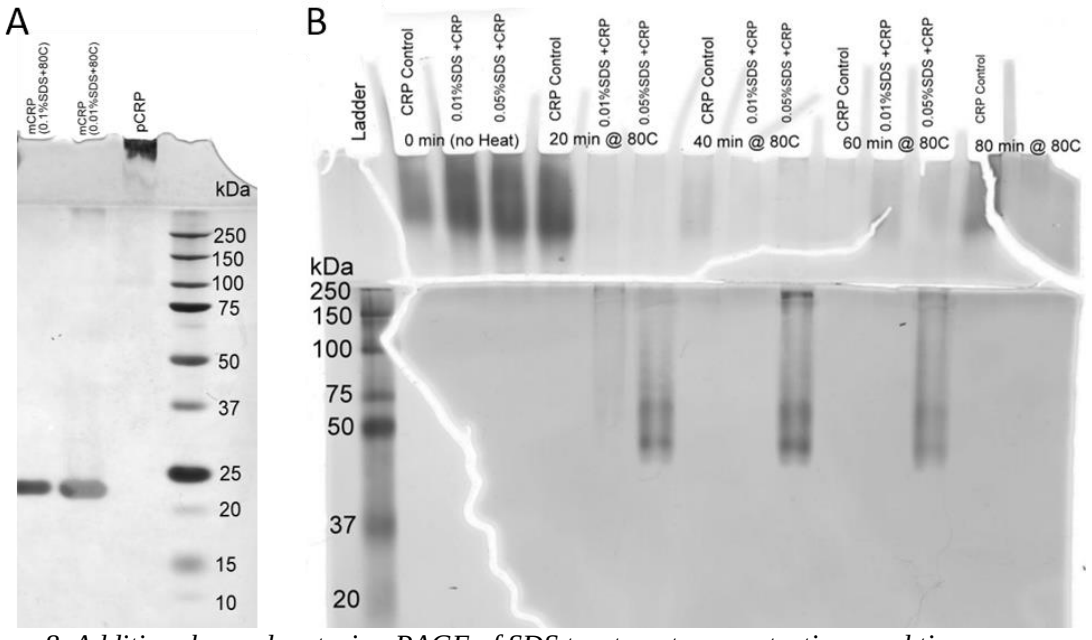

Figure 8. Additional non-denaturing PAGE of SDS treatment concentrations and times.

Circular dichroism (CD) was used to measure CRP during the denaturation process to assess whether conformational changes were occurring to the secondary structure. pCRP and mCRP have a different CD signal from 210 to 230 nm with a dip for pCRP (Figure 9A). Although there is a different CD signal for pCRP and mCRP forms, the two methods tested for mCRP – with dilute SDS and heat or with just heat – have similar spectra. CRP treated with dilute SDS was tested at various temperatures and Figure 9B shows full conversion from pCRP to mCRP around 70 °C with a less structured spectra. CRP that has been cooled back to room temperature post heating to 80 °C continues to show less structure in the 210-230 nm region of α-helices and β-sheets.

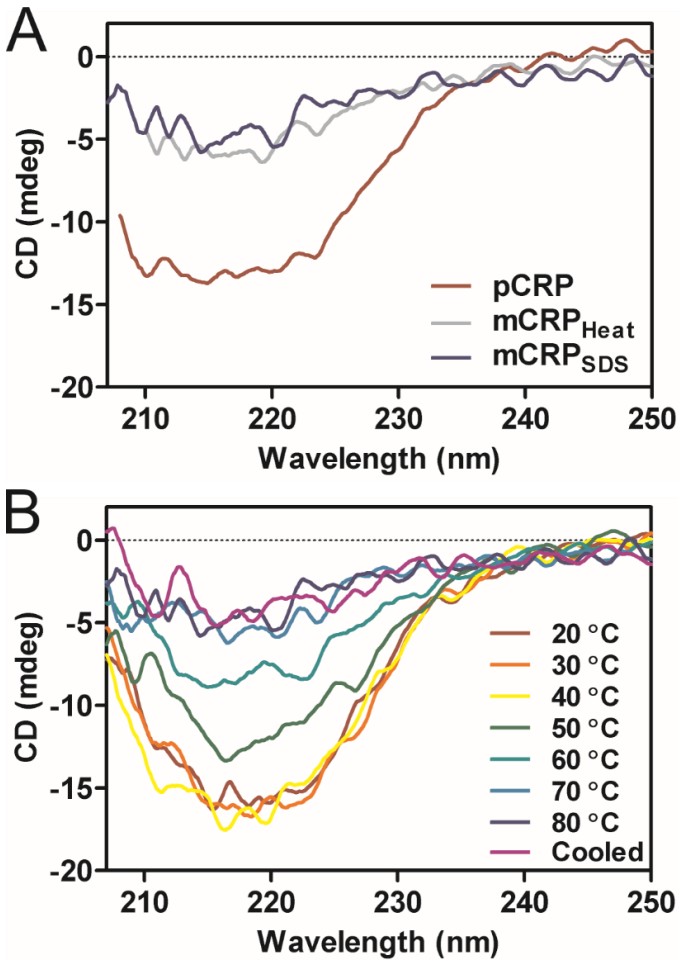

Figure 9. Circular Dichroism of CRP forms shows a structural change. A) Circular dichroism spectra of pCRP (red line) and mCRP made from heat only (grey line) and dilute SDS with heat (red line). B) CRP sample with dilute SDS in buffer heated in the cuvette from 20-80 °C with CD spectra recorded and final sample allowed to cool back to room temperature.

To monitor CRP unfolding after incubation with different denaturants ANS, a hydrophobic fluorescent probe, was utilized. ANS is frequently used in biochemistry and biophysics research to identify protein folding and aggregation. ANS binds to hydrophobic regions of proteins, which leads to a significant increase in its quantum yield and a blue shift in the emission maxima (70). Previous research has used ANS to investigate the conformational changes of CRP at various pH and temperatures (62, 71). Because ANS binds hydrophobic regions, an increase in ANS fluorescence indicates that

the protein has more hydrophobic regions exposed. As shown in Figure 10, treatment with 3 M GndHCl (Figure 10A), 6 M urea (Figure 10B), or 0.01% SDS with heat (Figure 10C) caused hydrophobic portions of CRP to be exposed. SDS-treated CRP showed the largest change (Figure 10C, black circles) from the untreated CRP (grey triangles in all figures) compared to other denaturants.

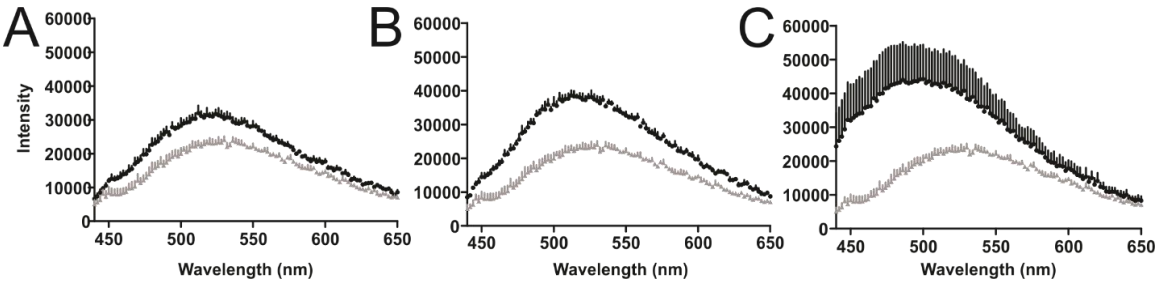

Figure 10. Treatment of CRP with denaturants increases ANS binding. ANS fluorescence upon binding to CRP incubated with (A) 3 M GndHCl for 2 hours at 37 °C (black circles), (B) 6 M urea/EDTA at 37 °C for 2 hours (black circles), and (C) 0.01% SDS with incubation at 80 °C for one hour (black circles). Grey triangles for all are pCRP. N=3

After altering the conformation of pCRP with urea/EDTA, GndHCl and 0.01% SDS with heat, we assessed whether the new forms of CRP could bind C1q, a well-established binding partner for initiation of the complement immune response. Enzyme-linked immunosorbent assays (ELISAs) were performed where C1q was used to capture CRP. A polyclonal antibody to CRP with a biotin linkage was used to then bind horseradish peroxidase linked streptavidin (HRP-Strep). In Figure 11, the GndHCl treated CRP clearly shows binding to C1q (black filled circles), however, for most concentrations, similar binding was observed for a control, where bovine serum albumin (BSA) was used as the capture protein. Statistical significance between BSA and C1q binding only exists at 1.5 M GndHCl (p-value of 0.0037 for Student's paired t-test). Urea treated CRP binds BSA comparably to C1q and the binding is not statistically significant

(Figure 6B). Acid treated CRP shows similar behavior which indicates that the binding observed is not specific (62). However, dilute SDS with heat-treated CRP does have significant C1q binding with a p-value of 0.0103 as determined by a two-tailed paired Student's t-test (Figure 11). Table 1 contains a detailed list of all p-values. As pCRP converts to mCRP, more amino acid residues are exposed, as well as areas of binding sites for ligands (Figure 13 and Figure 3). A summary of the results for each CRP form is shown in Table 2.

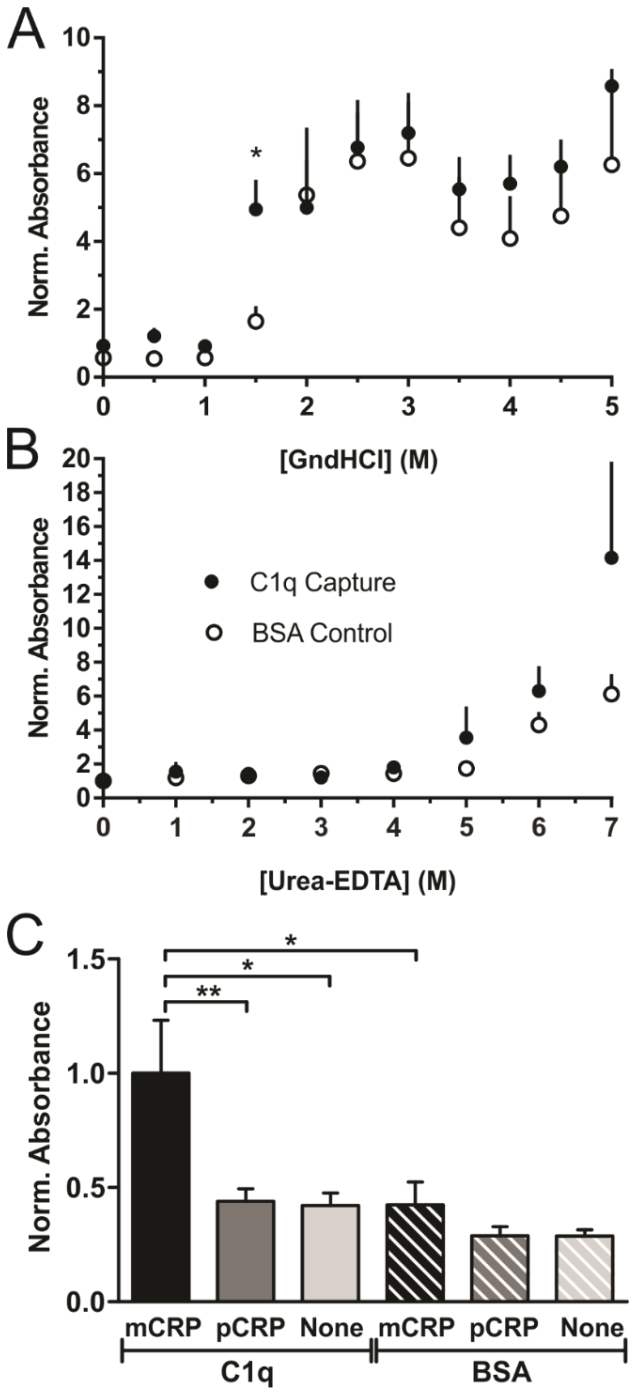

Figure 11. Denaturation of pCRP by GndHCl, urea/EDTA, or dilute SDS with heat alters CRP binding to BSA and C1q. ELISA with BSA (open circles or solid bars) or C1q (filled circles or striped bars) as the capture agent was performed to determine if denaturation at a certain concentration leads to a form of CRP that can bind C1q. A) CRP treated with 1.5 M GndHCl (or higher concentrations) leads to C1q binding, however the binding above 2 M GndHCl is not specific; BSA capture works equally well. B) Urea treated CRP binds C1q at 5 M and higher concentrations, but also binds BSA non-specifically. Data for A and B was normalized to pCRP

*(0 M GndHCl or urea). C) C1q captures CRP treated with 0.01% SDS and heated at 80 °C for 1 hour (solid black), but not pCRP (solid grey) or antibodies (solid light grey). BSA captures mCRP significantly less than C1q (black stripes), but captures more 0.01% SDS with heat treated CRP than pCRP (grey stripes) or antibodies (light grey stripes). Data was normalized to the average mCRP absorbance with C1q capture. Significance was calculated using a two-tailed Student's paired t-test (p-values < 0.05 shown as * and < 0.01 shown as **). Detailed significance for C can be found in supplemental Table 1. Error bars are SEM and only shown in the positive direction for clarity. Often the SEM is smaller than the data point.*

Table 1. ELISA t-test results.

t-test partner	Capture	Antigen	Values (paired, two-tailed)	Significance
C1q-mCRP$_{SDS}$	BSA	mCRP	0.0103	*
	BSA	pCRP	0.0067	**
	BSA	None	0.0102	*
	C1q	pCRP	0.0091	**
	C1q	None	0.0106	*
C1q-pCRP	BSA	mCRP	0.5775	NS
	BSA	pCRP	0.0014	**
	BSA	None	0.0035	**
	C1q	None	0.6587	NS
BSA-mCRP$_{SDS}$	BSA	pCRP	0.0432	*
	BSA	None	0.0629	NS
BSA-pCRP	BSA	None	0.2092	NS
C1q-None	C1q	BSA	0.0106	*
C1q-CRP$_{1.5M\ GndHCl}$	BSA	CRP$_{1.5M\ GndHCl}$	0.0037	*
C1q-CRP$_{7M\ Urea}$	BSA	CRP$_{7M\ Urea}$	0.2972	NS

2.4 Discussion

CRP is known to have both a pentameric native form and a modified form that exposes neoepitopes (55, 67). We confirmed with DLS that purchased pCRP, prior to denaturation methods, had a hydrodynamic radius (R_H) within range for the pentameric state (4.12 ± 0.15 nm, Figure 7B). In comparison, the measured radius from the pCRP crystal structure is 5.1 nm (22) and the radius of gyration (R_g) for pCRP is 3.7 nm, as determined by x-ray scattering (66). The R_g has a linear relationship to the R_H for

spheroidal objects that can be summarized by the equation $R_g = 0.775 \times R_H$ (72). Using the R_H found by DLS above, our calculated radius of gyration would be 3.19 ± 0.12 nm. Since CRP is a disk-shaped pentagon (73) and not a perfect sphere, a slight discrepancy between the calculated and observed R_g values is expected. With salt concentrations in buffer, CRP is expected to stay as a pentamer and not form a decamer (66). Having established that CRP without any denaturant is the native, pentameric form, the next step was to produce an *in vitro* mCRP.

Denaturants, such as chemicals or heat, have a wide range of effects on proteins and *in vitro* studies of denaturing individual proteins provide a better understanding of protein function and structure (74–77). Chemicals used to denature include strong acids and bases, salts, detergents, or organic solvents; examples include sodium dodecyl sulfate, guanidine hydrochloride, urea, hexane, and trifluoroacetic acid (74, 78). These chemical denaturants disrupt the interactions that stabilize the secondary, tertiary, and/or quaternary structures of the protein (i.e. van der Waal's interactions, salt bridges, and hydrogen bonds) and alter the native state. As larger concentrations of denaturants are added, the protein can have meta-stable forms, as previously established in work with oligomeric proteins (79). One way of measuring denaturation and stable states is to use tryptophan fluorescence. Depending on the location of the tryptophan residues, unfolding will cause either quenching or increased fluorescence intensity and a melting curve for a protein can be used to calculate data about stability. Results here from many biochemical assays indicate that methods used to make mCRP have varied effects on the structure of pCRP.

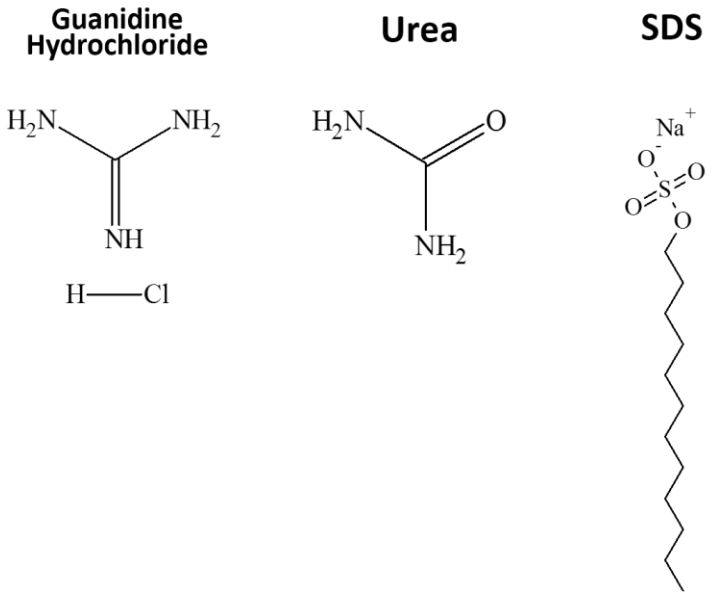

Figure 12. Chemical denaturants guanidine hydrochloride, urea, and SDS were incubated with CRP at various concentrations to test for pCRP to mCRP conversion.

These incongruent effects can be attributed to differences among the denaturants used: GndHCl, urea, and SDS (Figure 11). SDS is a detergent that others have shown to denature without aggregation at high concentrations (74). However, at the low concentrations used in this work, it is anticipated that SDS works to stabilize the meta-stable state of mCRP. Urea and GndHCl are chaotropic denaturants shown to have destabilizing effects on proteins (80, 81). Despite only having a slight structural difference, as seen in Figure 11, GndHCl and urea impact proteins differently. GndHCl is considered to be a strong chemical denaturant and was shown by others at limited small concentrations of GndHCl to stabilize aggregation with some proteins in the molten globule state, whereas urea did not (82). The strong denaturing properties and the distinct way that GndHCl interacts with CRP in comparison to urea can be seen in the results of these biochemical studies.

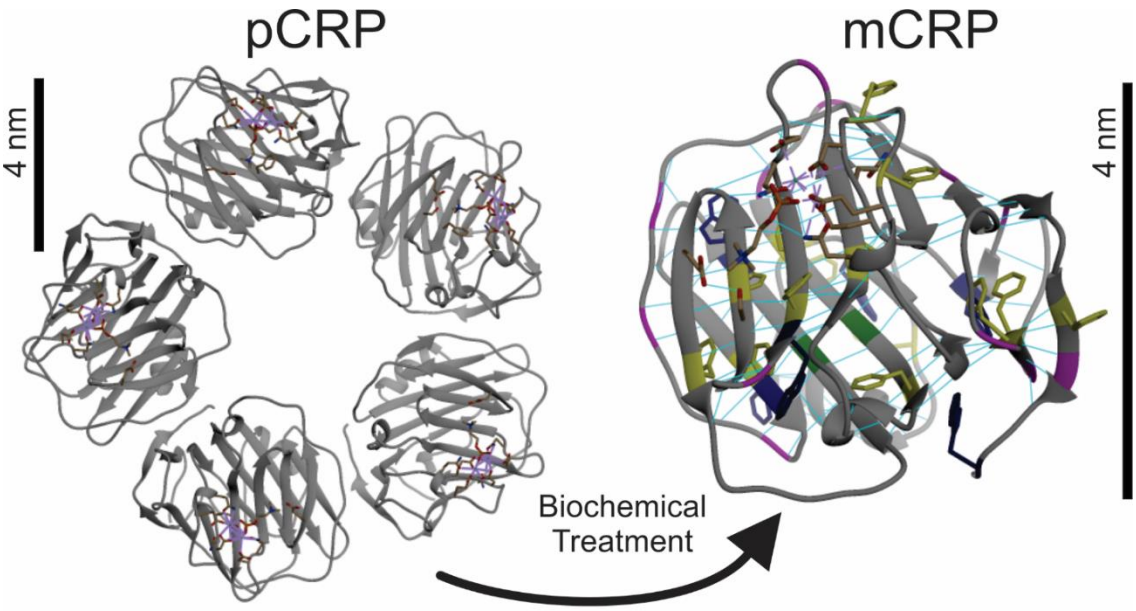

Figure 13. pCRP to mCRP conversion with highlighted amino acid residues. CRP monomer contains 6 tryptophan residues (navy blue), 13 lysine residues (magenta), 14 phenylalanine residues (yellow), and 2 cysteine residues to form the disulfide bond (green) (83). *Hydrogen bonding between molecules is shown in cyan* (47, 48).

One assay often used to explore the two states of CRP is gel electrophoresis. Whether a 2D urea gel (84), reduced SDS (59), or the conditions used here for non-denaturing PAGE, all results show a pCRP band that runs high and a mCRP band that runs low. Each gel (Figure 5C, Figure 5D, and Figure 7A) shows a native pentameric form that stays near the stacking portion (bands in Figure 5D have been cropped). Non-denaturing gels separate proteins based on more than molecular weight, including protein shape and charge. The pCRP structure has salt bridges between subunits, hydrogen bonding, and van der Waals forces (85). Besides these interactions for pCRP, differences in how pCRP and mCRP run on a gel can be attributed to a change in the pI from 6.4 to 5.4 (67). The gel conditions include pH values of 8.3 for the running buffer, 6.8 for the stacking portion, and 8.8 for the running portion of the gel, supporting mCRP having

more charge and running farther on the non-denaturing gel. Treatment of CRP with ≥ 2.5 M GndHCl, ≥ 3 M urea/EDTA, or 0.01% SDS with heat all run close to the molecular weight for a CRP monomer (23 kDa) with non-denaturing PAGE. This demonstrates a clear transition and separation of pCRP and mCRP bands.

The difference in the secondary structure of pCRP and mCRP forms (Figure 9A) indicates that mCRP is not merely a monomeric form of pCRP, but that it undergoes a structural change. Types of secondary structure that show up in the 210-230 nm region include α-helix and anti-parallel β-sheet (86). Native CRP has two antiparallel β-sheets and one α-helix per protomer (Figure 13) (22, 48). CD spectra of recombinant mCRP in comparison to pCRP have been reported to have a significant secondary structural change, mainly from β-sheet to α-helix, although no spectra was published (65). This structural change may be what gives mCRP its different binding properties, such as C1q binding. Comparing mCRP treated with dilute SDS and heat while at 80 °C and then after being cooled shows similar spectra (Figure 9B) concluding that when mCRP is made with dilute SDS and heat that it does not revert to pCRP upon cooling.

Since no intermediates were observed in the gel (only modified and native), we used a two-state model to fit the GndHCl Trp fluorescence data (Figure 5A, black line). The intermediate states of fluorescence intensity can be assumed to be a mixture of folded and unfolded states, not proteins that exist in an intermediate state. However, the work of others (49) suggests that tetramers, trimers and dimers may exist under certain conditions. Our work suggests that only two states exist in a purified biochemical system.

Other conditions and the presence of other proteins may stabilize intermediate states that are not observed here.

The results of the fit are what would be expected for a multimeric protein that has a slow transition. The change in free energy represents the conformational stability of a protein and most proteins have a value of 20-60 kJ/mol for stability of the native state above the unfolded state (87). CRP has a $\Delta G°_{N/U}$ of 32 ± 12 kJ/mol. In comparison, a $\Delta G°_{N/U}$ for α-lactalbumin, a smaller monomeric protein, was found by others to be 10.12 ± 0.33 kJ/mol (88) and the $\Delta G°_{N/U}$ for phenylmethanesulfonyl α-chymotrypsin, a larger monomeric protein, was calculated from experiments with GndHCl to be 36.4 ± 1.8 kJ/mol (originally in kcal/mol) (69). The $\Delta G°_{N/U}$ of pCRP to mCRP based on the transition with GndHCl treatment indicates that pCRP requires a substantial energetic input to change forms. This is consistent with the work of others in requiring large amounts of heat or high concentrations of urea to biochemically make mCRP (55, 59).

GndHCl appears to transition at a similar point with both Trp fluorescence and non-denaturing PAGE (Figure 5A, around 2.5-3 M). The observed Trp fluorescence transition for urea treated CRP is gradual (from 2 – 6 M) and over a much wider range than that observed in the gel (Figure 5B). This gradual transition suggests that conformational changes are still occurring that affect the Trp environment, but that these changes do not broadly influence the size or charge of the protein in a way that affects how it runs on a gel. The transition likely occurs over a larger range of urea concentrations because urea is a weaker denaturant than GndHCl. Each CRP monomer contains 6 Trp residues, which allows for comparison to a control sample of free Trp

(Figure 5A and Figure 5B, open circles). The lower fluorescence for CRP treated with 4 M GndHCl than for free Trp at the same concentration suggests quenching. Tryptophan is sensitive to environment and many different interactions may contribute to a decrease in fluorescence including aggregation or quenching from nearby residues such as phenylalanine and lysine (89). There are two Trp residues with an adjacent phenylalanine and the CRP sequence contains 13 lysine residues per monomer (Figure 13). Conformational changes near the tryptophan residues are most likely the cause of the quenching and the lower than expected fluorescence. However, aggregation of CRP may also explain the low Trp fluorescence followed by an increase at higher concentrations of GndHCl due to stabilization and protein denaturation (Figure 6A). Each denaturant has a slightly different change in ANS fluorescence in comparison to free ANS in solution (Figure 10), which points to a difference in how the denaturants change the structural form of CRP. Urea and dilute SDS with heat treated CRP show a larger increase in ANS fluorescence, with the dilute SDS form being the largest change, indicating hydrophobic regions being exposed. A change in the amino acid residues exposed for mCRP is consistent with the observance of a mCRP specific aptamer (40, 90).

The biochemical assays for both tryptophan and ANS fluorescence indicate that each denaturant affects pCRP differently. In order to determine which denaturant makes a biologically relevant mCRP form for *in vitro* experiments binding to the downstream C1q complement protein was analyzed with an ELISA (Figure 6). Paired, two-tailed Student's t-tests revealed that the only forms with statistically significant binding to C1q were mCRP treated with 1.5 M GndHCl and with dilute SDS and heat. Although, many

conditions can cause monomerization and denaturation, only certain conditions leave CRP in a state that is capable of binding C1q. Denaturation with GndHCl is likely harsh and causes full unfolding, such that the sites needed for C1q binding are no longer intact. Instead, the protein binds a wide variety of other proteins, like BSA, likely in a non-specific way, similar to what others have seen with acid treated CRP (62). In previous research, others have shown that while CRP treatment with 5 M GndHCl appears to have some monomeric properties (91), various concentrations of GndHCl failed to produce a mCRP form with neoantigenicity (67, 91). This discrepancy was contributed to different pH levels for the experiments, and in light of the research here, GndHCl appears to have a wide variety of effects on CRP. Urea/EDTA denaturation has a similar behavior with a trend towards binding C1q more than BSA at high concentrations of urea. Results from a fluorescent anisotropy assay confirm acid treatment also did not allow CRP to retain C1q binding abilities (40). This agrees with recombinant mCRP and not pCRP to C1q with surface plasmon resonance (55). Meanwhile, gentle unfolding with dilute SDS (0.01%) and heat retains binding to C1q (Table 2).

In the literature, mCRP has been made with a wide variety of methods. Treatment with 8 M urea-EDTA is frequently used for pCRP to mCRP conversion (32, 38, 58, 66, 84) and our results indicate that concentrations of urea >7 M are likely to follow the upward trend to make a CRP form with significant C1q binding. One method commonly used for cellular and animal experiments is recombinant mCRP (65, 71). The recombinant form has been shown by others to bind C1q and is considered similar to urea chelated mCRP in other assays (55, 65, 92, 93). The recombinant form remains mCRP

and does not revert back to pCRP (65). This is good for purification, however the method for expression and purification is time consuming (94). The method of making mCRP with 0.01% SDS and heating for 1 hour at 80 °C is consistent with functional relevance of C1q binding, in both this work and the work of others (40). The ability to maintain functional relevance when the mCRP treated with heat and SDS has been diluted points to a permanent change in the molecular structure, which, similar to recombinant mCRP, indicates that mCRP is unlikely to return to pCRP. Further studies of mCRP would benefit from using the SDS and heat preparation method due to the consistent C1q binding and simple technique.

Table 2. Summary of biochemical preparations of mCRP and their results.

CRP Preparation	Transition to mCRP	Structural Notes	C1q binding
GndHCl	Non-denaturing PAGE & Trp Fluorescence show transition around 2.75 M	Hydrophobic portions exposed (Trp and ANS Fluorescence)	Only at 1.5 M GndHCl
Urea/EDTA	3 M is where an mCRP band starts to show up in non-denaturing PAGE	Hydrophobic portions exposed (Trp and ANS Fluorescence)	Trends toward binding at 7M, but not statistically significant
SDS/Heat	0.01% SDS and heat for 1 hour at 80 °C has mCRP band	Aggregates at higher CRP concentrations (DLS); CD spectra loses dip in secondary structure region	0.01% SDS with heat has statistically significant C1q binding

2.5 Summary

C-reactive protein (CRP) is commonly measured as an inflammatory marker in patient studies for coronary heart disease, autoimmune disease, and recent acute infections. Because of the correlation of CRP to a vast number of disease states, CRP is a well-studied protein in medical literature with over 11000 references in PubMed (95). However, the biochemical and structural variations of CRP are not well understood. Conformations of CRP are thought to affect disease states differently, with a modified form showing neoepitopes and activating the complement immune response through C1q binding. Despite the broad interest in CRP, there is a noticeable gap of information in the biochemical literature regarding how different conformational states affect biochemical reactivity. In this work, we compare the unfolding of CRP using chemical denaturants

and identify which states of CRP bind a downstream complement immune response binding partner (C1q). We used guanidine HCl (GndHCl), urea/EDTA, and 0.01% SDS with heat to perturb the pentameric state. All treatments give rise to a monomeric state in non-denaturing polyacrylamide gel electrophoresis experiments, but only treatment with certain concentrations of denaturant or dilute SDS with heat maintains CRP function with downstream binding partners when measured using enzyme-linked immunosorbent assays. The results suggest that the final form of modified CRP and its ability to mimic biological reactivity depends on the preparation method.

CHAPTER THREE: CONFORMATIONAL CHANGES IN C-REACTIVE PROTEIN AFFECT BINDING TO CURVED MEMBRANES IN A LIPID BILAYER MODEL OF THE APOPTOTIC CELL SURFACE[1]

3.1 Introduction

As established in the previous chapter, C-reactive protein (CRP) is an acute phase protein that is released to trigger the complement immune response with two known conformational states. These two states are native pentameric CRP (pCRP) and modified CRP (mCRP). The results from the above experiments established a protocol to make a biologically relevant form of mCRP. Research in this chapter applies these biochemical findings by making mCRP with 0.01% SDS and heating for 1 hour at 80 °C for use in lipid experiments.

One main function of CRP involves binding to foreign or damaged material to signal degradation, allowing for removal of apoptotic cells to maintain self-tolerance. Native, soluble CRP (pCRP) is a homopentameric protein that binds to phosphatidylcholine (PC) lipids in a Ca^{2+}-dependent manner (96). Each monomer has a binding site for PC (22, 48). Conversion of pCRP into a modified form results in exposure of neoepitopes, leading to different reactivity. Modified CRP (mCRP) then

[1] Content for this chapter was modified from the journal article entitled "Conformational Changes in C-Reactive Protein Affect Binding to Curved Membranes in a Lipid Bilayer Model of the Apoptotic Cell Surface" by Aml A. Alnaas, Carrie L. Moon, Mitchell Alton, Scott M. Reed, and Michelle K. Knowles published in 2017 in the Journal of Physical Chemistry B. The DOI is: 10.1021/acs.jpcb.6b11505.

binds downstream to binding partners, such as Factor H, C1q, and C4bp, which regulate the complement immune response (55). The modified form is often identified as a monomeric form, but multimers of CRP or other forms could also play a role in CRP activity (36).

Beyond changes in molecular interactions due to conformational changes in CRP, conformational states have also been associated with different disease states. CRP levels have been linked to a wide variety of health issues, from cardiovascular disease (25, 97) and schizophrenia (98, 99), where high levels of CRP are related to negative outcomes, to autoimmune disorders, where increased CRP levels are likely protective (100–102). CRP is a marker of chronic inflammation (25, 48), and soluble pCRP is often measured to determine elevated levels that are correlated to health risks. However, it is thought that the modified form of CRP is the initiator of an inflammatory response in cells (30). Recent studies indicate that CRP plays a direct role in managing the inflammatory response to myocardial infarction, rather than just acting as a general marker of inflammation (103), with a monomeric form accumulating in plaque (104). Other recent work suggests that modified forms of CRP present in serum are related to obesity (60), and the monomeric form is also elevated in the eye during age-related macular degeneration (105). Despite the well-studied correlations between CRP forms and disease states, less is known about the molecular interactions of the different forms.

One primary role of CRP in the body involves the recognition of damaged membranes, a process that depends on CRP−protein and CRP−lipid interactions. mCRP binds C1q, which activates the complement response (106, 107); meanwhile, binding to

C4bp (32) and Factor H4 attenuates the immune response. In an acidic environment, CRP undergoes conformational changes that expose hydrophobic portions of the protein, and then, CRP binds oxidized low-density lipoprotein particles, C3b, and Factor H with higher affinity (62). The monomeric form of CRP has also been shown to bind integrin proteins on the cell surface and increase inflammation (58). In almost all studies, mCRP has been shown to bind other proteins better than pCRP. Some of this reactivity is thought to be regulated via an intrinsically disordered domain, and mutations in this sequence dramatically affect CRP binding to downstream partners (108).

Conformational changes in CRP clearly affect protein− protein interactions, but little attention has been given to how protein conformational changes affect lipid binding. It is interesting to note that phosphocholine is the predominant lipid head group in the outer leaflet of cell membranes yet CRP does not bind PC present on the surface of healthy cells. Beyond Ca^{2+}, it is not clear what is needed for CRP to bind to lipid membranes. Past work has shown that lysophosphatidylcholine (lysoPC) (96, 109), oxidized lipids (50), and cholesterol are required for pCRP binding (92). LysoPC and oxidized PC are commonly found in damaged membranes, like those found on apoptotic cells, and may provide a distinguishing feature between healthy and unhealthy membranes (110). However, others have shown using mimics of low density lipoprotein particles that neither lysoPC nor oxidized PC are needed; instead, CRP can recognize PC when it is presented on very small (radius <15 nm) nanoparticles (38). Both lipid composition and the presentation of lipids on curved surfaces likely affect CRP binding.

To identify how CRP recognizes and binds to damaged membranes, we designed curved membranes containing lipids that are typically present on the cell surface (PC, lysoPC) using a nanoparticle patterned surface with a fluid, supported lipid bilayer deposited on top. Lipid fluidity was measured using fluorescence recovery after photobleaching (FRAP) methods. Using quantitative fluorescence microscopy, we observed that the shape of the membrane alters CRP binding, with positively curved membranes recruiting more CRP than flat membranes. However, curvature-dependent, lipid binding depends greatly on the conformation of CRP. mCRP prefers curvature (radius of curvature, ROC = 27−55 nm), but the soluble pentameric CRP does not bind more than the CRP antibodies alone. Addition of lysoPC increases the accumulation of CRP to both flat and curved membranes, recruiting mCRP and pCRP to curved membranes more than bilayers containing only phosphatidylcholine. Interestingly, the highly curved membranes (ROC = 27 nm) bind mCRP to a lesser extent when compared to lower curvatures (ROC = 55 nm). Overall, the mechanism by which CRP recognizes membranes depends on the conformation, lipid composition, and shape of the membrane.

3.2 Method

Experimental Contributions

The majority of the research in this chapter was performed by Dr. Aml Alnaas. Mitchell Alton and Dr. Michelle Knowles contributed to image analysis coding and the processing of the images. Carrie Moon executed the dynamic light scattering experiment and a portion of the Biotin-X-DHPE experiment with some image analysis.

Materials

CRP was purchased from Academy Bio-Medical Company (Houston, TX) and stored at 4 °C. Monomeric CRP was made from CRP by adding 0.01% SDS and heating at 80 °C for 1 h in buffer, as previously described (40). Soy L-α-lysoPC (lysoPC) and 1-palmitoyl-2-oleoyl-sn-glycero-3-phosphocholine (POPC) were purchased from Avanti Polar Lipids (Alabaster, AL). Streptavidin labeled with Alexa 488, N-((6-(biotinoyl)amino)hexanoyl)-1,2-dihexadecanoyl-sn-glycero-3-phosphoethanolamine (Biotin-X-DHPE), red fluorescent (580/605) carboxylate modified fluospheres (d = 40 and 100 nm), Marina Blue 1,2-dihexadecanoyl-sn-glycero-3-phosphoethanolamine (MB-DHPE), and secondary goat anti-mouse immunoglobulin G with Alexa 488 were purchased from Thermo Fisher Scientific. Primary anti-C-reactive protein (C6 and D7 mouse monoclonal antibodies) and mouse IgG monoclonal antibody were purchased from Santa Cruz Biotechnology. Buffers used were PIPES buffer (2 mM CaCl2, 30 mM PIPES, 140 mM NaCl, pH 6.4) or HEPES buffer (30 mM HEPES, 140 mM NaCl, 2 mM CaCl2, pH 6.5). All remaining chemicals were purchased from Sigma-Aldrich.

Dynamic Light Scattering

To determine that CRP was not self-aggregating in storage, dynamic light scattering (DLS) was performed on a DynaPro Plate Reader II with Dynamics version 7 DLS software with a 384 well glass-bottom plate (Greiner Bio-One Sensoplate #781892). CRP was diluted to 500 μg/mL in PIPES buffer, and 50 μL each was placed into four wells for measurements. The plate was centrifuged at 200 rpm for 2 min. Settings for measurements were a 5 s acquisition time with autoattenuation at 25 °C. The solvent

setting for the system used was based on phosphate-buffered saline with a refractive index of 1.333 (at 589 nm for 20 °C) and a viscosity of 1.019 cP. Results are from three experimental days, where each measurement was in quadruplicate wells. The software used a Rayleigh Spheres model to fit the data, giving results for the hydrodynamic radius, % mass, and molecular weight (Figure 14).

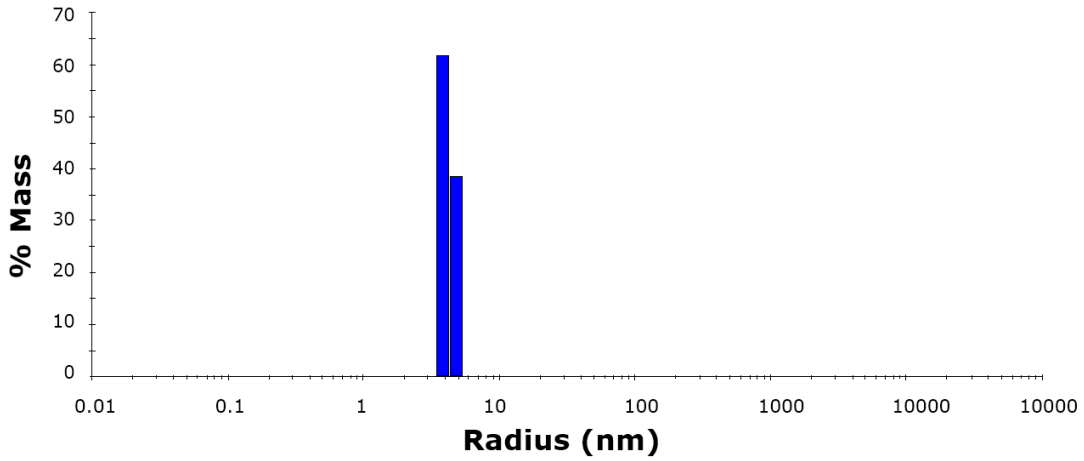

Figure 14. Dynamic light scattering of pCRP shows no aggregates. One example of a histogram of radii measured for pCRP is shown and representative of 12 measurements. 100% of the mass was less than 10 nm radius in all 12 samples measured. The average of 12 measurements was 4.4 +/- 0.3 nm radius and 110 +/-20 kDa for molecular weight. The error listed is the standard deviation.

Supported Lipid Bilayers

Supported lipid bilayers were made following previous methods (8). Briefly, the supported lipid bilayer was formed over fluorescent polystyrene nanoparticles (44 or 100 nm diameter Fluospheres from Life Technologies) deposited upon a flat glass surface (8 well plate from Lab-Tek Chambered Borosilicate Coverglass System, Thermo Fisher) at a density of 0.01−0.05 nanoparticles/μm^2. Liposomes were prepared by probe sonicating lipid films (0.125 mM lipids in PIPES buffer), and lipid bilayers were created by adding

100 μL of the sonicated lipid solution to each well followed by incubation at 37 °C for 1 h. CRP (50 μg/mL) was incubated with the lipid bilayer at 37 °C for 2 h. Membrane fluidity was tested with FRAP using MB-DHPE, as described in previous work (8), and confocal microscopy was performed to measure colocalization between nanoparticles and the protein. For labeling of CRP, the primary and secondary antibodies were preincubated together in 1:1000 ratios for 30 min at room temperature. Preincubated antibody solution (100 μL) was added to each well for a total volume of 200 μL. Two different primary antibodies were tested (D7 and C6).

Lipid films consisted of POPC, lysoPC, and MB-DHPE. The ratio of lipids included 0−3% lysoPC and 2% MB-DHPE, and the remainder was POPC. Specific ratios are stated in the text. For Biotin-X-DHPE samples, the ratio was POPC 99% and Biotin-X-DHPE 1%. Alexa488-labeled Streptavidin was added at a final concentration of 25 μg/mL.

Confocal Microscopy

A point-scanning confocal microscope (Olympus Fluoview) was used for FRAP experiments and for two-color imaging of red fluorescent nanoparticles and green fluorescent antibodies. For two-color imaging, the red and green fluorescence were taken sequentially to reduce bleedthrough with a 100× objective such that one pixel was equal to 124 nm. The red channel was excited with a 559 nm laser with an emission window of 575−675 nm. The green channel was excited with the 488 nm line of an argon ion laser with an emission window of 500−545 nm. When FRAP was performed, a 405 nm laser

was used to excite and photobleach MB-DHPE, and emission was detected from 425 to 475 nm.

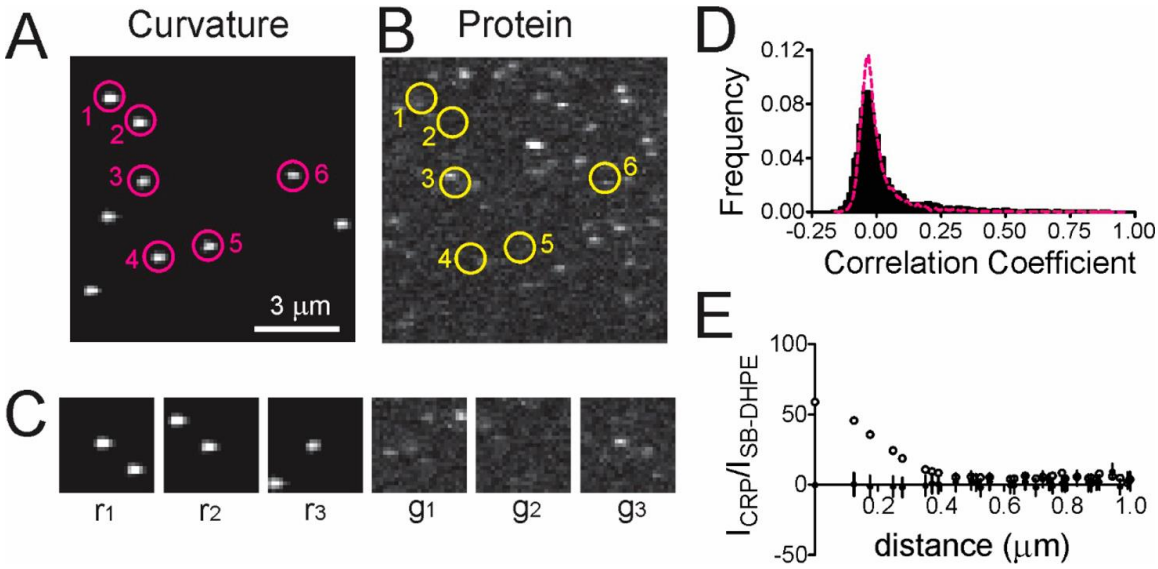

Figure 15. Supported lipid bilayers were created on a surface containing red fluorescent nanoparticles and then imaged after incubation with CRP. (A) Red fluorescent nanoparticle images mark sites of curvature. (B) Green fluorescently labeled protein (pCRP) is imaged separately. Red positions are located using a spot-finding algorithm and then cropped. Several positions are shown with circles. The same locations are cropped from the green image, shown in yellow circles, yielding pairs of images. (C) Three pairs of cropped images (3.1 μm wide). Panels r1−3 were cropped from A positions 1−3, and g1−3 were cropped from B. (D) The Pearson correlation coefficient is calculated for image pairs, and a histogram of all coefficients is plotted for pCRP at regions of curvature (black) and at random positions (magenta line). (E) A radial plot of the cropped images is calculated by averaging the normalized intensity of all pixels that are a certain distance from the center pixel, where a nanoparticle is located. Error bars are the SEM.

Image Analysis

Images were analyzed in MATLAB using location-guided colocalization methods, and the analysis is summarized in Figure 15. To find locations of curvature marked by red fluorescent nanoparticles, spot-finding methods were used based on freeware (111) that is designed from the methods of Crocker and Grier (112). Only the spot-finding portion of the code was used for this work. Locations were excluded if they were within 9 pixels of another location or within 12 pixels of the image edge. After

locations were identified, images were cropped from both red and green channels, yielding pairs of images. From the pairs of images, we measured first the distribution of Pearson's correlation coefficients and second the average radial plot of the green cropped images. This was done by averaging all pixels that are a specific distance from the center pixel. For example, there are four pixels that reside one pixel (124 nm) away from the center, and these are averaged to give the second data point. Four pixels that reside 175 nm from the center are averaged to give the third data point and so on. MATLAB code for the radial averaging function is available upon request. The intensity was normalized for each radial plot by dividing by an average radial plot of Alexa488 Streptavidin bound to Biotin-X-DHPE (SB-DHPE), which acts as a measure of the membrane surface area. The normalized intensity is termed $I_{CRP}/I_{SB\text{-}DHPE}$. After normalizing to SB-DHPE, the peak height (amount bound to curved regions), offset (amount bound to flat regions), and sorting ratio, I_{peak}/I_{offset}, were calculated for samples where binding to the flat areas was observable above the background (113). The offset was calculated by averaging all values in the radial plot greater than 0.75 μm away from the center. All error bars are the standard error of the mean (SEM).

The correlation function calculation was obtained from Dr. Justin Taraska (114). All other plots and significance testing were performed in GraphPad Prism (La Jolla, CA, U.S.A.).

3.3 Results

To determine whether or not CRP preferentially bound to curved membranes, supported lipid bilayers were created over a nanopatterned surface. Fluorescent

nanoparticles were deposited at a density of 0.01−0.05 nanoparticles/μm^2 onto a cleaned glass surface. Then a bilayer was created on top using liposome deposition methods. CRP was incubated with the curved membrane surface and labeled with green fluorescent antibodies. Two-color, confocal imaging was performed to determine whether or not CRP bound to curved membranes. The red fluorescent nanoparticles mark locations of membrane curvature, as demonstrated in previous work (8). The green fluorescent channel relates the amount and location of CRP. The sample shown in Figure contains CRP from human serum, the soluble, pentameric form commonly detected in medical diagnostics for inflammation. The lipid bilayer is composed of MB-DHPE (2%) and POPC (98%), a common lipid on the cell surface, with regions of curvature that have a radius of curvature (ROC) of 55 nm.

To quantify imaging data, nanoparticles were identified using a spot-finding algorithm (112). Nanoparticles that were separated by more than 9 pixels from other nanoparticles and more than 12 pixels from the edge of the images were selected and cropped to 3.1 μm × 3.1 μm (25 × 25 pixel) images (Figure 15A). The same locations were cropped from the CRP channel (Figure 15B), and three examples of single cropped images are shown (Figure 15C). In CRP images, the intensity is variable with hazy fluorescence shown in g1, the background level of fluorescence in g2, and a fluorescent spot near a nanoparticle position in g3, whereas there is always a clear spot for the nanoparticle in images r1−3. Because nanoparticles are very bright relative to the background and monodisperse in both size and intensity, it is straightforward to automate the identification of curved membrane locations. The identification of regions of

curvature first allows us to automate our analysis using location-guided colocalization methods (8, 114, 115). This method of data analysis yields pairs of images, like those in Figure C, which can be further analyzed to obtain distribution information or averaged to obtain bulk information.

From individual pairs of images, the Pearson correlation function was calculated to relate how similar the two images are, with −1 being images that are opposites and +1 being those that are identical. The distribution of correlation values is plotted as a histogram, and very little is observed to be correlated in samples containing pCRP and curved POPC bilayers (Figure D, black bars). Random positions have a similar distribution (Figure D, magenta curve). The correlation function is useful for colocalization measurements, but the intensity information is lost; therefore, we performed another measurement that retains information related to the amount of protein present at nanoparticle regions. From the individual cropped, green (CRP) images (n = 3297), a radial plot of the normalized intensity as a function of the distance from the center pixel was calculated (Figure E). This was done by averaging all pixels that are the same distance from the center, as described in the methods. After subtracting the background intensity, the intensity of samples lacking green fluorophores, data were normalized by dividing by the radial plot of SB-DHPE, which acts as a general membrane marker (Figure 16). In the radial plot, there are two pieces of information: the peak height (distance = 0 μm) and the offset (distance > 0.75 μm). The height is a measure of the amount of fluorescence at regions of curvature, and the offset is a measure of the fluorescence due to binding to flat membranes. These methods of analysis are used

to quantify how the lipid composition, protein conformation, and membrane shape separately affect CRP recognition of membranes.

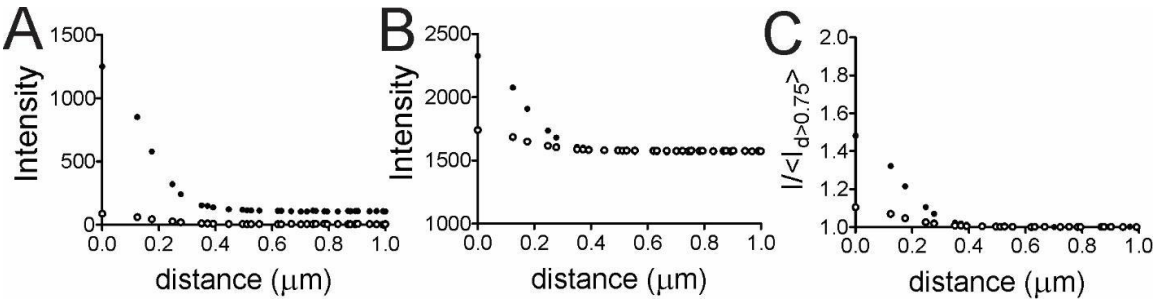

Figure 16. Radial plots used to calculate surface area normalized radial plots. A) The raw intensity measurement of mCRP (black dots) and pCRP (open circles) at regions of curvature with radii of 55 nm. B) The raw intensity measurement of Alexa488 labeled Streptavidin attached to Biotin-X-DHPE at 55 nm (black circles) and 29 nm (open circles). The background intensity of samples containing no green probes was subtracted from both A and B. C) Strep-Biotin-X-DHPE (SB-DHPE) at 55 nm (black circles) and 27 nm (open circles) was normalized by dividing by the average intensity for all pixels at a distance 0.75 of greater from the region of curvature. To calculate Figures in the text that contain normalized data, $I_{CRP}/I_{SB\text{-}DHPE}$, plots like those in A are divided by those in C based on the ROC.

CRP Conformation Affects Binding to Curved Membranes

The conformation of CRP affects binding to downstream proteinaceous partners, such as C1q and Factor H (25). Here we tested whether CRP conformation affects lipid binding to both curved and flat regions of the membrane. Supported lipid bilayers containing 98% POPC and 2% MB-DHPE were formed over top of a fluorescent nanoparticle patterned surface (ROC = 55 nm) and then incubated with CRP and CRP antibodies. The monomeric form of CRP (mCRP) was made as previously described (40). In this preparation, the tertiary structure remains intact, as demonstrated by the ability of mCRP to bind downstream partners of the complement immune response in a way that acid-treated or fully denatured CRP does not (40). Visually, mCRP shows high colocalization to nanoparticle sites and is also present in flat regions when compared to pCRP (Figure 17A). The average of the cropped, nanoparticle images shows a spot in the

center, as expected. All images, except the red fluorescent nanoparticle image, are scaled identically and linearly for direct comparison. A spot appears in the center for mCRP, pCRP, and samples with no CRP (containing only antibodies, termed “none”) but not for samples where the surface has been blocked with bovine serum albumin (BSA) instead of CRP or when random regions are chosen instead of nanoparticle regions.

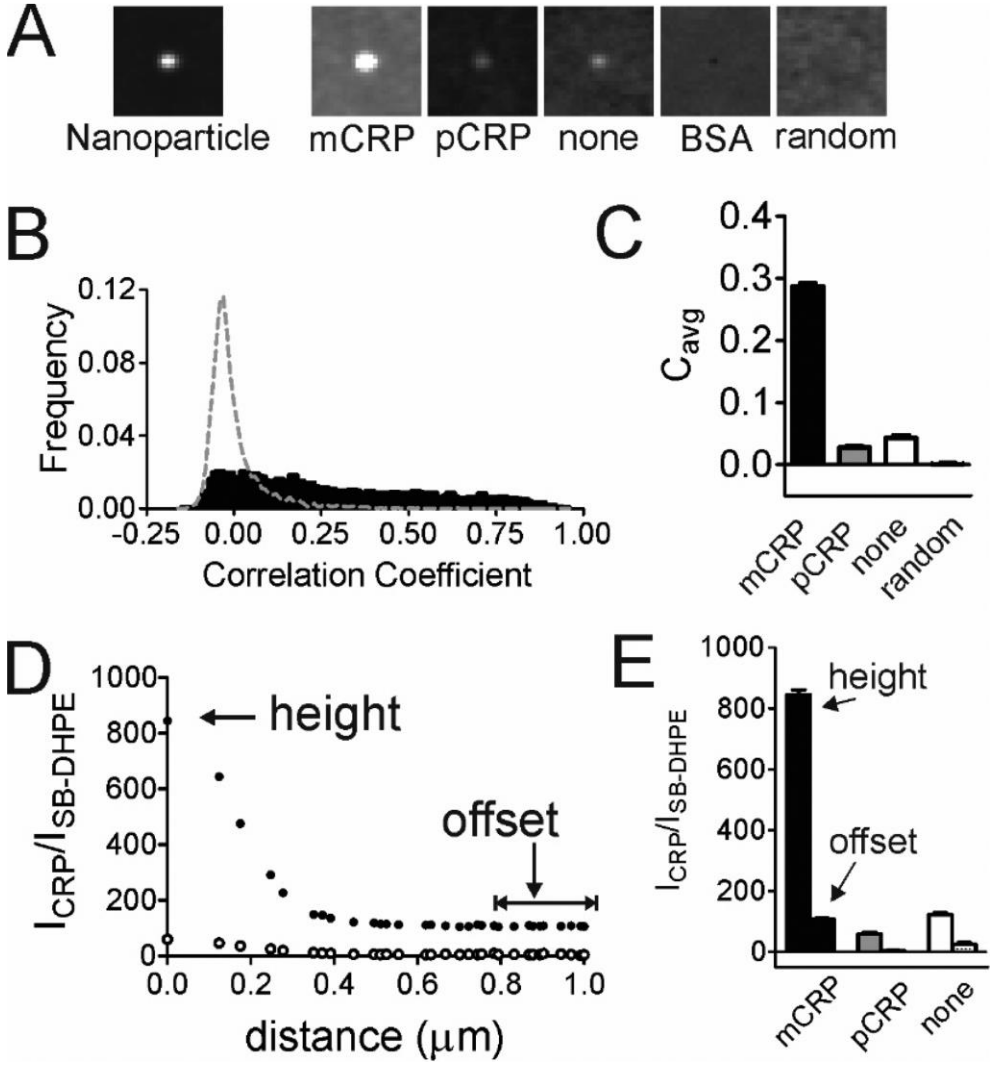

Figure 17. Monomeric CRP and pCRP were incubated on curved supported lipid bilayers and then imaged using confocal microscopy. (A) Average images of nanoparticles, mCRP, pCRP, samples with antibodies only ("none"), and BSA-blocked samples with antibodies and no CRP ("BSA") have been cropped from regions selected from nanoparticle positions. Random positions were also selected and cropped. The images are all scaled linearly and identically. (B) The distribution of correlation coefficients for pairs of cropped images is measured for mCRP (black) and randomly selected positions in a pCRP sample (gray dashed line). (C) The average of the distribution is plotted for mCRP, pCRP, images with antibodies alone, and CRP at random regions instead of curved membrane regions. (D) From the images, the intensity is averaged radially and normalized to show the accumulation of mCRP (black circles) and pCRP (open circles). (E) The height and the offset are plotted for each radial plot. In all bar graphs, the error is the SEM.

To assess the interaction between CRP conformers and curved membranes further, correlation coefficients were calculated from pairs of cropped images (Figure 17B). mCRP (black bars) and pCRP (Figure 15D) are clearly different; mCRP has a higher correlation to the nanoparticle positions, suggesting higher preference for curvature. The average correlation coefficient is 0.29 for mCRP (Figure 17C), and this is due to a large diverse distribution (Figure 17B). pCRP has an average of 0.03, which is similar to samples where no CRP has been deposited. Randomly chosen positions show near-zero correlation.

Monomeric CRP accumulates at a curvature, and the amount of fluorescence at nanoparticle positions is quantified from the average radial distribution of the cropped images (Figure 17D). The normalized radial average shows that mCRP binds both flat regions, as observed by the offset, and nanoparticle regions, observed by the peak height, better than pCRP. pCRP has no measurable signal above background for flat regions and is similar in intensity to antibodies alone at regions of curvature, suggesting that pCRP does not bind membranes well. The increase in fluorescence at curvature relative to the background is shown as a bar graph of the peak height and offset intensity for mCRP, pCRP, and no CRP present (Figure 17E). The height is the first point in the radial curve. The offset is measured from the average for all distances from 0.75 to 3.1 μm away from the center, a distance greater than the spread of the intensity in the center but less than the nearest-neighbor distance. In Figure 17E, the average peak height and offset of all cropped images are plotted, and both are higher for mCRP relative to those for pCRP.

Lysophosphatidylcholine Increases CRP Binding to Membranes

The presence of lysoPC has long been known to enhance CRP binding to the surfaces of artificial bilayers (96). To investigate how changes in the chemical composition affect CRP binding, supported lipid bilayers that contained 3% lysoPC, 2% MB-DHPE (to measure fluidity), and 95% POPC were created over a nanopatterned surface where both flat and curved membrane regions were measured simultaneously. The presence of lysoPC increased the Pearson correlation coefficient for both pCRP and mCRP (Figure 18A, B). In both cases, there was an increase in the distribution at larger coefficients. In Figure 18C, the average correlation coefficient is shown relative to random positions, and a dashed line indicates the position without lysoPC (shown in Figure 15D and Figure 17B). There is an increase by approximately 0.1 for both forms of CRP, suggesting that lysoPC enhances binding to curved regions.

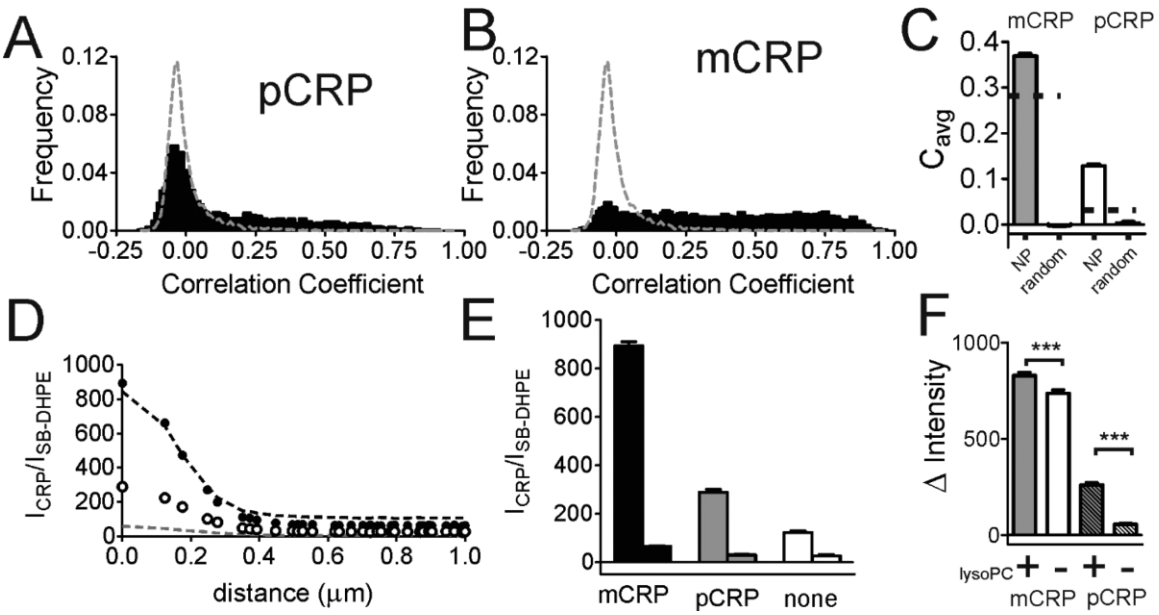

Figure 18. CRP was incubated with lysoPC containing membranes (LysoPC: POPC: MB-DHPE at a 3:95:2 molar ratio) that had regions of curvature (ROC = 55 nm). From cropped images, the Pearson correlation coefficient was calculated for (A) pCRP (black bars) and (B) mCRP (black bars). The gray dashed line in both plots denotes the distribution of the correlation coefficient of protein to regions of curvature in randomly selected positions in pCRP samples. (C) The average value of the correlation function distribution is shown with the SEM for both nanoparticle and random positions. The dashed line shows the average value when lysoPC is not in the membrane and nanoparticle positions are selected. (D) Normalized radial averages of mCRP and pCRP binding to sites of curvature. mCRP and pCRP binding to lysoPC bilayers (black circles and white circles, respectively), mCRP (black dashed line), and pCRP (gray dashed line) on bilayers without lysoPC. (E) The peak height and offset are plotted side by side for mCRP, pCRP, and no CRP. (F) The difference between the height and offset, ΔIntensity, for mCRP (solid) and pCRP (striped) with and without lysoPC.

To determine how much CRP accumulates at nanoparticle regions when lysoPC is present, the intensity of CRP fluorescence was quantified (Figure 18D−F). The height of the radial plot of mCRP increases only slightly, as shown in Figure 18D, where the black dashed line is the radial plot without lysoPC and the black circles are that with lysoPC. The height of the radial plot of pCRP at nanoparticles increases approximately 4-fold, as shown in Figure 18D, E, where the gray line is the radial plot of pCRP without lysoPC

and the open circles depict the radial plot in the presence of lysoPC. The difference in normalized intensity between flat and curved regions, ΔIntensity (Figure 18F), is significantly higher ($p < 0.05$) for both mCRP and pCRP, indicating that lysoPC serves to increase binding of all forms of CRP to curved regions more so than that to flat regions but affecting pCRP more than mCRP.

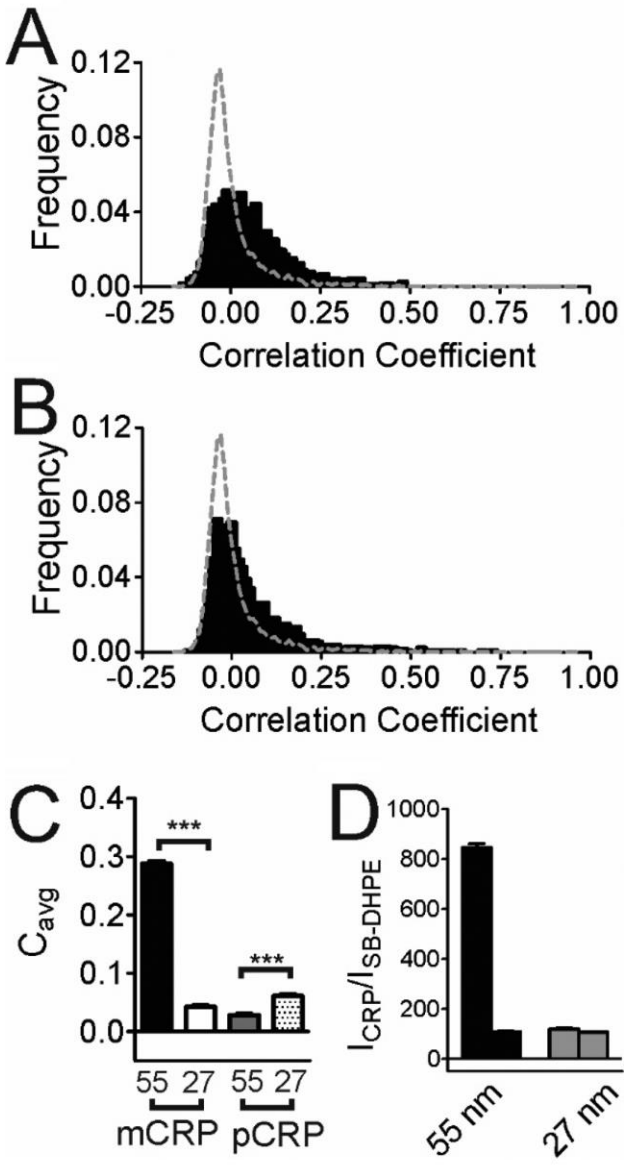

Figure 19. CRP was incubated with supported lipid bilayers with a smaller nanoparticle support (d = 44 nm, ROC = 27 nm) and imaged using confocal microscopy. Lipid bilayers contained 98% POPC and 2% MB-DHPE. (A) Pearson correlation coefficient distribution for pCRP and nanoparticle images (N = 1574), on samples containing a ROC = 27 nm. (black). (B) Pearson correlation coefficient distribution for mCRP and nanoparticle images (N = 1368) on samples containing a ROC = 27 nm (black). The gray dashed curves in both (A) and (B) are from randomly selected positions in a pCRP sample. (C) Average of the correlation coefficient as a function of curvature. (D) The peak height (normalized intensity at d = 0 μm) and offset (normalized intensity at d = 0.75−3.1 μm) for mCRP at 27 and 55 nm were measured from the normalized radial plot. Error bars are the SEM.

Membrane Shape Affects CRP Binding

The shape of a membrane has been shown to affect protein binding for a variety of membrane-associated proteins, such as BAR domains (116), amphipathic helices (16, 117), and lipid-anchored proteins (118, 119). By decreasing the size of nanoparticles used as a template for the supported lipid bilayer, higher curvatures (ROC = 27 nm) were examined. The Pearson correlation coefficient distribution (Figure 19A, B) was affected by membrane shape for both conformations. The distribution shifted to slightly higher, more colocalized coefficients for pCRP (Figure 19A), whereas the shift was to lower coefficients for mCRP (Figure 19B). The average correlation coefficients for both mCRP and pCRP are shown (Figure 19C), and a statistical difference in colocalization is observed for both conformations. However, the change in pCRP accumulation is small, with pCRP slightly favoring higher curvatures relative to the large change in mCRP accumulation, where mCRP favors lower curvatures. The results were similar when 3% lysoPC was included in the bilayer (Figure 20).

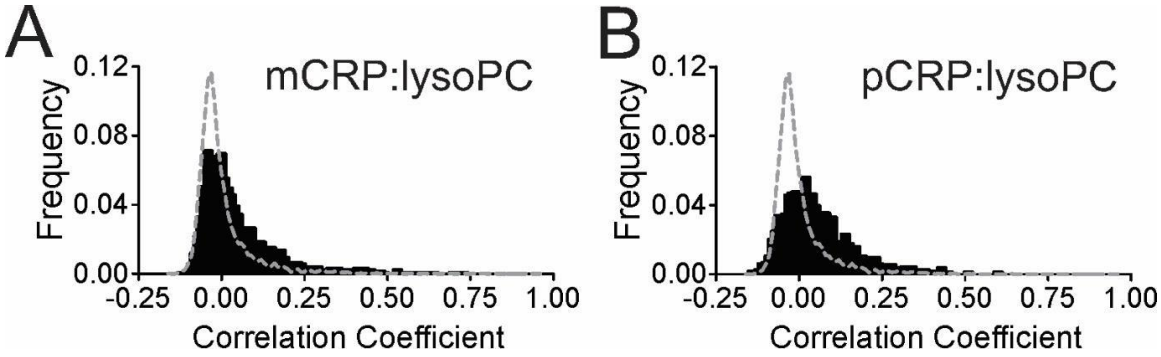

Figure 20. CRP recruitment to curvature with a smaller nanoparticle support (d = 44 nm, ROC = 27 nm) was measured using confocal microscopy. Lipid bilayers contained 95% POPC, 3% LysoPC, 2% MB-DHPE A) The Pearson's correlation coefficient distribution for mCRP and nanoparticle images at a ROC of 25 nm (black bars). B) The Pearson's correlation coefficient distribution for pCRP and nanoparticle images at a ROC of 25 nm (black bars). In both plots, the gray curve is the distribution of correlation values for randomly selected positions.

The accumulation of mCRP at regions of curvature was quantified by comparing the binding of mCRP to flat regions (offset) to the binding of mCRP to regions of curvature (peak height) after normalizing the radial plots with SB-DHPE (Figure 19D,Table 3). The sorting coefficient was calculated by dividing the normalized peak intensity by the intensity measured in the offset, and these coefficients are summarized in Table 4. Sorting coefficients were not calculated for pCRP because the binding of pCRP to flat regions was close to 0 after background subtraction and not greater than the binding of free antibody to flat membranes.

Table 3. Summary of mCRP and pCRP Accumulation at Curved and Flat Regions [a]

	I_{flat}	**I_{peak} @ ROC 55 nm**	**I_{peak} @ ROC 27 nm**
mCRP	108 ± 3	844 ± 17	119 ± 4
pCRP	4 ±2	59 ±6	56 ± 2
$mCRP_{lyso}$	65 ± 3	893 ± 17	n/a
$pCRP_{lyso}$	29 ± 2	289 ± 11	n/a

[a]*The intensity was normalized by dividing by the intensity of SBDHPE, as described in Figure .*

Both the increase in intensity at the peak relative to the flat regions and the average correlation coefficient convey that mCRP collects at larger nanoparticles (lower curvature) at a density greater than the accumulation at smaller nanoparticles (higher curvature). However, pCRP binds membranes minimally, unless lysoPC is present, in agreement with the work of others (96, 120). The shape of a membrane clearly affects CRP binding, and this depends on the form of CRP. The mechanism by which mCRP and pCRP interact with membranes is likely different.

Table 4. Sorting Coefficients for mCRP [a]

	ROC 55 nm	ROC 27 nm
mCRP	7.8	1.1
mCRPlyso	13.7	n/a

[a]*Sorting coefficients, Ipeak/Ioffset, are determined by dividing the normalized peak intensity by the normalized flat intensity.*

3.4 Discussion

The physiological activity of CRP depends on its ability to bind membranes and trigger an immune response. Others have demonstrated that the conformational state of CRP affects protein binding (24, 32, 58) and the subsequent regulation of an inflammatory response by the complement cascade (107), but little is known about how lipid interactions are affected by alterations in CRP conformation. In our work, we measured CRP accumulation on membranes, focusing on a commonly prepared monomeric form and the native, pentameric form. The ability of the different forms to bind membranes of varying shapes and lipid composition was examined using a nanoparticle- based assay that allows for separate adjustment of the shape and chemical composition. The following conclusions can be drawn from the data to further characterize the mechanism by which CRP identifies damaged membranes in the body.

Conformation of CRP Affects Binding to Curvature. The modified form of CRP binds lower curvatures (ROC = 55 nm) more effectively than pCRP (Figure 15 and Figure 17). We hypothesize that the mechanism by which mCRP binds curvature better than pCRP is driven primarily by hydrophobic regions of CRP being exposed once the pentamer begins to dissociate (36, 92, 121). The faces that connect the protomers in the pentameric form are enriched in hydrophobic amino acids that preferentially insert into membranes or aggregate. Other proteins, such as amphipathic helices, preferentially

insert into curved membranes through hydrophobic interactions with the defect sites that form as a lipid membrane bends around a curved surface (118). These defect sites are thought to allow exposure of the hydrophobic tails to the surrounding aqueous solution and potentially interact with hydrophobic proteins. However, defect site binding to membranes alone cannot explain the clear preference that mCRP has for lower curvatures over higher curvatures and flat membranes (Figure 19, Table 4). The current model of defect site binding suggests that more defect sites exist as a membrane bends with higher curvature. Therefore, defect site binding proteins, like lipid-anchored proteins and amphipathic helices, bind higher curvatures better than lower curvatures (16, 118, 119). Defect site-based curvature sensing predicts a linear dependence of the sorting ratio (I_{peak}/I_{offset}) on 1/ROC (122). This trend differs from the curvature preference of mCRP binding, where mCRP prefers moderate curvature over high or flat regions. The driving force in defect site binding is the reduction in free energy of the system unless other mechanisms (described below) are acting on the system to create an optimal curvature for protein binding.

One mechanism by which a specific or optimal shape preference comes about is from a 3D protein structure that has an intrinsic curvature, like a BAR domain (116) or a clathrin coated pit (123). These larger structures act as a driving force for sorting of the protein at sites of curvature. These structures then prefer lipid membranes that match in shape to their intrinsic curvature. mCRP could form larger oligomers on membranes that give rise to structures with a specific curvature preference. It is possible that higher-order structures are what drive CRP binding and these structures form better on membranes

with a radius of curvature of 55 nm as opposed to 27 nm. A second mechanism by which specific shapes of membranes could be sensed involves molecular crowding. For example, the protein CALM, a clathrin adapter protein, has a preference for binding 90 nm diameter liposomes (124). CALM shows this preference by using an amphipathic helix to insert into defect sites, and CALM itself is not thought to form higher-ordered structures. Instead, the packing into defect sites is limited by molecular crowding of the rest of the protein as it binds only on one leaflet. In the same way, mCRP could insert hydrophobic portions into defect sites but be limited from fitting more due to crowding. We see no direct evidence of higher-ordered structures in our assay, but curvature sensing of a specific size could arise from a multimeric mechanism or a mechanism by which molecular crowding limits the protein density at higher curvatures.

An alternative interpretation for the observation of specific curvature sensing in the data could arise from the conformational state of the protein being different when bound to 55 nm curved sites than higher curvature membranes. It is possible that the conformational state of CRP exposes neo-epitopes when bound to 55 nm curved membranes and these neoepitopes have a higher affinity to antibodies. It is well-known that different CRP conformers bind differentially to CRP antibodies (125, 126) and CRP conformation is affected when directly labeled (59). If the observed accumulation at curvature is an effect of protein state, this would be physiologically relevant to the inflammation field, where the state of CRP at sites of inflammation, like plaque, is unclear. Changes in conformational state would likely affect downstream binding in the complement cascade and with cell surface receptors, as others have shown when

comparing mCRP and pCRP (24, 127). Further studies of CRP reactivity to C1q, C4bp, and Factor H while on a wide range of curved membranes could elucidate whether these CRP clusters have unique physiological relevance and what the optimal curvature is for CRP clustering and/or neoepitope exposure.

In sharp contrast to mCRP, we see a lack of pCRP binding to curvatures containing only POPC (Figure 15 and Figure 17). This agrees with the fact that pCRP does not bind healthy cells and does not accumulate well on PC containing liposomes (96, 104, 120). However, once the membrane curvature was increased (ROC = 27 nm), pCRP exhibited a slightly higher accumulation at curved membranes regions (Figure 19A−C). This is in agreement with past work on CRP (38) where very high curvatures (ROC = 10−15 nm) were tested and shown to bind pCRP better than lower curvatures (ROC = 20−35 nm). However, in this past work, the lower curvatures likely bound pCRP to a lesser extent, below the detection level for the binding assay used, based on the fact that CRP was activated in some way to be able to bind C1q after incubation with curved membranes (38). All binding was Ca^{2+}-dependent, indicating that the pCRP/PC interaction was likely through binding of the PC moiety as opposed to an interaction with the lipid tails. Although we observe a small increase in pCRP colocalization at membrane locations with a ROC of 27 nm relative to 55 nm, it is likely that pCRP binds better to higher curvatures than those measured here, like others have shown.

Lipid Composition Affects Binding to Membranes

The membrane association of pCRP is also enhanced by changes in the lipid composition. Once lysoPC is added to the lipid bilayer, pCRP binds at a higher density to

curved regions (Figure 18). This is consistent with the fact that CRP does not bind healthy cells that contain lipids similar to POPC. Damaged membranes often contain modified lipids, and modifications that convert PC to lysoPC on the cell surface are required for recruiting CRP to cells or particles that need clearance (96, 120). In our work, lysoPC enhances binding more at curved regions than on flat regions, as shown by the increase in height of the radial plots in Figure 18D−F. This could be due to the accumulation of single-tailed lipids, like lysoPC, at sites of curvature (8); there is a higher density of lysoPC at the curved regions to associate with CRP. Others have suggested that lysoPC introduces irregularities into artificial lipid bilayers (96) and that these features are essential to binding pCRP.

The presence of lysoPC affects pCRP more than mCRP, increasing the accumulation by 4-fold as opposed to a 10% increase at curved membranes (Figure 18F). This suggests that mCRP associates in a way that does not depend on binding lysoPC, whereas pCRP association does. pCRP likely interacts through head group interactions within the Ca^{2+}-dependent PC binding site, as others have observed on highly curved membranes lacking lysoPC (38). However, the mechanism by which pCRP binds membranes may be different when lysoPC is present. Recent work suggests that pCRP has a non-Ca^{2+}-dependent, lysoPC binding site, on the side opposite the PC binding site (109). This site could be lost upon monomerization, leaving mCRP to interact with membranes primarily through hydrophobic insertion.

3.5 Summary

In summary, we utilized a nanopatterned substrate to introduce curvature into continuous lipid bilayers for quantitative image analysis of CRP−lipid interactions. One major advantage of this assay is the ability to separately tune chemical composition and membrane shape (8). This work demonstrates that the conformational state of CRP affects lipid binding. Monomeric CRP readily associates with membranes, favoring sites of curvature over flat regions. Native pCRP does not easily associate with membranes until the curvature is high, likely higher than that tested here, or until lysoPC is introduced. CRP likely recognizes damaged lipidic materials through a mechanism that combines PC head group binding by pCRP and membrane insertion into defect sites, which stabilizes the conformational conversion to mCRP. Both of these types of interactions are potentially strengthened at sites of curvature and could aid in CRP's role in recognizing damaged membranes in the body.

CHAPTER FOUR: NOVEL MODIFICATIONS TO A NANOPARTICLE PATTERNED SUBSTRATE ASSAY

4.1 Introduction

Experiments studying binding of CRP to curved membranes show the ability of the nanoparticle patterned substrate assay outlined above to be applied to studying a system where peripheral membrane proteins bind to a membrane. Other systems where membrane curvature may play a role in protein binding include BAR domains and membrane trafficking (16, 124, 128). The method for a membrane curvature assay published by our lab involves first depositing nanoparticles for a patterned substrate followed by a deposition of liposomes to form a supported lipid bilayer (8). Others have shown the advantages of using colloidal lithography to deposit nanoparticles, which can be followed by a layer of silicon dioxide through sputter coating (129). This chapter focuses on experiments that combine these two methods to allow for the reuse of the patterned substrate as well as the ability to use it with cellular experiments.

A challenge with sputter coating is that a flat coverglass must be used. The addition of fabricated silicone or 3D printed chambers to the coverglass system allows for less volume. 3D printing is becoming more accessible, as seen by the dedicated website of the NIH 3D Print Exchange (https://3dprint.nih.gov/). There are currently no 3D printing files for chambers available, so the chambers designed here will be a valuable addition and option for scientists.

In addition to being a patterned substrate, the use of fluorescent nanoparticles has the added functionality to be able to be used for colocalization analysis beyond simply inducing curvature. Inducing curvature into cells is a new concept and could be useful for studying processes like endocytosis and exocytosis to see if certain proteins sort to sites of curvature. By sputter coating a thin layer of silicon dioxide on top, the nanopatterned substrate is not only reusable, but also works with many assays, such as atomic force microscopy (AFM) and colocalization analysis using supported lipid bilayers and a fluorescent probe. In depth colocalization analysis of different lipid bilayer compositions are shown here.

4.2 Method

Experimental Contributions

Alan Weisgerber did the deposition and melting of most of the nanoparticle patterned coverglass used here. Dr. Xin Fan (University of Denver, Physics and Astronomy) performed the sputter coating. Dr. Michelle Knowles and Mitchell Alton contributed the majority of the MATLAB code. All other experiments and data analysis were completed by Carrie Moon.

Materials

Attofluor cell chambers (Invitrogen A-7816) are stainless steel, autoclavable holders for 25 mm round coverglass. These were used for deposition of 0.1 μm fluorescent polystyrene nanoparticles (Thermo Fisher fluospheres) for cellular and supported lipid bilayer imaging experiments. Yellow-green fluospheres (Thermo Fisher

F8803) were used for AFM experiments and red fluospheres (Thermo Fisher F8801) were used in the other experiments performed here.

Silicone Rubber Chambers

Silicone rubber baking mats were cut into a shape with four chambers to fit on top of a coverglass inside the Attofluor chamber. The overall shape was designed to have four circular chambers with a small triangular notch near the top (for orientation when imaging). Silicone rubber was cut using an electronic die cutting machine (Cricut Personal/V1). Superglue was used to adhere the silicone rubber to the glass with a semi-permanent bond. Experimental working volume was 20 µL per well with an overall total volume of 30 µL maximum for a droplet shape. This allows for washing off liposomes with the addition and removal of 5 µL. Due to the small volumes, some evaporation occurred during lipid incubation and extra buffer was added (5 µL) as needed.

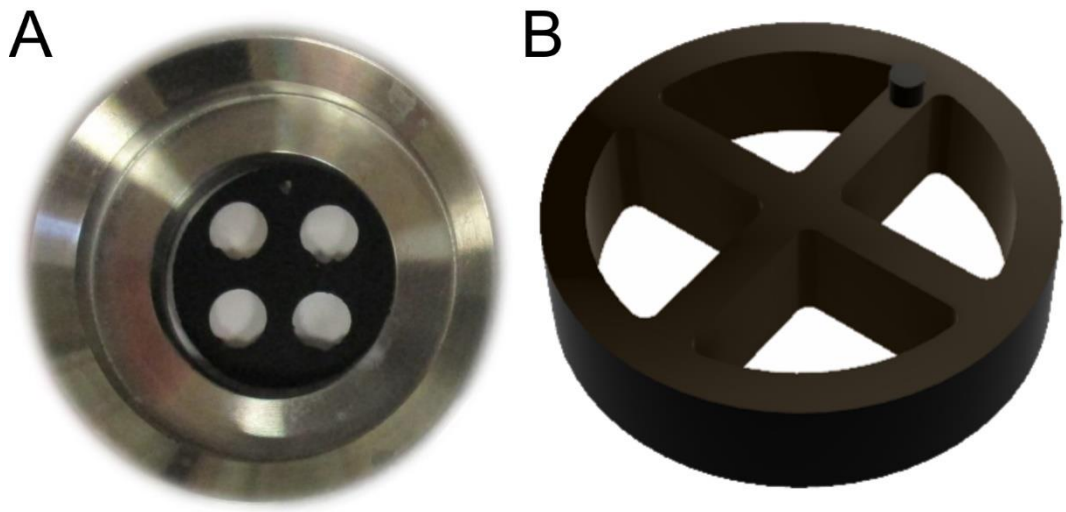

Figure 21. Chambered holders designed for different well volumes. A) Silicone rubber miniature chambers have a 20 µL working volume. B) Walled 3D printed chambers have a 75 µL working volume.

3D Printed Chambers

A chambered structure with walls was designed in Autodesk Fusion 360 software to have 4 pie shaped wells. Wells were designed to fit on top of a coverglass after it has been inserted into an Attofluor holder. 3D prints were made using a Prntrbot Plus (Model 1504) with 1.75 mm polyethylene terephthalate (PETG) filament (Maker Geeks HD Black Glass). PETG plastic was chosen over acrylonitrile butadiene styrene (ABS) or polylactic acid (PLA) filament due to strength, low odor, and environmentally friendly properties. Prints were done using Ultimaker Cura 15.04 software (https://ultimaker.com/en/products/cura-software) with settings of 50% fill density, 0.1984 mm layer height, 0.8 mm shell thickness, 40 mm/s speed. The printing temperature was optimized to 240 °C. 3D prints were glued on with silicone elastomer epoxy (Sylgard 184, used at a 10:1 ratio) or superglue for a semi-permanent bond or with Gorilla brand epoxy for a permanent bond. Once 3D print was placed, the epoxy or glue was allowed to set at appropriate curing times and temperatures (10-20 minutes at room temperature or 1 hour at 80 °C). The prints with coverslips attached were handled with tweezers and the underside was inspected for areas that did not seal. Fresh epoxy or glue was pushed under in those areas with a toothpick and allowed to cure again. Total maximum volume in each well is 100 µL, with a working volume of 75 µL, allowing for the addition of 25 µL for a liposome wash.

Nanoparticle Patterned Coverglass

In the Attofluor chamber, nanoparticles were deposited on a cleaned 25 mm round coverglass using previously established protocols and concentrations (see Appendix A)

(8). Nanoparticles were allowed to incubate for 15 minutes at room temperature before being placed in a 100 °C oven for 10 minutes. After heating, the coverglass is rinsed 5 times with deionized water.

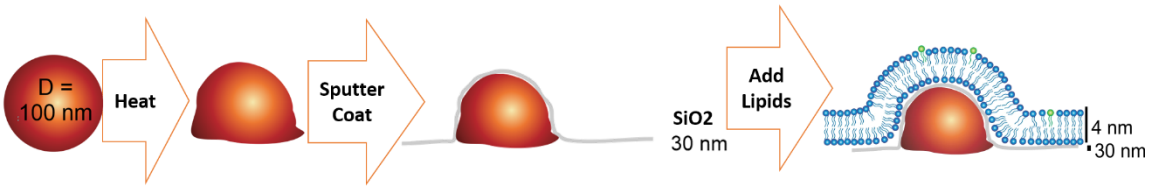

Figure 22. Illustration of modification to nanopatterned substrate for curvature assays. Fluorescent nanoparticles (radius 50 nm) have been used previously to induce curvature with supported lipid bilayers. The method outlined here has the addition of heating to melt the nanoparticles slightly and of a 30 nm silicon dioxide coating. Figure not drawn to scale. Lipid bilayers are approximately 4 nm.

Nanoparticle patterned coverglass was attached to sputter coat stage with Kapton tape. A Phase II J sputter coater (AJA International, Inc.) was used to deposit 30 nm of silicon dioxide (Figure 22, 2300 s at 0.13 Å/s deposition rate). Some coverglass had the addition of a 5 nm titanium coating (80 s at 0.63 Å/s) on top of the silicon dioxide.

Atomic Force Microscopy (AFM)

AFM of nanoparticles sputter coated with both silicon dioxide and titanium was performed at the University of Denver using an Asylum Research MFP-3D instrument with AR v13 software (Bruker probe MSNL-10, Figure 25). Image analysis and measurements were done with Gwyddion software.

AFM was also done with a Bruker Resolve instrument located at Colorado State University in Fort Collins, CO. For these experiments, a ScanAssyst Air probe was used and analysis was done with Nanoscope Analysis 1.8 software. Samples tested had 30 nm silicon dioxide and 5 nm titanium sputter coating (Figure 25) or no sputter coating at all

(just melted nanoparticles, as seen in Figure 26). Gwyddion software was used to calculate the roughness of the sputter coated flat region.

Cell Culture Experiments

PC-12 gr5 cells (ATCC) were grown in T-25 or T-12.5 flasks (Nunclon) with Dulbecco's Modified Eagle Media (Life Technologies 11965) containing 5% fetal calf serum (Fisher SH3007403), 5% horse serum (Fisher SH3007203), and 100 µg/mL each of penicillin and streptomycin (Fisher ICN1670049). Cells were split or plated when at 80% confluence with pipetting up and down to break up clumps. Versene (Thermo Fisher 15040066) was used to detach cells from flasks. Polylysine (Sigma PL4707) was used to coat the coverglass with an incubation time of 20 min at room temperature. Coverglass was then washed 3 times with sterile PBS (Life Technologies 14040) prior to plating cells. Cells were allowed to adhere and grow overnight. Manufacturer's instructions were followed to stain membranes with Cellmask in green or deep red (Life Technologies C37608 or C10046).

Supported Lipid Bilayer Analysis

The protocol used here was modified from a previously published method (8) and a detailed version of that protocol can be found in Appendix A. The modifications included no Hellmanex and no deposition of nanoparticles (already deposited and sputter coated). Each experiment starts with washing the sputter coated substrate with buffer (15 mM HEPES, 100 mM sodium chloride, 2 mM calcium chloride, pH 7.4). If using customized chambers, the volume used in the working volume listed above or a volume of 500 µL, if using only the Attofluor chamber. Lipid incubation and rinsing off

liposomes is also the same except for the volumes being chamber size dependent. After imaging is over, wells are cleaned for reuse. Cleaning steps include removal of lipid-buffer solution, incubating with the appropriate maximum volume of 1% SDS for 5 minutes, and washing 3-4 times with deionized water. Wells are left empty, allowed to dry, and stored in an individual covered and labeled container for later use. The containers that were found to work well are two small weigh boats taped together to form a clam shell configuration. Lipid structures in the compositions used here are illustrated below. Lipid film compositions contained 92-98% POPC, 0-5% cholesterol, 0-1% DOPE-PEG 2000 and 2% MB-DHPE or 2% Fluorescein DHPE (FL-DHPE). All lipids were purchased from Avanti Polar Lipids, with the exception of MB-DHPE and FL-DHPE which were purchased from Thermo Fisher Scientific.

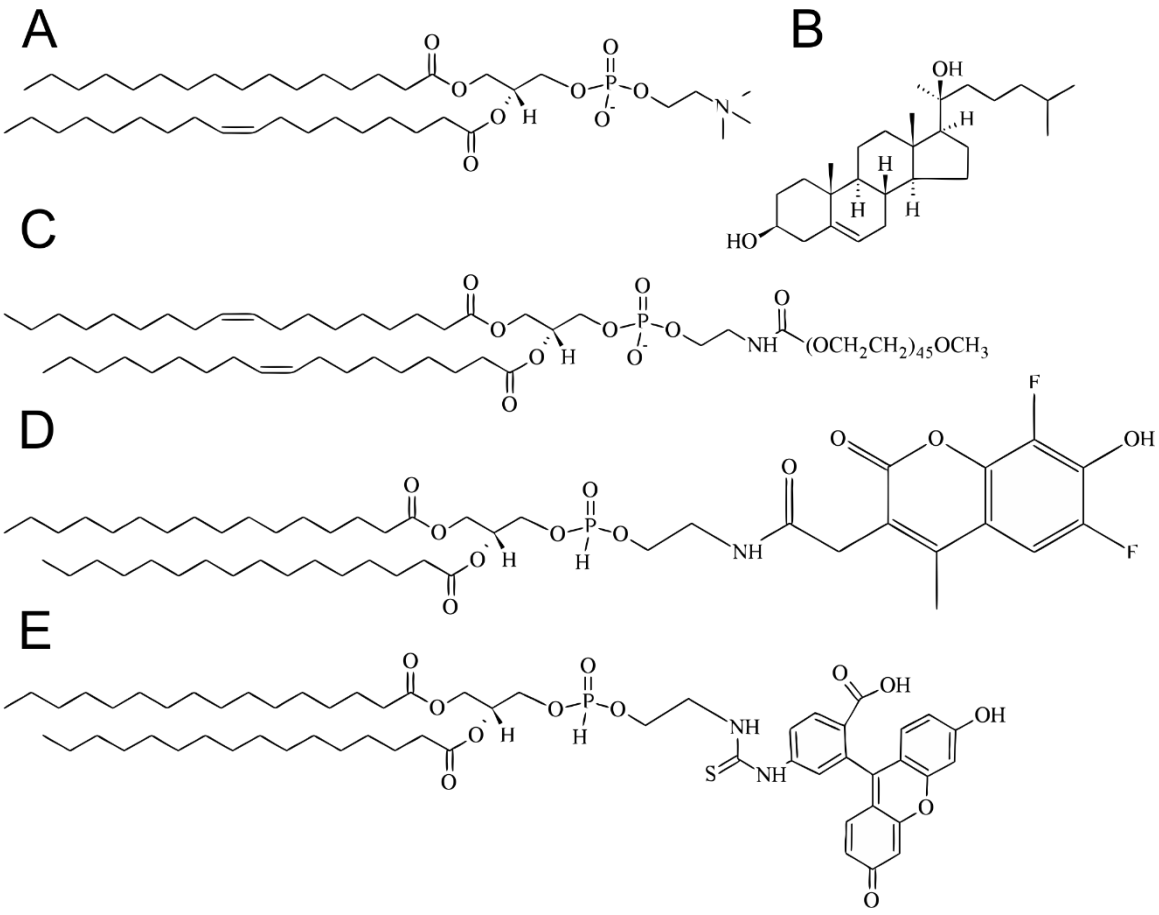

Figure 23. Lipid Structures. A) POPC, B) Cholesterol, C) PEG-DOPE, D) MB-DHPE, E) FL-DHPE

Confocal Microscopy

A point-scanning confocal microscope (Olympus Fluoview FV1000) was used for cellular experiments. For two-color imaging, the red and green fluorescence were taken sequentially to reduce bleedthrough with a 100× oil objective such that one pixel was equal to 99 nm. The red channel was excited with a 559 nm laser with an emission window of 575−675 nm. The green channel was excited with the 488 nm laser with an emission window of 500−545 nm.

Another point-scanning confocal microscope (Olympus Fluoview FV3000) was used for the supported lipid bilayer experiments. For two-color imaging, the red and

green fluorescence or red and blue fluorescence were taken sequentially to reduce bleedthrough with a 100× oil objective such that one pixel was equal to 99 nm (zoom 2.5). The red channel was excited with a 559 nm laser with an emission window of 575−675 nm. The green channel was excited with the 488 nm laser with an emission window of 500−545 nm. The blue channel was excited with a 405 nm laser and emission was detected from 425 to 475 nm.

Data Analysis

Confocal images were split by channel and exported into TIFF files using ImageJ (http://imagej.nih.gov/ij/) or Olympus FV FV31S-SW software. Detailed steps for colocalization analysis in MATLAB are outlined in Appendix D. Colocalization analysis of non-cell nanoparticles resulted in false positive curvature sensing, so the second method outlined in Appendix D was used for cell data. Fluorescence recovery after photobleaching (FRAP) analysis employed the method outlined in Appendix B.

4.3 Results

Using a combination of already established methods, a reuseable nanoparticle patterned substrate was made (8, 9, 129, 130). In order to induce curvature into cells for studying proteins that go to sites of curvature, it was first necessary to have an assay that allowed cells to grow on top of a patterned surface. Initial attempts to grow cells on top of melted nanoparticles resulted in cellular uptake of the fluorescent nanoparticles (Figure 24A). By sputter coating the melted nanoparticles with 30 nm of silicon dioxide (Figure 22), the cells are now capable of growing on top of the patterned substrate Figure 24B, C).

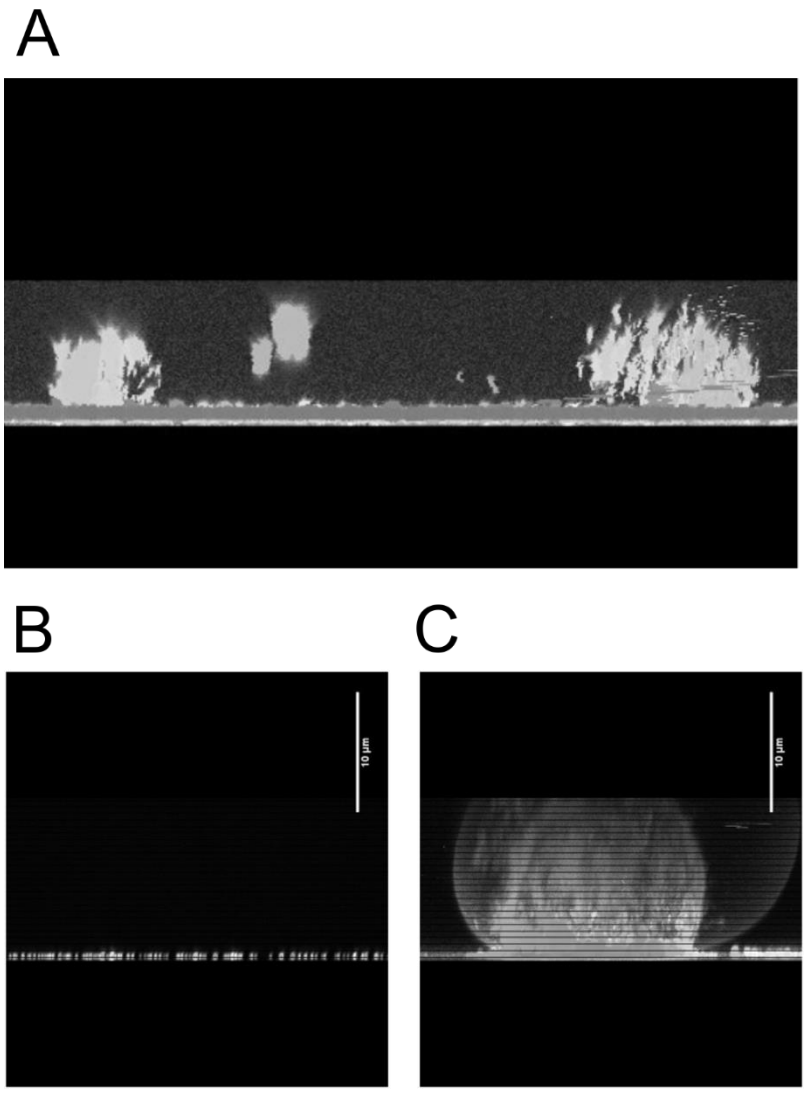

Figure 24. Cells invaginate melted nanoparticles prior to sputter coating. A) PC12 cells grown on top of melted nanoparticles show fluorescence in the z-stack of the nanoparticle channel. B) PC12 cells grown on top of melted and silicon dioxide sputter coated nanoparticles have a distinct layer of fluorescence along the coverslip of the nanoparticle channel. C) The corresponding z-stack for the Cellmask channel highlighting the cell membrane.

AFM was used to determine the size and shape of the melted and sputter coated nanoparticle pattern substrate. The titanium sputter coat was added to enhance the ability of the AFM probe to sense the surface in tapping mode (Figure 25). Data contains a large amount of noise. Line scans indicate widths of 300-400 nm and heights of 80-300 nm. A Confocal AFM instrument was used to measure sizes of melted nanoparticles with no

sputter coating resulting in heights of 70-80 nm for the melted 100 nm nanoparticles (Figure 26). This same instrument was used to measure the roughness of flat region after 30 nm silicon dioxide and 5 nm titanium coatings. The majority of the roughness values are within ±10 nm (Figure 27).

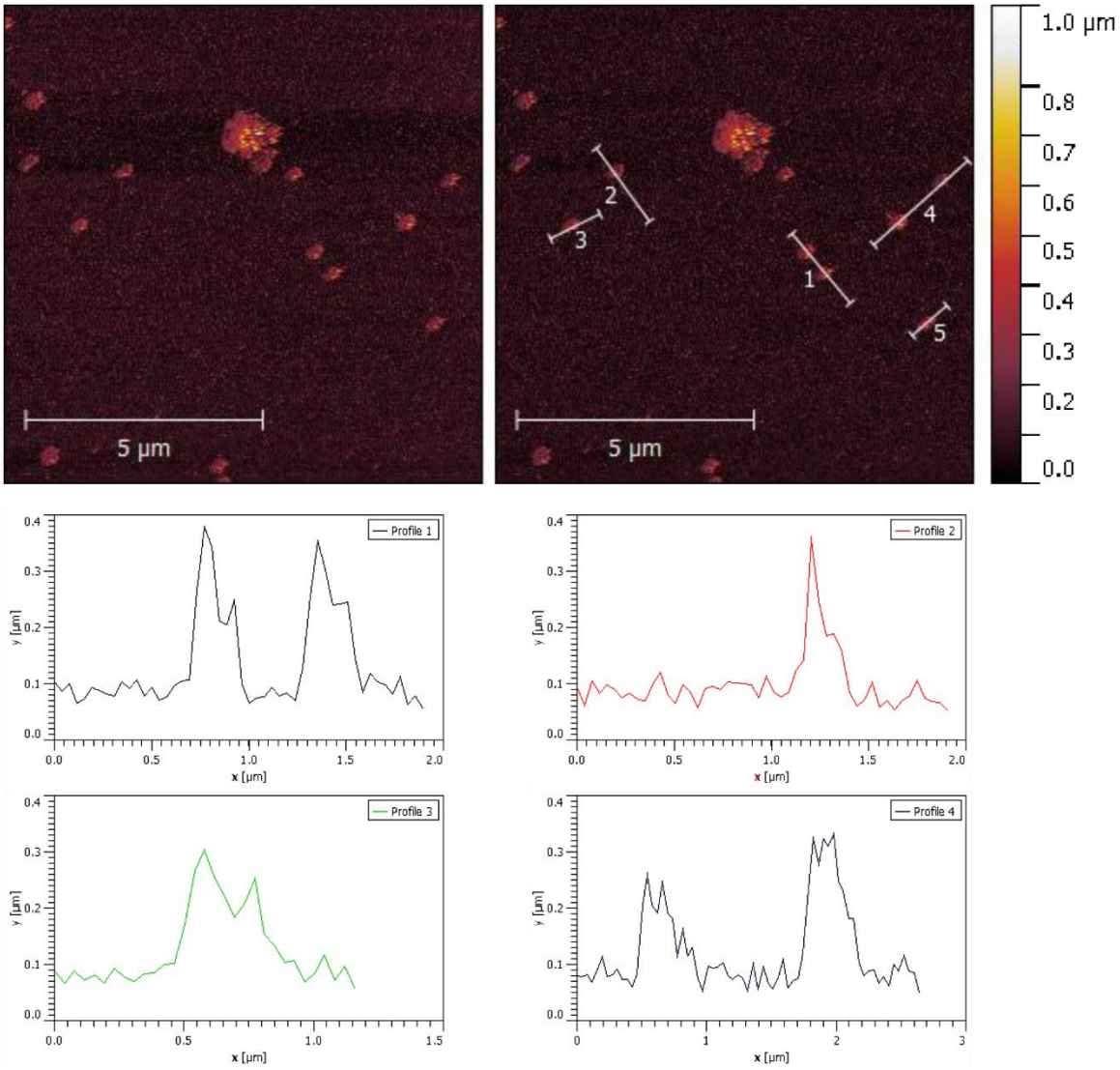

Figure 25. Atomic force microscopy (AFM) of melted and sputter coated nanoparticles. 100 nm nanoparticles were melted and then sputter coated with 30 nm of silicon dioxide and 5 nm of titanium.

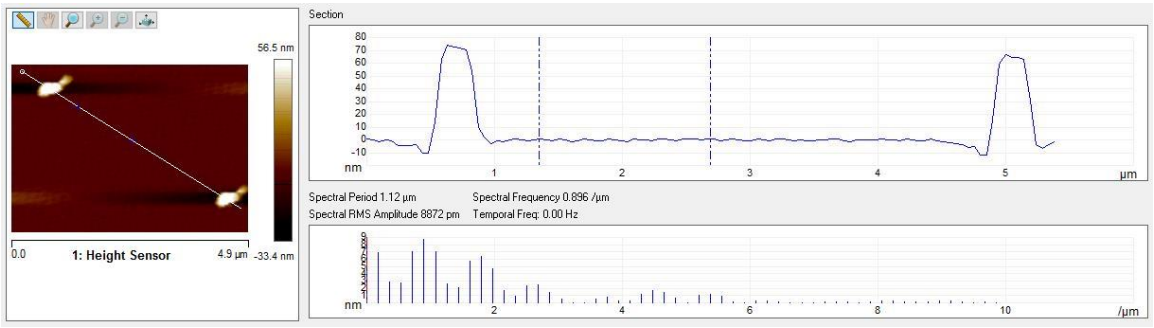

Figure 26. AFM results for melted nanoparticles. Nanoparticles start out as 100 nm Fluospheres and have a height near 70 nm after melting.

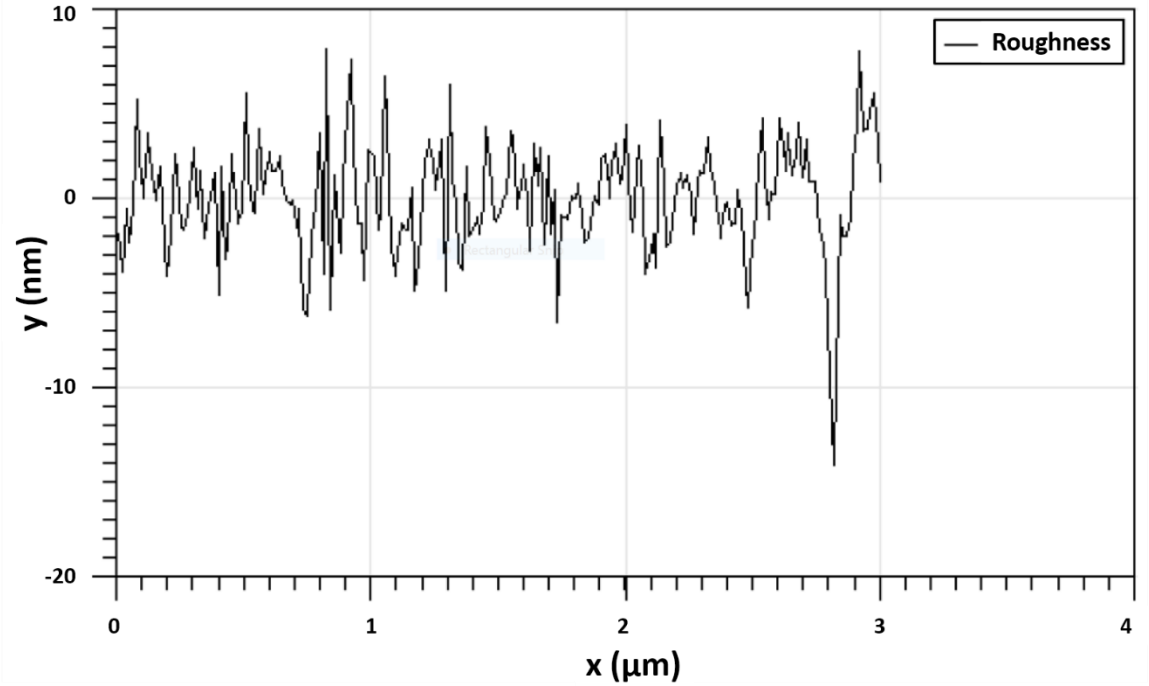

Figure 27. Calculated roughness of 30 nm silicon dioxide and 5 nm titanium coated glass coverslip flat region from an AFM image.

Initial results from colocalization analysis with cellmask membrane staining appeared to show colocalization of membrane material with sites of curvature. This is expected due to the increase of surface area if the membrane wraps around the curved region (data not shown). After analyzing a control, it was discovered that this was a false positive due to the bright regions around the edges of the cell image. By only analyzing

the nanoparticles on the inside of the cells, the reprocessed data shows a lack of curvature sensing by the cell membrane (Figure 28, Appendix D).

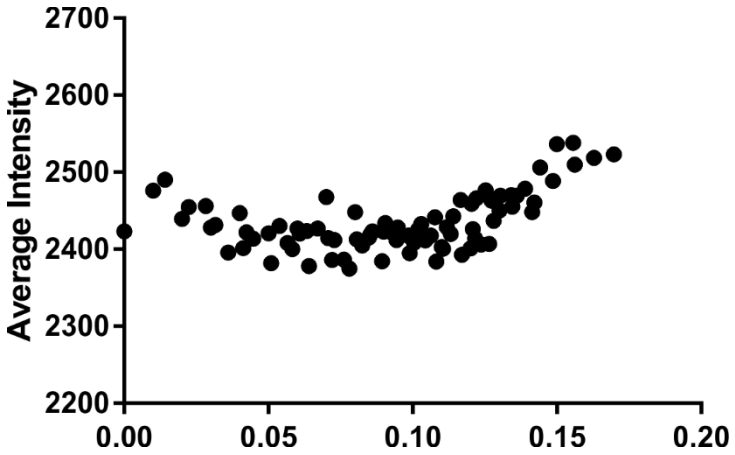

Figure 28. Representative radial average of colocalization analysis of PC12 cell membranes labeled with cell mask on top of sputter coated, melted nanoparticles.

For an *in vitro* analysis of the ability for membranes to curve around the nanoparticle patterned substrate, supported lipid bilayers were used with combinations that contained cholesterol and a polyethylene glycol (PEG) polymer attached to the lipid head group (Figure 23). PEG was added to mimic the extracellular matrix, which has an impact on membrane dynamics (131). Cholesterol was added to mimic cellular membranes. Cellular membrane composition varies by cell type, leaflet side, and even regions of the cell (Figure 29 and Figure 30). One example of this variation has been recorded by others with two opposite sides of an intestinal cell (apical and basolateral) containing different compositions (132). The phospholipid type as well as the amount of cholesterol varies among cellular organelles as seen in Table 5.

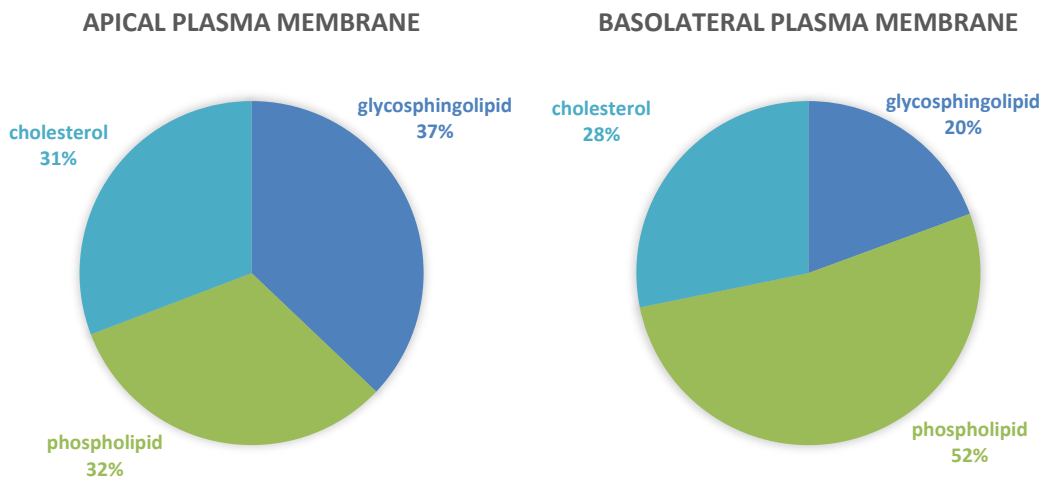

Figure 29. Plasma membrane composition of two regions of intestinal cells are representative of the variation among cell membrane compositions and the high amount of cholesterol present (132).

Table 5. Lipid and cholesterol compositions vary with cellular organelles (133).

	% of total phospholipids				Ratio
Membrane	**PC**	**PE**	**PI**	**PS**	**Chol/PS**
Endoplasmic reticulum	55	30	15	3–5	3
Golgi complex	50	15	10	5	4
Early endosome	47	23	8	8.5	-
Late endosome	48–49	18.5–20	4–7	2.5–3.9	-
Mitochondria	40–46	30–35	5–10	1	10
Plasma membrane	42	25	3	12	8

Fluorescent lipids were used to visualize membranes for colocalization. FL-DHPE has been shown by others to sense curvature and MB-DHPE was used as our control (118). Radially averaged colocalization data was normalized to an average of the tail region (0.75 µm or farther away from the center of the pixel). Results show that the lipid mixture has an impact on the curvature sensing ability of the fluorescent dye (Figure 30).

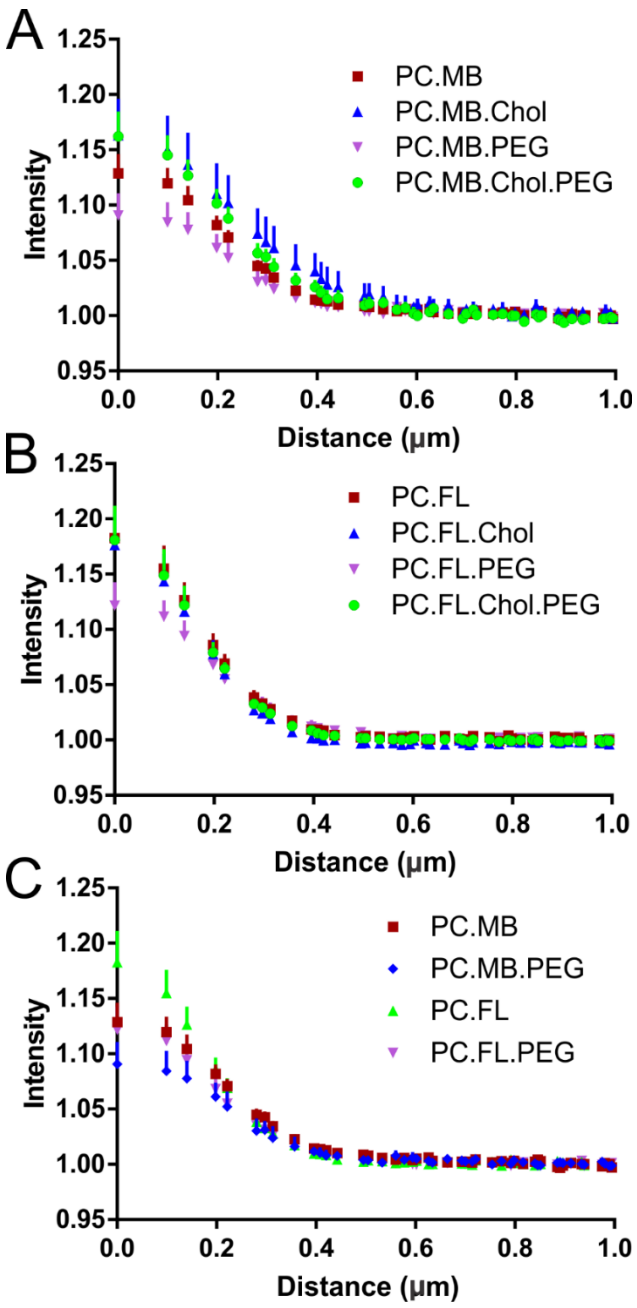

Figure 30. Colocalization analysis of fluorescent lipids in a supported lipid bilayer deposited on melted, silicon dioxide coated nanoparticle patterned surface. X-axis on all graphs shows the distance from the center of the nanoparticle. Y-axis data shows the radially averaged intensity for pixels falling within that distance from the center of the nanoparticle. A) Lipid films made with 93-98% POPC, 2% MB-DHPE, 0 or 5% cholesterol, and 0 or 1% PEG-DOPE. B) Lipid films made with 93-98% POPC, 2% FL-DHPE, 0 or 5% cholesterol, and 0 or 1% PEG-DOPE. C) Comparison of the two fluorescently dye labeled lipids with membranes that contain PEG and those that do not. Each data set is 3 or more experimental days, N=3-5 for SEM. Total number of

particles for each data set are: 1307 for MB, 721 for MB.Chol, 714 for MB.PEG, 1082 for MB.Chol.PEG, 1921 for FL, 889 for FL.Chol, 2251 for FL.PEG, and 4380 for FL.Chol.PEG.

Preliminary results from FRAP data analysis shows that fluid membranes are possible with the silicon dioxide coated nanoparticles. Diffusion constants for each lipid composition were calculated from the FRAP recovery curves (Figure 31 and Figure 32).

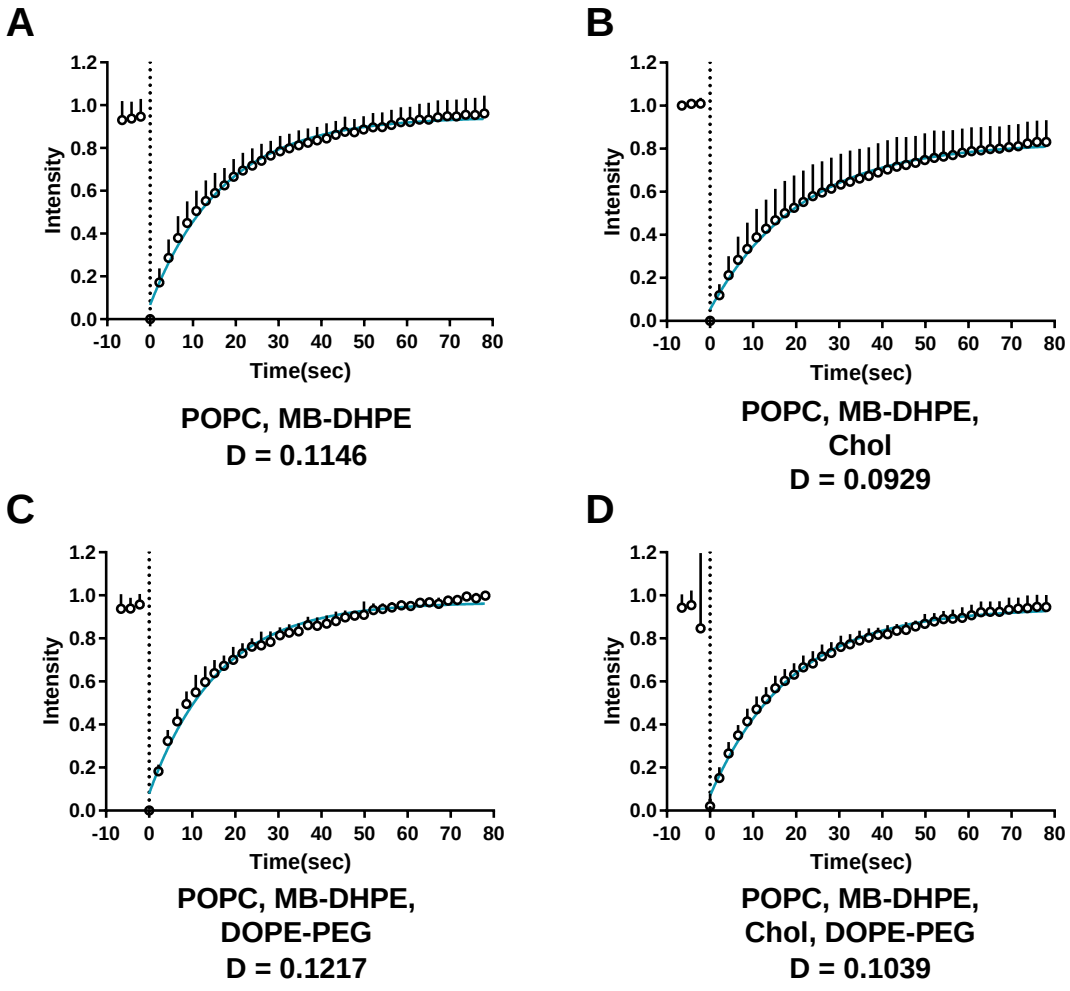

Figure 31. FRAP recovery curves and diffusion constants for lipid membranes containing MB-DHPE deposited on top of 100 nm melted, silicon dioxide coated nanoparticles. Diffusion (represented as D) units are $\mu m^2/s$. Each recovery curve is from 3 experimental days and the following number of images: A) N = 10, B) N = 11, C) N = 7, D) N = 8.

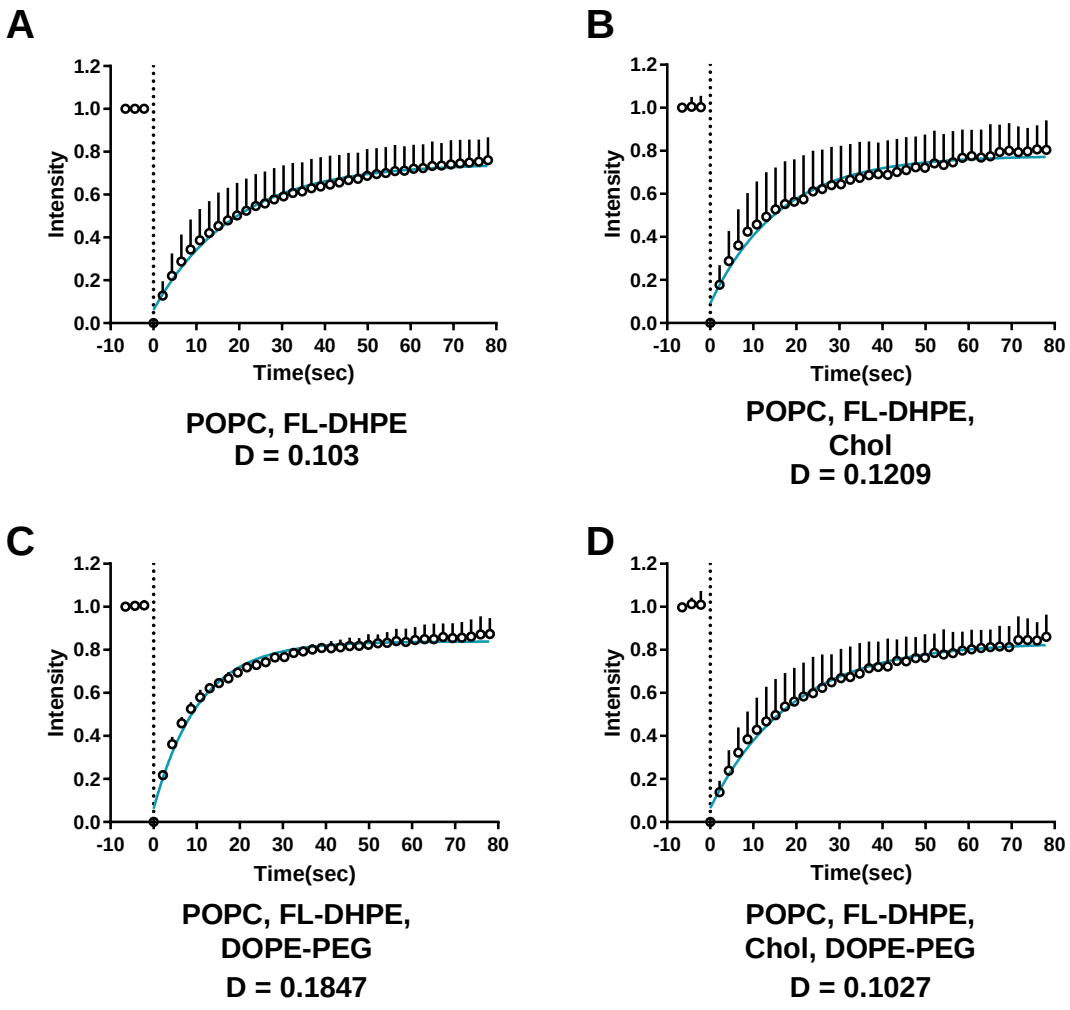

Figure 32. FRAP recovery curves and diffusion constants for lipid membranes containing FL-DHPE deposited on top of 100 nm melted, silicon dioxide coated nanoparticles. Diffusion (D) units are $\mu m^2/s$. Each recovery curve is from 3 experimental days and the following number of images: A) N = 10, B) N = 10, C) N = 6, D) N = 10.

4.4 Discussion

This chapter shows three key advances for our membrane curvature biosensor assay. The first and second key advancements were to create a fixed and reusable nanoparticle substrate through annealing and sputter coating the nanoparticles. The third advancement was the addition of chambers to allow for smaller experimental working volumes.

A fixed substrate was done by sputter coating fluorescent nanoparticles patterned onto a glass coverslip. This process merged two current protocols to melt and coat fluorescent nanoparticles as seen in Figure 22 (8, 129). The permanence of the patterned substrate not only allows for washing and reusing them, but also applications of lipid bilayer and cellular membrane experiments. Due to the slightly larger well area and the more permanent nature of the 3D printed chambers, they are preferable to the smaller silicone rubber chambers (Figure 21). Furthermore, the pink colored silicone rubber caused scattering in the red channel with epifluorescence imaging, making it difficult to focus in the eyepiece. Black colored silicone rubber was then used and did not have scattering. The versatility of being able to 3D print chambered wall system in the size and shape needed for the experiment and having the ability to use plain coverglass or nanopatterned coverglass make this a desirable system.

The AFM data from the University of Denver instrument contained a large amount of noise, however the images do indicate the relative distances between nanoparticles and although clumps do exist, that the majority of nanoparticles are separated (Figure 25). Furthermore, the larger size for the titanium sputter coated nanoparticles indicates that the AFM probe in tapping mode interacts widely with the metal. This was added for the purpose of increasing the AFM interaction, since earlier experiments with AFM on melted nanoparticles had failed to produce any images showing the nanoparticles (not shown here). The opportunity to use the AFM at Colorado State University allowed for a more accurate measurement with a suitable height of 80 nm for a melted nanoparticle (Figure 26).

One use for this assay is to determine the curvature sensing ability of different lipid compositions and probes. FL-DHPE has been shown by others to prefer curvature and was used as our positive control (118). MB-DHPE is not expected to prefer regions of curvature over flat regions. The more a lipid membrane curves around a nanoparticle patterned region, the higher the intensity. Unless a lipid completely avoids curvature, it is expected to have a slight increase in intensity around the nanoparticle due to an increased surface area (established in Chapter Three). As seen in Figure 30, MB-DHPE has a smaller normalized intensity at the center of nanoparticles than FL-DHPE. This matches the expected results of others for FL-DHPE to sense curvature.

The proposed experimental design was to test whether or not the addition of cholesterol or a lipid with a PEG head group would affect that curvature sensing. As seen in Figure 30A, the addition of PEG to a membrane decreases the intensity near the nanoparticle. This is most likely due to the size pushing it away from the surface and having less surface area to interact with the nanoparticle. Figure 30A also shows that the addition of cholesterol to membranes with or without PEG has the same effect – to increase the ability to sense curvature. It can be envisioned that the small size of the cholesterol would help lipid packing around nanoparticles. When comparing the same addition of cholesterol or PEG to membranes with FL-DHPE (Figure 30B), it appears that cholesterol does not affect the curvature sensing of a lipid that already has that ability, however, PEG still decreases the curvature sensing. The decrease in the ability of PEG to sense curvature can be applied as a mimic of the extracellular matrix and therefore cells would be expected to have a certain size of sputter coated nanoparticle

pattern that would no longer induce curvature in the membrane, but instead would grow the same as a flat membrane. This idea is supported by other research where micro-scale and nano-scale patterns affects cell growth differently (134, 135).

4.5 Summary

In this section, we have shown how the addition of a 30 nm silicon dioxide sputter coating to a nanoparticle patterned surface allows for cell growth without invagination of the nanoparticles. This sputter coating still had curved regions, as seen by the sensing of curvature with the colocalization analysis radial average results. The bilayers were also able to be bleached and recover, indicating that a fluid bilayer can form on top of the silicon dioxide coated nanoparticles. Overall, the addition of PEG to a membrane decreased its ability to sense the curvature. The fabrication of chambered systems to attach to the nanopatterned surface added the convenience of multiple experimental conditions to be tested at one time with lower volumes. Lastly, the ease of producing and reusing a 3D print chambered system and its cost-effectiveness will allow it to be applied to a vast array of experimental methods.

CHAPTER FIVE: CONCLUSION AND FUTURE WORK

CRP biochemical research in this work showed significant C1q binding for mCRP made with 0.01% SDS and heated for 1 hour at 80 °C and for mCRP made with 1.5 M GndHCl. 7 M urea treated CRP showed some C1q binding, however, it was not significant compared with BSA binding. Structural analysis with Chimera software complimented the use of circular dichroism as well as intrinsic tryptophan and ANS fluorescence to analyze the various denaturants used. The transition from pCRP to mCRP was clearly seen on non-denaturing PAGE and with intrinsic fluorescence. Furthermore, the denaturation curve for GndHCl was used to calculate the Gibbs free energy of unfolding for CRP.

The outer leaflet of apoptotic cell membranes was mimicked using a nanopatterned substrate to create curved, supported lipid bilayers and then used to characterize how CRP conformation affects the interactions between CRP and target membranes. In this assay, the chemical composition and shape are separately tunable parameters. The lipids consisted primarily of palmitoyl-oleoylphosphatidylcholine, with and without lysophosphatidylcholine, and the curvature had a radius of 27−55 nm. Using this model system combined with quantitative fluorescence microscopy methods, CRP binding to lipid membranes was measured as a function of different conformations of CRP. The modified form of CRP bound curved membranes, but the pentameric form did not for the range of curvatures measured. Unlike most other curvature-sensing proteins,

modified CRP accumulated more at a moderate curvature, rather than highly curved or flat regions, suggesting that the membrane bound form does not solely depend on a defect binding mechanism. The presence of lysophosphatidylcholine, a component of apoptotic membranes, increased CRP binding to all types of membranes. Overall, our results show that CRP interactions vary with protein form, lipid composition, and membrane shape. The mechanism by which CRP recognizes damaged membranes depends on the combination of all three.

The final section of this work illustrates the advantages of a sputter coated nanopatterned substrate for both repeated use and for the versatility in applications from supported lipid bilayers to cells. Experimental options were added and imaging was facilitated by the addition of chambers (either cut silicone rubber or 3D printed PETG plastic). These chambered nanopatterned systems are reusable and reduce the experimental volume. Error bars from supported lipid bilayer experiments show consistency between days for reusing these systems. Results from colocalization analysis to check for curvature sensing indicates that the addition of cholesterol to membranes increases its ability to sense curvature and the addition of a lipid with a PEG attached to the head group decreases the ability for a lipid mixture to sense curvature.

Future research to further understand and characterize this system includes the analysis of both cellular and supported lipid bilayer membranes with different sizes of nanoparticles and creating an eight well 3D printable chamber for attachment to a 24 x 50 mm 1.5 coverglass plate. Initial testing of this coverglass size worked well with confocal imaging. Finally, along with publication, the files for the 3D printable chambers will be

made available on the NIH 3D print exchange website. Further analysis of FRAP of membranes with the new system is needed to confirm differences in fluidity.

REFERENCES

1. Edidin, M. (2003) Lipids on the frontier: a century of cell-membrane bilayers. *Nat. Rev. Mol. Cell Biol.* **4**, 414–418

2. Sessa, G., and Weissmann, G. (1968) Phospholipid spherules (liposomes) as a model for biological membranes. *J. Lipid Res.* **9**, 310–318

3. Finean, J. B., Coleman, R., and Green, W. A. (1966) Studies of isolated plasma membrane preparations. *Ann. N. Y. Acad. Sci.* **137**, **Biolo**, 414–420

4. Wu, M., and Camilli, P. D. (2012) Supported Native Plasma Membranes as Platforms for the Reconstitution and Visualization of Endocytic Membrane Budding. in *Methods in Cell Biology: Lipids*, pp. 3–18, Academic Press, Amsterdam

5. Richter, R., Mukhopadhyay, A., and Brisson, A. (2003) Pathways of Lipid Vesicle Deposition on Solid Surfaces: A Combined QCM-D and AFM Study. *Biophys. J.* **85**, 3035–3047

6. Bergers, J. J., Vingerhoeds, M. H., Bloois, L. V., Herron, J. N., Janssen, L. H. M., Fischer, M. J. E., and Crommelint, D. J. A. (1993) The Role of Protein Charge in Protein-Lipid Interactions. pH-Dependent Changes of the Electrophoretic Mobility of Liposomes through Adsorption of Water-Soluble, Globular Proteins. *Biochemistry*. **32**, 4641–4649

7. Sasaki, D. Y., Lopez, G. P., Brueck, S. R. J., Zeindeldin, R. R., Last, J. A., Slade, A. L., Bisong, P., O'Brien, M. J., and Ista, L. K. (2004) *Lipid Membranes on Nanostructured Silicon*, Albuquerque

8. Black, J. C., Cheney, P. P., Campbell, T., and Knowles, M. K. (2014) Membrane curvature based lipid sorting using a nanoparticle patterned substrate. *Soft Matter*. **10**, 2016–23

9. Sundh, M., Svedhem, S., and Sutherland, D. S. (2011) Formation of supported lipid bilayers at surfaces with controlled curvatures: Influence of lipid charge. *J. Phys. Chem. B.* **115**, 7838–7848

10. Marsh, D. (1990) Lipid-protein interactions in membranes. *FEBS Lett.* **268**, 371–375

11. Kleinschmidt, J. H. (ed.) (2013) *Lipid-Protein Interactions: Methods and Protocols (Methods in Molecular Biology) Vol. 974*, Humana Press

12. Zhu, C., Das, S. L., and Baumgart, T. (2012) Nonlinear Sorting, Curvature Generation, and Crowding of Endophilin N-BAR on Tubular Membranes.

Biophys. J. **102**, 1837–1845

13. Edidin, M. (2003) The State of Lipid Rafts: from Model Membranes to Cells. *Annu. Rev. Biophys. Biomol. Struct.* **32**, 257–283

14. Cooke, I. R., and Deserno, M. (2006) Coupling between Lipid Shape and Membrane Curvature. *Biophys. J.* **91**, 487–495

15. Tian, A., and Baumgart, T. (2009) Sorting of Lipids and Proteins in Membrane Curvature Gradients. *Biophys. J.* **96**, 2676–2688

16. Bhatia, V. K., Madsen, K. L., Bolinger, P.-Y., Kunding, A., Hedegård, P., Gether, U., and Stamou, D. (2009) Amphipathic motifs in BAR domains are essential for membrane curvature sensing. *EMBO J.* **28**, 3303–3314

17. Wang, M. S., and Reed, S. M. (2011) Electrophoretic mobility of lipoprotein nanoparticle mimics. *Proc. IEEE Conf. Nanotechnol.*

18. Chou, C., Hsu, H.-Y., Wu, H.-T., Tseng, K.-Y., Chiou, A., Yu, C.-J., Lee, Z.-Y., and Chan, T.-S. (2007) Fiber optic biosensor for the detection of C-reactive protein and the study of protein binding kinetics. *J. Biomed. Opt.* **12**, 241–249

19. Black, S., Kushner, I., and Samols, D. (2004) C-reactive Protein. *J. Biol. Chem.* **279**, 48487–90

20. Kindt, T. J., Goldsby, R. A., and Osborne, B. A. (2007) *Kuby Immunology*, 6th Ed., W.H. Freeman and Company, New York

21. Gershov, D., Kim, S., Brot, N., and Elkon, K. B. (2000) C-Reactive protein binds to apoptotic cells, protects the cells from assembly of the terminal complement components, and sustains an antiinflammatory innate immune response: implications for systemic autoimmunity. *J. Exp. Med.* **192**, 1353–64

22. Volanakis, J. E. (2001) Human C-reactive protein: expression, structure, and function. *Mol. Immunol.* **38**, 189–197

23. Eisenhardt, S. U., Habersberger, J., Murphy, A., Chen, Y. C., Woollard, K. J., Bassler, N., Qian, H., von zur Muhlen, C., Hagemeyer, C. E., Ahrens, I., Chin-Dusting, J., Bobik, A., and Peter, K. (2009) Dissociation of pentameric to monomeric C-reactive protein on activated platelets localizes inflammation to atherosclerotic plaques. *Circ. Res.* **105**, 128–137

24. Eisenhardt, S. U., Thiele, J. R., Bannasch, H., Stark, G. B., and Peter, K. (2009) C-reactive protein: how conformational changes influence inflammatory properties. *Cell Cycle*. **8**, 3885–3892

25. de Ferranti, S. D., and Rifai, N. (2007) C-reactive protein: a nontraditional serum marker of cardiovascular risk. *Cardiovasc. Pathol.* **16**, 14–21

26. Katrinchak, C., and Fritz, K. (2007) Clinical implications of C-reactive protein as a predictor of vascular risk. *J. Am. Acad. Nurse Pract.* **19**, 335–40

27. Libby, P. (2012) Inflammation in atherosclerosis. *Arterioscler. Thromb. Vasc. Biol.* **32**, 2045–51

28. Devaraj, S., Singh, U., and Jialal, I. (2009) The evolving role of C-reactive protein in atherothrombosis. *Clin. Chem.* **55**, 229–38

29. Verma, S., Szmitko, P. E., and Yeh, E. T. H. (2004) C-Reactive Protein: Structure Affects Function. *Circulation*. **109**, 1914–1917

30. Eisenhardt, S. U., Habersberger, J., and Peter, K. (2009) Monomeric C-reactive protein generation on activated platelets: the missing link between inflammation and atherothrombotic risk. *Trends Cardiovasc. Med.* **19**, 232–237

31. Zwaka, T. P., Hombach, V., and Torzewski, J. (2001) C-Reactive Protein–Mediated Low Density Lipoprotein Uptake by Macrophages: Implications for Atherosclerosis. *Circulation*. **103**, 1194–1197

32. Mihlan, M., Blom, A. M., Kupreishvili, K., Lauer, N., Stelzner, K., Bergstrom, F., Niessen, H. W. M., and Zipfel, P. F. (2011) Monomeric C-reactive protein modulates classic complement activation on necrotic cells. *FASEB J.* **25**, 4198–4210

33. Elliott, M. R., and Ravichandran, K. S. (2010) Clearance of apoptotic cells: implications in health and disease. *J. Cell Biol.* **189**, 1059–70

34. Shiratsuchi, A., Mori, T., and Nakanishi, Y. (2002) Independence of Plasma Membrane Blebbing from Other Biochemical and Biological Characteristics of Apoptotic Cells. *J. Biochem.* **132**, 381–386

35. Bochkov, V. N., Oskolkova, O. V, Birukov, K. G., Levonen, A.-L., Binder, C. J., and Stöckl, J. (2010) Generation and biological activities of oxidized phospholipids. *Antioxid. Redox Signal.* **12**, 1009–59

36. Ji, S.-R., Wu, Y., Zhu, L., Potempa, L. A., Sheng, F.-L., Lu, W., and Zhao, J. (2007) Cell membranes and liposomes dissociate C-reactive protein (CRP) to form a new, biologically active structural intermediate: mCRP(m). *FASEB J.* **21**, 284–294

37. Thiele, J. R., Habersberger, J., Braig, D., Schmidt, Y., Goerendt, K., Maurer, V., Bannasch, H., Scheichl, A., Woollard, K., von Dobschutz, E., Kolodgie, F.,

Virmani, R., Stark, G. B., Peter, K., and Eisenhardt, S. U. (2014) The dissociation of pentameric to monomeric C-reactive protein localizes and aggravates inflammation: in vivo proof of a powerful pro-inflammatory mechanism and a new anti-inflammatory strategy. *Circulation*. **130**, 35–50

38. Wang, M. S., Messersmith, R. E., and Reed, S. M. (2012) Membrane curvature recognition by C-reactive protein using lipoprotein mimics. *Soft Matter*. **8**, 7909–7918

39. Steinbrecher, U. P., Zhang, H., and Lougheed, M. (1990) Role of Oxidatively Modified LDL in Atherosclerosis. *Free Radic. Biol. Med.* **9**, 155–168

40. Wang, M. S., Black, J. C., Knowles, M. K., and Reed, S. M. (2011) C-reactive protein (CRP) aptamer binds to monomeric but not pentameric form of CRP. *Anal. Bioanal. Chem.* **401**, 1309–1318

41. Casas, J. P., Shah, T., Hingorani, a D., Danesh, J., and Pepys, M. B. (2008) C-reactive protein and coronary heart disease: a critical review. *J. Intern. Med.* **264**, 295–314

42. Slevin, M., Matou, S., Zeinolabediny, Y., Corpas, R., Weston, R., Liu, D., Boras, E., Di Napoli, M., Petcu, E., Sarroca, S., Popa-Wagner, A., Love, S., Font, M. A., Potempa, L. A., Al-Baradie, R., Sanfeliu, C., Revilla, S., Badimon, L., and Krupinski, J. (2015) Monomeric C-reactive protein--a key molecule driving development of Alzheimer's disease associated with brain ischaemia? *Sci. Rep.* **5**, 13281

43. Edberg, J. C., Wu, J., Langefeld, C. D., Brown, E. E., Marion, M. C., Mcgwin, G., Petri, M., Ramsey-Goldman, R., Reveille, J. D., Frank, S. G., Kaufman, K. M., Harley, J. B., Alarcón, G. S., and Kimberly, R. P. (2008) Genetic variation in the CRP promoter: Association with systemic lupus erythematosus. *Hum. Mol. Genet.* **17**, 1147–1155

44. Du Clos, T. W. (2013) Pentraxins : structure, function, and role in inflammation. *ISRN Inflamm.*

45. Jones, N. R., Pegues, M. A., McCrory, M. A., Kerr, S. W., Jiang, H., Sellati, R., Berger, V., Villalona, J., Parikh, R., McFarland, M., Pantages, L., Madwed, J. B., and Szalai, A. J. (2011) Collagen-induced arthritis is exacerbated in C-reactive protein-deficient mice. *Arthritis Rheum.* **63**, 2641–2650

46. Szalai, A. J., Nataf, S., Hu, X.-Z., and Barnum, S. R. (2002) Experimental allergic encephalomyelitis is inhibited in transgenic mice expressing human C-reactive protein. *J. Immunol.* **168**, 5792–5797

47. Pettersen, E. F., Goddard, T. D., Huang, C. C., Couch, G. S., Greenblatt, D. M.,

Meng, E. C., and Ferrin, T. E. (2004) UCSF Chimera - A visualization system for exploratory research and analysis. *J. Comput. Chem.* **25**, 1605–1612

48. Thompson, D., Pepys, M. B., and Wood, S. P. (1999) The physiological structure of human C-reactive protein and its complex with phosphocholine. *Structure*. **7**, 169–177

49. Li, Q., Kang, T., Tian, X., Ma, Y., Li, M., Richards, J., Bythwood, T., Wang, Y., Li, X., Liu, D., Ma, L., and Song, Q. (2013) Multimeric stability of human C-reactive protein in archived specimens. *PLoS One*. **8**, 1–6

50. Ji, S. R., Wu, Y., Potempa, L. A., Liang, Y. H., and Zhao, J. (2006) Effect of modified C-reactive protein on complement activation: A possible complement regulatory role of modified or monomeric C-reactive protein in atherosclerotic lesions. *Arterioscler. Thromb. Vasc. Biol.* **26**, 934–941

51. Gaboriaud, C., Frachet, P., Thielens, N. M., and Arlaud, G. J. (2012) The human C1q globular domain: Structure and recognition of non-immune self ligands. *Front. Immunol.* **2**, 1–8

52. McGrath, F. D. G., Brouwer, M. C., Arlaud, G. J., Daha, M. R., Hack, C. E., and Roos, A. (2006) Evidence that complement protein C1q interacts with C-reactive protein through its globular head region. *J. Immunol.* **176**, 2950–2957

53. Agrawal, A., Shrive, A. K., Greenhough, T. J., and Volanakis, J. E. (2001) Topology and structure of the C1q-binding site on C-reactive protein. *J. Immunol.* **166**, 3998–4004

54. Gaboriaud, C., Thielens, N. M., Gregory, L. A., Rossi, V., Fontecilla-Camps, J. C., and Arlaud, G. J. (2004) Structure and activation of the C1 complex of complement: Unraveling the puzzle. *Trends Immunol.* **25**, 368–373

55. Bíró, A., Rovó, Z., Papp, D., Cervenak, L., Varga, L., Füst, G., Thielens, N. M., Arlaud, G. J., and Prohászka, Z. (2007) Studies on the interactions between C-reactive protein and complement proteins. *Immunology*. **121**, 40–50

56. Li, H. Y., Wang, J., Meng, F., Jia, Z. K., Su, Y., Bai, Q. F., Lv, L. L., Ma, F. R., Potempa, L. A., Yan, Y. Bin, Ji, S. R., and Wu, Y. (2016) An intrinsically disordered motif mediates diverse actions of monomeric C-reactive protein. *J. Biol. Chem.* **291**, 8795–8804

57. Li, H. Y., Wang, J., Wu, Y. X., Zhang, L., Liu, Z. P., Filep, J. G., Potempa, L. A., Wu, Y., and Ji, S. R. (2014) Topological localization of monomeric C-reactive protein determines proinflammatory endothelial cell responses. *J. Biol. Chem.* **289**, 14283–14290

58. Fujita, M., Takada, Y. K., Izumiya, Y., and Takada, Y. (2014) The binding of monomeric C-reactive protein (mCRP) to integrins αvβ3 and α4β1 is related to its pro-inflammatory action. *PLoS One*

59. Taylor, K. E., and Van Den Berg, C. W. (2007) Structural and functional comparison of native pentameric, denatured monomeric and biotinylated C-reactive protein. *Immunology*. **120**, 404–11

60. Asztalos, B. F., Horan, M. S., Horvath, K. V., McDermott, A. Y., Chalasani, N. P., and Schaefer, E. J. (2014) Obesity associated molecular forms of C-reactive protein in human. *PLoS One*. **9**, e109238

61. Eisenhardt, S. U., Habersberger, J., Murphy, A., Chen, Y.-C., Woollard, K. J., Bassler, N., Qian, H., von Zur Muhlen, C., Hagemeyer, C. E., Ahrens, I., Chin-Dusting, J., Bobik, A., and Peter, K. (2009) Dissociation of pentameric to monomeric C-reactive protein on activated platelets localizes inflammation to atherosclerotic plaques. *Circ. Res.* **105**, 128–37

62. Hammond, D. J., Singh, S. K., Thompson, J. A., Beeler, B. W., Rusiñol, A. E., Pangburn, M. K., Potempa, L. A., and Agrawal, A. (2010) Identification of acidic pH-dependent ligands of pentameric C-reactive protein. *J. Biol. Chem.* **285**, 36235–36244

63. Alnaas, A. A., Moon, C. L., Alton, M., Reed, S. M., and Knowles, M. K. (2017) Conformational changes in C-reactive protein affect binding to curved membranes in a lipid bilayer model of the apoptotic cell surface. *J. Phys. Chem. B.* **121**, 2631–2639

64. Li, H.-Y., Wang, J., Meng, F., Jia, Z.-K., Su, Y., Bai, Q.-F., Lv, L.-L., Ma, F.-R., Potempa, L. A., Yan, Y.-B., Ji, S.-R., and Wu, Y. (2016) An intrinsically disordered motif mediates diverse actions of monomeric C-reactive protein. *J. Biol. Chem.* **291**, 8795–8804

65. Khreiss, T., József, L., Hossain, S., Chan, J. S. D., Potempa, L. A., and Filep, J. G. (2002) Loss of pentameric symmetry of C-reactive protein is associated with delayed apoptosis of human neutrophils. *J. Biol. Chem.* **277**, 40775–40781

66. Okemefuna, A. I., Stach, L., Rana, S., Buetas, A. J. Z., Gor, J., and Perkins, S. J. (2010) C-reactive protein exists in an NaCl concentration-dependent pentamer-decamer equilibrium in physiological buffer. *J. Biol. Chem.* **285**, 1041–52

67. Potempa, L. A., Maldonado, B. A., Laurent, P., Zemel, E. S., and Gewurz, H. (1983) Antigenic, electrophoretic and binding alterations of human C-reactive protein modified selectively in the absence of calcium. *Mol. Immunol.* **20**, 1165–1175

68. Laemmli, U. K. (1970) Cleavage of structural proteins during the assembly of the head of bacteriophage T4. *Nature*. **227**, 680–685

69. Santoro, M. M., and Bolen, D. W. (1988) Unfolding free energy changes determined by the linear extrapolation method. 1. Unfolding of phenylmethanesulfonyl alpha-chymotrypsin using different denaturants. *Biochemistry*. **27**, 8063–8068

70. Albani, J. R. (2007) *Principles and Applications of Fluorescence Spectroscopy*, Blackwell Science, Oxford

71. Singh, S. K., Thirumalai, A., Hammond, D. J., Pangburn, M. K., Mishra, V. K., Johnson, D. a., Rusiñol, A. E., and Agrawal, A. (2012) Exposing a hidden functional site of C-reactive protein by site-directed mutagenesis. *J. Biol. Chem.* **287**, 3550–3558

72. Smilgies, D. M., and Folta-Stogniew, E. (2015) Molecular weight-gyration radius relation of globular proteins: A comparison of light scattering, small-angle X-ray scattering and structure-based data. *J. Appl. Crystallogr.* **48**, 1604–1606

73. Vashist, S. K., Venkatesh, A. G., Marion Schneider, E., Beaudoin, C., Luppa, P. B., and Luong, J. H. T. (2016) Bioanalytical advances in assays for C-reactive protein. *Biotechnol. Adv.* **34**, 272–290

74. Dutta, A., Tirupula, K. C., Alexiev, U., and Klein-seetharaman, J. (2010) Characterization of membrane protein non-native states. 1. Extent of unfolding and aggregation of rhodopsin in the presence of chemical denaturants. *Biochemistry*. **49**, 6317–6328

75. Kauzmann, W. (1959) *Advances in Protein Chemistry Volume 14*, Advances in Protein Chemistry, Elsevier, 10.1016/S0065-3233(08)60608-7

76. Dutta, A., Kim, T.-Y., Moeller, M., Wu, J., Alexiev, U., and Klein-Seetharaman, J. (2010) Characterization of membrane protein non-native states. 2. The SDS-unfolded states of rhodopsin. *Biochemistry*. **49**, 6329–40

77. Denaturation (2013) *Columbia Encycl.*

78. Tanford, C. (1968) *Advances in Protein Chemistry Volume 23*, Advances in Protein Chemistry, Elsevier, 10.1016/S0065-3233(08)60401-5

79. Park, C., and Marqusee, S. (2004) Analysis of the stability of multimeric proteins by effective DeltaG and effective m-values. *Protein Sci.* **13**, 2553–2558

80. Collins, K. D. (1997) Charge density-dependent strength of hydration and biological structure. *Biophys. J.* **72**, 65–76

81. Hatefi, Y., and Hanstein, W. G. (1969) Solubilization of particulate proteins and nonelectrolytes by chaotropic agents. *Proc. Natl. Acad. Sci. U. S. A.* **62**, 1129–36

82. Povarova, O. I., Kuznetsova, I. M., and Turoverov, K. K. (2010) Differences in the pathways of proteins unfolding induced by urea and guanidine hydrochloride: Molten globule state and aggregates. *PLoS One*. **5**, 1–4

83. Oliveira, E. B., Gotschlich, E. C., and Liu, T. Y. (1979) Primary structure of human C-reactive protein. *J. Bol. Chem.* **254**, 489–502

84. Kresl, J. J., Potempa, L. A., and Anderson, B. E. (1998) Conversion of native oligomeric to a modified monomeric form of human C-reactive protein. *Int. J. Biochem. Cell Biol.* **30**, 1415–1426

85. Rzychon, M., Zegers, I., and Schimmel, H. (2010) Analysis of the physicochemical state of C-reactive protein in different preparations including 2 certified reference materials. *Clin. Chem.* **56**, 1475–82

86. Kelly, S. M., Jess, T. J., and Price, N. C. (2005) How to study proteins by circular dichroism. *Biochim. Biophys. Acta - Proteins Proteomics*. **1751**, 119–139

87. Shirley, B. A. (1974) Urea and guanidine hydrochloride denaturation curves. in *Methods in Molecular Biology: Protein Stability and Folding*, pp. 177–190, **40**, 177–190

88. Singh, R., Hassan, I., Islam, A., and Ahmad, F. (2015) Cooperative unfolding of residual structure in heat denatured proteins by urea and guanidinium chloride. *PLoS One*. **10**, 1–16

89. Lakowicz, J. R. (2006) Protein Fluorescence. in *Principles of Fluorescence Spectroscopy*, 3rd Ed., pp. 529–575, Springer, Baltimore

90. Kim, S. D., Ryu, J. S., Yi, H. K., Kim, S. C., and Zhang, B. T. (2004) Construction of C-reactive protein-binding aptamer as a module of the DNA computing system for diagnosing cardiovascular diseases. in *Preliminary proceedings of the tenth international meeting on DNA computing (DNA10)*, pp. 334–343

91. Edelman, G. M., and Gotschlich, E. C. (1965) C-reactive protein: a molecule composed of subunits. *Proc. Natl. Acad. Sci. U. S. A.* **54**, 558–566

92. Ji, S.-R., Ma, L., Bai, C.-J., Shi, J.-M., Li, H.-Y., Potempa, L. A., Filep, J. G., Zhao, J., and Wu, Y. (2009) Monomeric C-reactive protein activates endothelial cells via interaction with lipid raft microdomains. *FASEB J.* **23**, 1806–16

93. Schwedler, S. B., Amann, K., Wernicke, K., Krebs, A., Nauck, M., Wanner, C., Potempa, L. A., and Galle, J. (2005) Native C-reactive protein increases whereas

modified C-reactive protein reduces atherosclerosis in apolipoprotein E-knockout mice. *Circulation*. **112**, 1016–23

94. Potempa, L. a., Yao, Z.-Y., Ji, S.-R., Filep, J. G., and Wu, Y. (2015) Solubilization and purification of recombinant modified C-reactive protein from inclusion bodies using reversible anhydride modification. *Biophys. Reports*. **1**, 18–33

95. PubMed search for "C-reactive Protein" in title. (2017)

96. Volanakis, J. E., and Wirtz, K. W. A. (1979) Interaction of C-reactive protein with artificial phosphatidylcholine bilayers. *Nature*. **281**, 155–157

97. Agrawal, A., Hammond, D. J., and Singh, S. K. (2010) Atherosclerosis-related functions of C-reactive protein. *Cardiovasc. Hematol. Disord. Drug Targets*. **10**, 235–240

98. Inoshita, M., Numata, S., Tajima, A., Kinoshita, M., Umehara, H., Nakataki, M., Ikeda, M., Maruyama, S., Yamamori, H., Kanazawa, T., Shimodera, S., Hashimoto, R., Imoto, I., Yoneda, H., Iwata, N., and Ohmori, T. (2016) A significant causal association between C-reactive protein levels and schizophrenia. *Sci. Rep.* **6**, 26105

99. Miller, B. J., Culpepper, N., and Rapaport, M. H. (2014) C-reactive protein levels in schizophrenia: a review and meta-analysis. *Clin. Schizophr. Relat. Psychoses*. **7**, 223–30

100. Kravitz, M. S., Pitashny, M., and Shoenfeld, Y. (2005) Protective molecules- C-reactive protein (CRP), serum amyloid P (SAP), pentraxin3 (PTX3), mannose-binding lectin (MBL), and apolipoprotein A1 (Apo A1), and their autoantibodies: prevalence and clinical significance in autoimmunity. *J. Clin. Immunol.* **25**, 582–591

101. Szalai, A. J. (2004) C-reactive protein (CRP) and autoimmune disease: facts and conjectures. *Clin.Dev.Immunol.* **11**, 221–226

102. Du Clos, T. W., Zlock, L. T., and Rubin, R. L. (1988) Analysis of the binding of C-reactive protein to histones and chromatin. *J. Immunol.* **141**, 4266–4270

103. Habersberger, J., Strang, F., Scheichl, A., Htun, N., Bassler, N., Merivirta, R. M., Diehl, P., Krippner, G., Meikle, P., Eisenhardt, S. U., Meredith, I., and Peter, K. (2012) Circulating microparticles generate and transport monomeric C-reactive protein in patients with myocardial infarction. *Cardiovasc. Res.* **96**, 64–72

104. Eisenhardt, S. U., Habersberger, J., Murphy, A., Chen, Y. C., Woollard, K. J., Bassler, N., Qian, H., von zur Muhlen, C., Hagemeyer, C. E., Ahrens, I., Chin-Dusting, J., Bobik, A., Peter, K., Kevin, J., Bassler, N., Qian, H., Muhlen, C. Von,

Hagemeyer, C. E., Ahrens, I., Chin-Dusting, J., Bobik, A., Peter, K., Woollard, K. J., Bassler, N., Qian, H., von Zur Muhlen, C., Hagemeyer, C. E., Ahrens, I., Chin-Dusting, J., Bobik, A., and Peter, K. (2009) Dissociation of pentameric to monomeric C-reactive protein on activated platelets localizes inflammation to atherosclerotic plaques. *Circ. Res.* **105**, 128–137

105. Chirco, K. R., Whitmore, S. S., Wang, K., Potempa, L. A., Halder, J. A., Stone, E. M., Tucker, B. A., and Mullins, R. F. (2016) Monomeric C-reactive protein and inflammation in age-related macular degeneration. *J. Pathol.* **240**, 173–183

106. Volanakis, J. E., and Narkates, A. J. (1981) Interaction of C-reactive protein with artificial phosphatidylcholine bilayers and complement. *J. Immunol.* **126**, 1820–1825

107. Volanakis, J. E. (1982) Complement activation by C-reactive protein complexes. *Ann. New York Acad. Sci.* **389**, 235–250

108. Li, H.-Y. Y., Wang, J., Meng, F., Jia, Z.-K. K., Su, Y., Bai, Q.-F. F., Lv, L.-L. L., Ma, F.-R. R., Potempa, L. A., Yan, Y.-B. Bin, Ji, S.-R. R., and Wu, Y. (2016) An intrinsically disordered motif mediates diverse actions of monomeric C-reactive protein. *J. Biol. Chem.* **291**, 8795–8804

109. Goda, T., and Miyahara, Y. (2016) Engineered zwitterionic phosphorylcholine monolayers for elucidating multivalent binding kinetics of C-reactive protein. *Acta Biomater.*

110. Greenberg, M. E., Li, X.-M., Gugiu, B. G., Gu, X., Qin, J., Salomon, R. G., and Hazen, S. L. (2008) The lipid whisker model of the structure of oxidized cell membranes. *J. Biol. Chem.* **283**, 2385–96

111. Blair, D., and Dufresne, E. The Matlab Particle Tracking Code Repository. *Available online*. [online] http://site.physics.georgetown.edu/matlab (Accessed June 10, 2014)

112. Crocker, J. C., and Grier, D. G. (1996) Methods of digital video microscopy for colloidal studies. *J. Colloid Interface Sci.* **179**, 298–310

113. Sorre, B., Callan-Jones, A., Manneville, J.-B., Nassoy, P., Joanny, J.-F., Prost, J., Goud, B., and Bassereau, P. (2009) Curvature-driven lipid sorting needs proximity to a demixing point and is aided by proteins. *Proc. Natl. Acad. Sci. U. S. A.* **106**, 5622–5626

114. Larson, B. T., Sochacki, K. a, Kindem, J. M., and Taraska, J. W. (2014) Systematic spatial mapping of proteins at exocytic and endocytic structures. *Mol. Biol. Cell*. **25**, 2084–93

115. Barg, S., Knowles, M. K., Chen, X., Midorikawa, M., and Almers, W. (2010) Syntaxin clusters assemble reversibly at sites of secretory granules in live cells. *Proc. Natl. Acad. Sci. U. S. A.* **107**, 20804–20809

116. Peter, B. J., Kent, H. M., Mills, I. G., Vallis, Y., Butler, P. J. G., Evans, P. R., and McMahon, H. T. (2004) BAR domains as sensors of membrane curvature: the amphiphysin BAR structure. *Science (80-.).* **303**, 495–499

117. Vanni, S., Vamparys, L., Gautier, R., Drin, G., Etchebest, C., Fuchs, P. F. J., and Antonny, B. (2013) Amphipathic lipid packing sensor motifs: Probing bilayer defects with hydrophobic residues. *Biophys. J.* **104**, 575–584

118. Hatzakis, N. S., Bhatia, V. K., Larsen, J., Madsen, K. L., Bolinger, P.-Y., Kunding, A. H., Castillo, J., Gether, U., Hedegård, P., and Stamou, D. (2009) How curved membranes recruit amphipathic helices and protein anchoring motifs. *Nat. Chem. Biol.* **5**, 835–841

119. Madsen, K. L., Bhatia, V. K., Gether, U., and Stamou, D. (2010) BAR domains, amphipathic helices and membrane-anchored proteins use the same mechanism to sense membrane curvature. *FEBS Lett.* **584**, 1848–1855

120. Mori, S., Nakata, Y., and Endo, H. (1991) Involvements of fibronectin and lysophosphatidylcholine for selective binding of C-reactive protein. *Cell. Mol. Biol.* **37**, 421—431

121. Shrive, A. K., Cheetham, G. M., Holden, D., Myles, D. A., Turnell, W. G., Volanakis, J. E., Pepys, M. B., Bloomer, A. C., and Greenhough, T. J. (1996) Three dimensional structure of human C-reactive protein. *Nat. Struct. Biol.* **3**, 346–354

122. Sorre, B., Callan-Jones, A., Manzi, J., Goud, B., Prost, J., Bassereau, P., and Roux, A. (2012) Nature of curvature coupling of amphiphysin with membranes depends on its bound density. *Proc. Natl. Acad. Sci. U. S. A.* **109**, 173–178

123. McMahon, H. T., and Gallop, J. L. (2005) Membrane curvature and mechanisms of dynamic cell membrane remodelling. *Nature*. **438**, 590–596

124. Miller, S. E., Mathiasen, S., Bright, N. A., Pierre, F., Kelly, B. T., Kladt, N., Schauss, A., Merrifield, C. J., Stamou, D., Honing, S., and Owen, D. J. (2015) CALM regulates clathrin-coated vesicle size and maturation by directly sensing and driving membrane curvature. *Dev. Cell*. **33**, 163–175

125. Ying, S. C., Gewurz, H., Kinoshita, C. M., Potempa, L. a, and Siegel, J. N. (1989) Identification and partial characterization of multiple native and neoantigenic epitopes of human C-reactive protein by using monoclonal antibodies. *J. Immunol.* **143**, 221–228

126. Potempa, L. A., Siegel, J. N., Fedel, B. A., Potempa, R. T., and Gewurz, H. (1987) Expression, detection and assay of a neoantigen (Neo-CRP) associated with a free, human C-reactive protein subunit. *Mol. Immunol.* **24**, 531–541

127. Heuertz, R. M., Schneider, G. P., Potempa, L. A., and Webster, R. O. (2005) Native and modified C-reactive protein bind different receptors on human neutrophils. *Int. J. Biochem. Cell Biol.* **37**, 320–35

128. Mukherjee, S., Soe, T. T., and Maxfield, F. R. (1999) Endocytic sorting of lipid analogues differing solely in the chemistry of their hydrophobic tails. *J. Cell Biol.* **144**, 1271–1284

129. Sundh, M., Manandhar, M., Svedhem, S., and Sutherland, D. S. (2011) Supported lipid bilayers with controlled curvature via colloidal lithography. *IEEE Trans. Nanobioscience*. **10**, 187–193

130. Agheli, H., and Sutherland, D. S. (2006) Nanofabrication of polymer surfaces utilizing colloidal lithography and ion etching. *IEEE Trans. Nanobioscience*. **5**, 9–14

131. Lamers, E., Frank Walboomers, X., Domanski, M., te Riet, J., van Delft, F. C. M. J. M., Luttge, R., Winnubst, L. A. J. A., Gardeniers, H. J. G. E., and Jansen, J. A. (2010) The influence of nanoscale grooved substrates on osteoblast behavior and extracellular matrix deposition. *Biomaterials*. **31**, 3307–3316

132. Simons, K., and van Meer, G. (1988) Lipid sorting in epithelial cells. *Biochemistry*. **27**, 6197–6202

133. Leventis, P. A., and Grinstein, S. (2010) The Distribution and Function of Phosphatidylserine in Cellular Membranes. *Annu. Rev. Biophys. Vol 39*. **39**, 407–427

134. Lim, J. Y., and Donahue, H. J. (2007) Cell sensing and response to micro- and nanostructured surfaces produced by chemical and topographic patterning. *Tissue Eng.* **13**, 1879–1891

135. Fozdar, D. Y., Lee, J. Y., Schmidt, C. E., and Chen, S. (2010) Hippocampal neurons respond uniquely to topographies of various sizes and shapes. *Biofabrication*. **2**, 35005

136. Chevallet, M., Luche, S., and Rabilloud, T. (2006) Silver staining of proteins in polyacrylamide gels. *Nat. Protoc.* **1**, 1852–1858

137. Wayne Wray, Teni Boulikas, Virginia P. Wray, R. H. (1981) Silver staining of proteins in polyacrylamide gels. *Nat. Protoc.* **118**, 197–203

APPENDIX A: SUPPORTED LIPID BILAYER ON NANOPARTICLE PATTERNED SUBSTRATE

This protocol is a detailed version (with troubleshooting tips) of the one outlined by Black, *et al* (8).

Detailed instructions

Preparation and Supplies Needed

1. Use an 8 well chambered coverglass that has been pre-cleaned in advance by doing the following (#1.5 coverglass is preferred if doing sensitive assays due to better microscope images; #1 coverglass is less expensive – be consistent within an experiment):
    a. Cover with 0.1% SDS in a beaker - soak for 1 hour (usually 4-6 coverglass plates)
    b. Pour off SDS and cover with 1% Bleach solution in a beaker - soak overnight
    c. Pour off bleach and change solution to Millipore water (make sure it is covering the plates). Rinse 2-3 times with water. This is what they will be stored in until an experiment is performed.
2. Use lipids (PC, PS, etc.) that have been prepared at DU by the following method:
    a. Lipids and dye labeled DHPE are combined with percent by mole. Total aim should be 250 nanomoles. Using the molarity (M) of PC, PS, or dye labeled (MB or TR) DHPE calculate the μL of each to add to the vials.
    b. Normally 6-8 vials are made at a time. Cover with foil and label each vial on the sides and top.

c. Glass syringes that are used with chloroform are not to be used with anything else (the syringes are labeled “Heather Syringe” or for S.P.T. only – SPT are NOT to be used with red lipids).
d. Under the hood, measure out appropriate amounts for each dye/lipid, going from smallest to largest volume. Rinse syringe 5+ times with chloroform between/after use. Using the largest volume, swirl vial to mix lipids.
e. Place open vials in vacuum, seal, and make sure hose path is correct, turn on and wait for bubble noise to stop, reposition stop-cock to create vacuum. Leave overnight. Clean up lipid stock by quickly blowing solution with argon or nitrogen to remove any oxygen from stock solution. Screw on lid and wrap with electrical tape.
f. Turn off/remove vials from vacuum. Cover lipids with nitrogen. Screw on lid and store in freezer.

3. Nanoparticles (if applicable) are found in the refrigerator – we usually use red fluorescent polystyrene fluorospheres (Invitrogen)
4. Protein (C1q or CRP) and applicable antibodies if not using labeled protein
5. Buffers/Solutions:
    a. 30 mM PIPES, 2 mM CaCl2, 140 mM NaCl, pH 6.4
    b. Hellmanex (2% by volume)

Experiment Day Procedure

Note: Plan out 8-well grid before doing experiment (or while soaking with Hellmanex)

All experiments should be done with a directional indicator on the wells. The #1 plates have the word “LAB” on one side that you can place in the upper left. The #1.5 plates have a notch that can be placed on the left.

LAB				
	1	3	5	7
	2	4	6	8

1. Using a Kim wipe or paper towel, dry off the 8 well chambered coverglass
2. Add 100 µL of Hellmanex to each well, cover with lid and let sit 1 hour (at R.T.)
3. If doing nanoparticles:
    a. Dilute with PIPES buffer (see concentrations below)
        i) Optional bath sonication for 15 minutes after 1st dilution to break up clumps as needed
        ii) 40 nm size dilute 1 µL with 999 µL (10^3), and sonicate for 15 min, then dilute 1 µL of 10^3 solution with 999 µL of PIPES again (10^6 dilution total)
        iii) 100 nm size dilute 1 µL with 999 µL (10^3), and sonicate for 15 min, then dilute 100 µL of 10^3 solution with 900 µL of PIPES again (10^4 dilution total).
        iv) 500 nm size dilute 1 µL with 999 µL (10^3),
    b. Empty wells using 100 µL pipette

c. Rinse 3 times with 100 μL of PIPES buffer
d. Add 100 μL of nanoparticle solutions, cover with foil and incubate at r.t. for 30 minutes

4. Lipids
    a. Prepare each lipid solution by adding 2 mL (or 2000 μL) of PIPES buffer to each lipid mixture vial that was prepared above (vacuum, nitrogen, etc.)
    b. Sonicate for 5 minutes with the probe sonicator on "2" setting (sand probe lightly with sandpaper if it has not been done in a while, and clean with ethanol before each use)
    c. Empty wells using 100 μL pipette (removing solution from wells, but leaving nanoparticles)
    d. Add 100 μL of appropriate lipids to each well.
    e. Cover with foil and incubate at 37 °C for 1 hour
5. Proteins (note if not using proteins, follow step c to remove liposomes before imaging)
    a. Thaw in ice bucket
    b. Calculate amount of protein to add to each well to get desired concentration: either labeled (different concentration) or purchased protein.
    c. Rinse 3 times with 100 μL of PIPES buffer (adding lipids first, then remove; the wells need to stay wet). This should remove any liposomes floating in the mixture.

d. Add predetermined amount of protein and incubate for 1 hour at r.t. (Aml does CRP for 2 hours at 37 °C; some proteins, can be incubated for 10-15 minutes)

e. If using antibodies: pre-incubate primary and secondary together in 1:1000 ratios for 30 minutes (covered with foil at r.t.)

f. Add 100 µL of pre-incubated primary and secondary antibody to each well. Cover with Foil and incubate for 30 minutes.

6. Image on Confocal or TIRF microscopes. Recording settings as needed.

7. Putting data into folders for each well is useful. Name files with contents of well for future reference. The illustrations below show how different students number the wells. Whatever you do, be consistent!

Carrie:

1	3	5	7
2	4	6	8

Aml:

8	7	6	5
4	3	2	1

Alan:

1	2	3	4
5	6	7	8

Troubleshooting and notes by steps

1. Cleaning plates:
    a. Plates should be used within 2 weeks of cleaning or a small amount of sodium azide to the water should be added to prevent contamination with bacteria.
2. Hellmanex:
    a. Do not keep Hellmanex on for more than 1 hour, it will start to dissolve the glue and cause the well to leak/break.
    b. If a well looks empty after the 1 hour, it most likely had a leak to begin with. Fill it with 100 µL of buffer and see if it empties out. If it does not stay full, you cannot use that well for the experiment.
3. Nanoparticles:
    a. The first dilution of NPs (10^3) can be reused if stored in the refrigerator and shaken gently to resuspend prior to the second dilution.
    b. Do not keep foil on the tube when bath sonicating, the foil will break up with the sonication. Bath sonication is optional. Too much bath sonication appears to break up NPs and cause problems.
    c. NPs can be incubated for a longer period of time if needed, it will just increase the number of NPs that settle on the surface.
    d. Adding NPs and lipids at the same time causes NP islands to be formed above and below lipids.

e. An older batch of 100 nm red NPs was the reconstituted, so if using, the second dilution works best at 30 µL of the 10^3 solution with 970 µL of PIPES.

4. Lipids:
    a. Lipid incubation time can be up to 2-3 hours at 37 °C.
    b. Incubating lipids at room temperature results in non-fluid bilayers.
    c. Failure to wash three times after lipid incubation keeps liposomes on the surface.
    d. Care should be taken when washing to only place the tip in one corner of the well and to keep the tip from touching the bottom of the coverslip (tip should be in the buffer).
5. Protein:
    a. If the protein is in the freezer, be sure to allow at least 30 minutes prior to the end of lipid incubation to thaw it on ice.
    b. If using antibodies, pre-incubate when 30 minutes are left for protein incubation.
6. Imaging:
    a. If there is extra time before scheduled imaging, finished coverslips can be stored covered with foil at 37 °C or room temperature for 1-2 hours.
    b. Multiple channels should be imaged on the confocal sequentially by line (not simultaneously).

Quick Reference

Experimental Date: _____

Plan: _____

LAB				
	Well #:___	Well #:___	Well #:___	Well #:___
	Well #:___	Well #:___	Well #:___	Well #:___

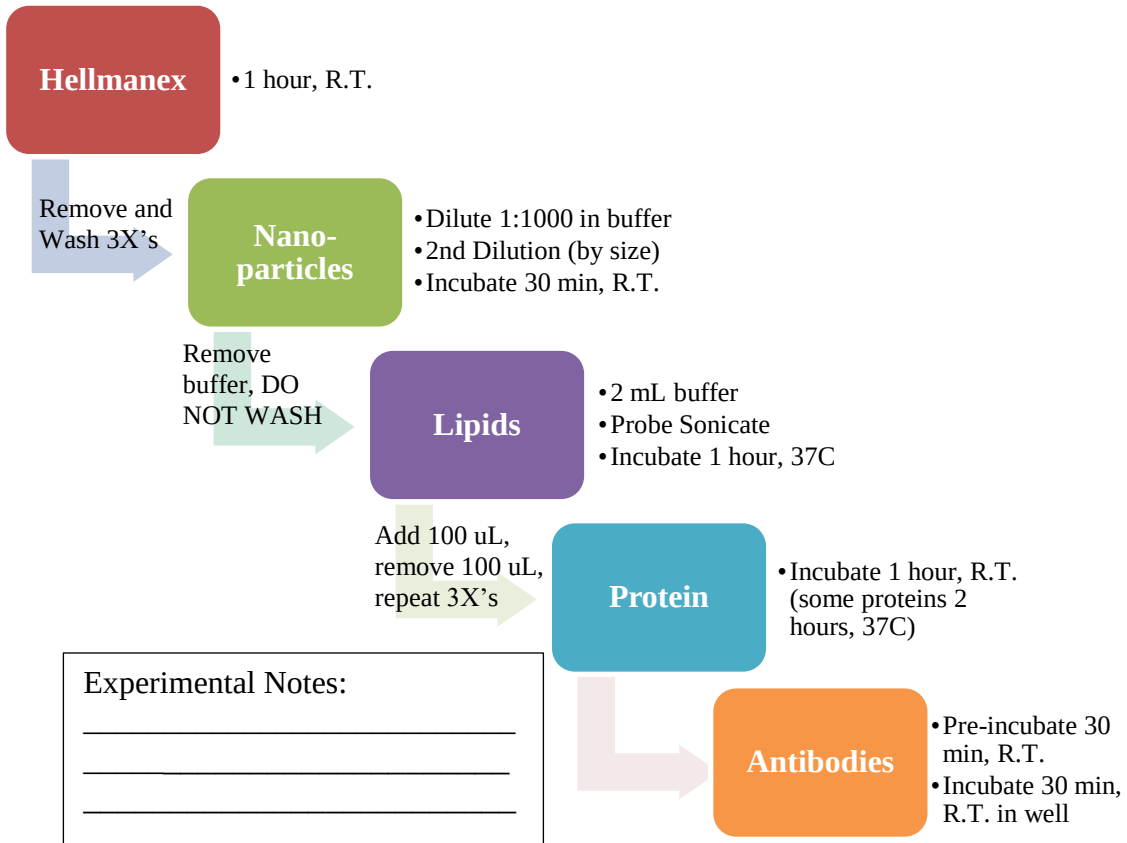

Experimental Notes:

_____

_____

_____

_____

_____

_____

_____

_____

_____

APPENDIX B: FRAP DATA ANALYSIS

This is a detailed protocol for the correction and analysis for Fluorescence Recovery after Photobleaching (FRAP) data from the confocal microscope and was modified from a protocol written by Alec Feuerbach.

Correcting for overall photobleaching

1. Open FRAP image (.oib from Confocal; if saved on newer Confocal as .oir file, convert to .oib in Fluoview software) in ImageJ (http://imagej.nih.gov/ij/)
2. Click on the ROI to display it or if it is not displayed, create an ROI where the bilayer was bleached.

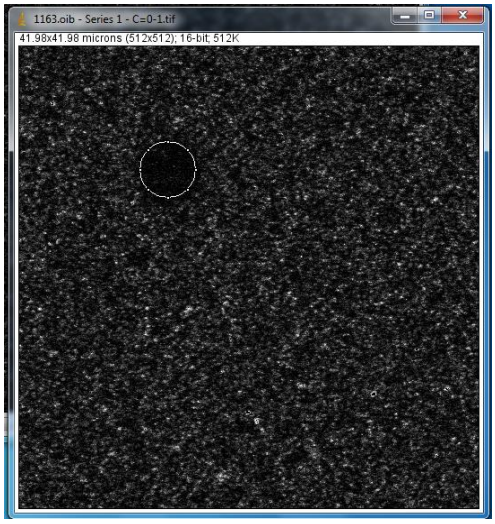

3. Collect intensity data for the FRAP ROI over the whole series by clicking the following in the “ROI Manager” window:
    a. More
    b. Multi-Measure
    c. Checked boxes for “Measure all slices” and “One row per slice”
    d. OK

e. Results appear in a new window

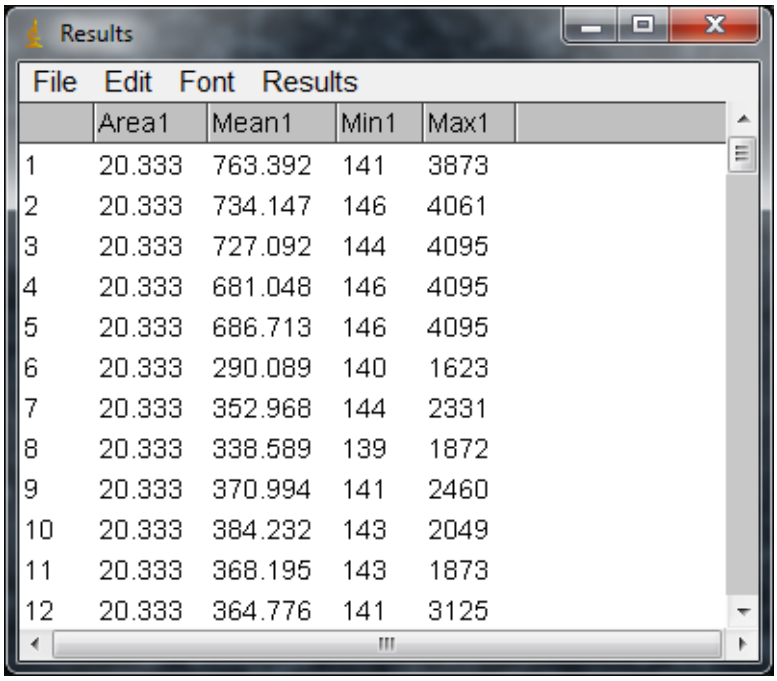

	Area1	Mean1	Min1	Max1
1	20.333	763.392	141	3873
2	20.333	734.147	146	4061
3	20.333	727.092	144	4095
4	20.333	681.048	146	4095
5	20.333	686.713	146	4095
6	20.333	290.089	140	1623
7	20.333	352.968	144	2331
8	20.333	338.589	139	1872
9	20.333	370.994	141	2460
10	20.333	384.232	143	2049
11	20.333	368.195	143	1873
12	20.333	364.776	141	3125

4. Transfer data to Excel:

   a. Open Excel

   b. In the Results window in ImageJ do:

      i. Edit

      ii. Copy

   c. Go to cell D3 and Paste

   d. Fill out the D2-H2 cells with the appropriate heading and write "FRAP Data" in D1.

	A	B	C	D	E	F	G	H
1				FRAP Data				
2				Slice	Area	Mean	Min	Max
3				1	81.334	438.585	225	1886

5. In ImageJ, move the ROI to another region away from the bleached area in order to measure the background intensity/bleaching

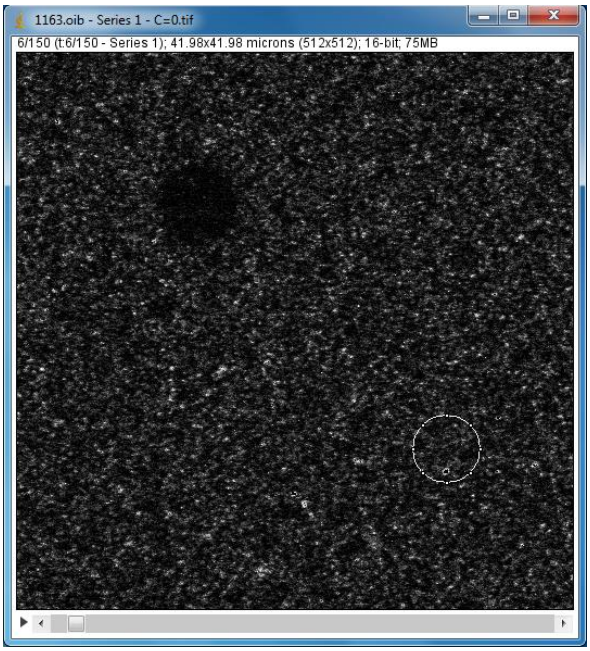

6. Click “Add” in the ROI Manager to add the region of interest that you want to measure and select the new ROI before measuring the ROI.
7. In the “Results” window do:
    a. Edit -> Select All
    b. Edit -> Clear
8. Repeat steps 3 and 4, with the exception of pasting the data in J3 and putting the title “Background ROI” in J1.

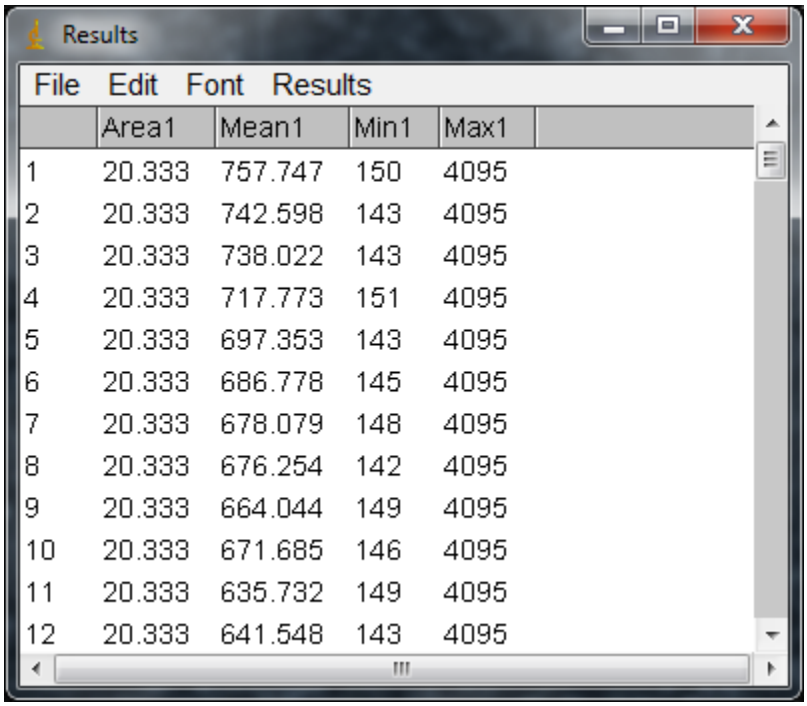

	Area1	Mean1	Min1	Max1
1	20.333	757.747	150	4095
2	20.333	742.598	143	4095
3	20.333	738.022	143	4095
4	20.333	717.773	151	4095
5	20.333	697.353	143	4095
6	20.333	686.778	145	4095
7	20.333	678.079	148	4095
8	20.333	676.254	142	4095
9	20.333	664.044	149	4095
10	20.333	671.685	146	4095
11	20.333	635.732	149	4095
12	20.333	641.548	143	4095

9. The excel spreadsheet should now look like this along the top:

	A	B	C	D	E	F	G	H	I	J	K	L	M	N
1				FRAP Data						Background ROI				
2				Slice	Area	Mean	Min	Max		Slice	Area	Mean	Min	Max
3				1	81.334	438.585	225	1886		1	81.334	425.542	219	1383
4				2	81.334	433.856	231	1959		2	81.334	423.342	227	1516

10. Get a photobleaching correction value for the background (random) ROI by dividing the intensity of the first slice by each slice intensity (in cell P3, the equation =$L$3/L3 is entered and dragged down the column to fill in the equation). Numbers should start with 1 and get larger.

	I	J	K	L	M	N	O	P	Q	R	S
1		Background ROI									
2		Slice	Area	Mean	Min	Max		Bkgrnd Photobleach Correction Value			
3		1	81.334	425.542	219	1383		=$L$3/L3			
4		2	81.334	423.342	227	1516		1.005197			
5		3	81.334	418.049	215	1458		1.017924			

11. In A1 type “Corrected FRAP Data” and in A2 type “Time (sec)”

    a. In ImageJ, find the frame interval by going to Image -> Properties

b. In Excel, in cell A3 use the formula =(D3-# of frames to activation)*(frame interval). Note the # of frames to activation is the preactivation +1. In the case of a preactivation of 3, the number used is 4. The lowest intensity will line up with Time= 0.

c. Drag to fill formula

	A	B	C	D	E	F
1	Corrected FRAP Data			FRAP Data		
2	Time (sec)			Slice	Area	Mean
3	=(D3-4)*1.3			1	81.334	438.585
4	-2.6			2	81.334	433.856
5	-1.3			3	81.334	431.833
6	0			4	81.334	275.38
7	1.3			5	81.334	302.175

12. In B2, type “Corrected Avg Intensity” (or Mean)

13. Multiply the average (mean) intensity of each slice from the FRAP ROI (Column F) by the Correction value for that slice (Column P). To do this B3 will have =F3*P3. Drag/fill this formula for all slices. This should give a corrected value for bleaching that occurs on the entire image while doing long periods of time for FRAP.

	A	B	C	D
1	Corrected FRAP Data			FRAP Dat
2	Time (sec)	Corrected Avg Intensity		Slice
3	1.3	=F3*P3		
4	2.6	436.1106386		
5	3.9	439.5730608		

	A	B	C	D	E	F	G	H	I	J	K	L	M	N	O	P	Q
1	Corrected FRAP Data			FRAP Data						Background ROI							
2	Time (sec)	Corrected Avg Intensity		Slice	Area	Mean	Min	Max		Slice	Area	Mean	Min	Max		Bkgrnd Photobleach	
3	1.3	=F3*P3		1	81.334	438.585	225	1886		1	81.334	425.542	219	1383		1	
4	2.6	436.1106386		2	81.334	433.856	231	1959		2	81.334	423.342	227	1516		1.005197	
5	3.9	439.5730608		3	81.334	431.833	219	1999		3	81.334	418.049	215	1458		1.017924	

14. Save and Copy/Paste this data into a GraphPad Prism XY plot.

Plotting Recovery Curves and Calculating Diffusion Coefficients

The directions in this section are for using GraphPad Prism to fit the following equations for fitting FRAP data and calculating diffusion coefficients (8).

$$F(t) = F_0 + (F_\infty - F_0) * (1 - e^{-kt})$$

$$D = \left(\frac{w^2}{4\tau_{half}}\right)\gamma_D$$

$$\tau_{half} = \frac{\ln 2}{k}$$

Where F_0 is the initial fluorescence and F_∞ is the fluorescence at equilibrium. K is the rate constant and t is time in seconds. D is the diffusion coefficient in $\mu m^2/s$. γ_D is defined as 0.88 for a circular beam and τ_{half} is the time at 50% recovery. For the experimental data processed here *w* is the radius of the bleaching region of interest (ROI) in μm.

The first step is to normalize the corrected data in the XY data table in GraphPad Prism. To do this, click on the analyze button from the menu along the top and select normalize. Define 0% as the smallest value and 100% as the first value. Choose to present data as fractions.

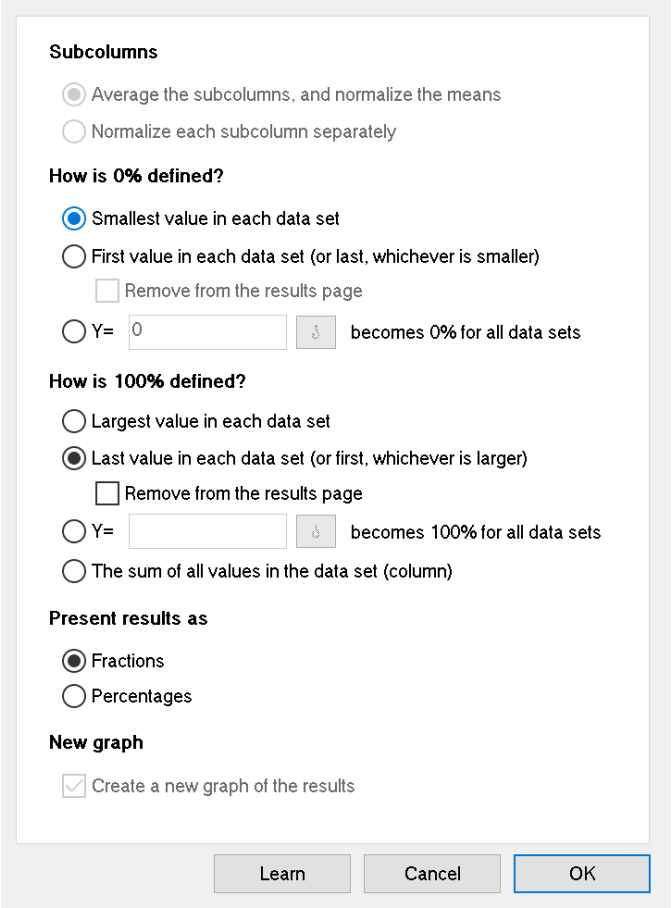

Next calculate the Mean and SEM of the normalized data by selecting Analyze and then Row Stats.

In the Analysis box click: fit with non-linear regression curve and select the “Diffusion Coefficient from FRAP recovery curve” equation or add the following as a custom equation:

Equation: Y=Y0 + (Plateau-Y0)*(1-exp(-K*x))

Default Constraints: K must be greater than 0

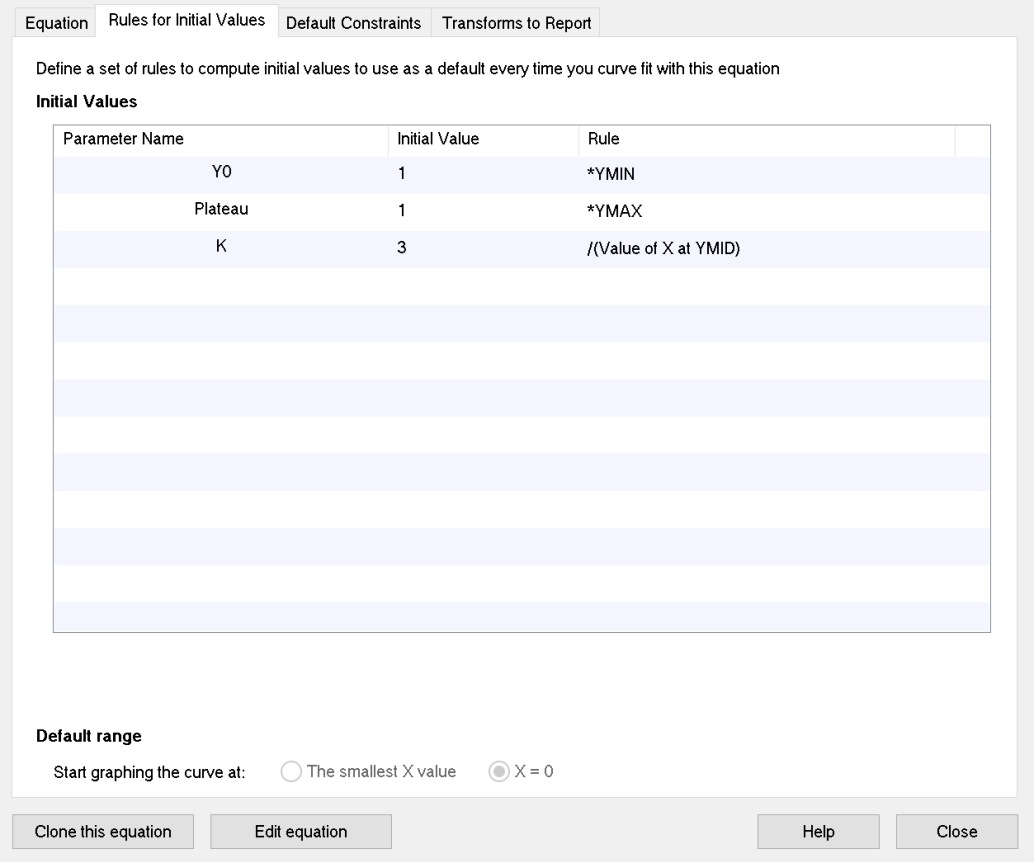

The transforms to report section is where the diffusion constant calculation will need to be adjusted for different bleaching ROI sizes. The table below gives some examples of confocal zooms with their corresponding pixel resolutions and different radii.

Zoom with 100X objective	nm/pixel	Radius for ROI
1X	240	15.5 μm for 125x125 pixel tornado
2X	124	7.75 μm for 125x125 pixel tornado
2.5X	100	6.25 μm for 125x125 pixel tornado 2.486 μm for 50x50 pixel tornado
3X	82	5.17 μm for 125x125 pixel tornado

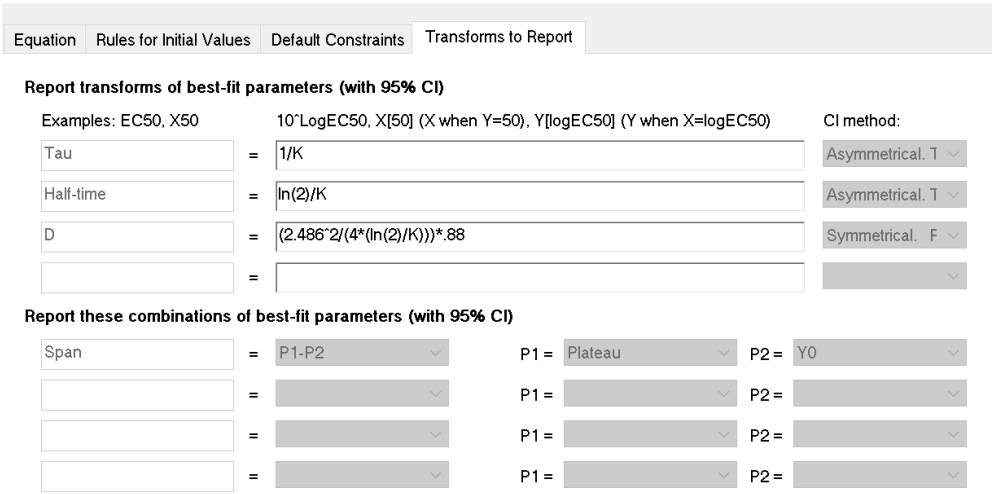

When fitting the data, if X values greater than 0 are included in the fit, there will be an error. This can be fixed by adjusting the range, as shown below.

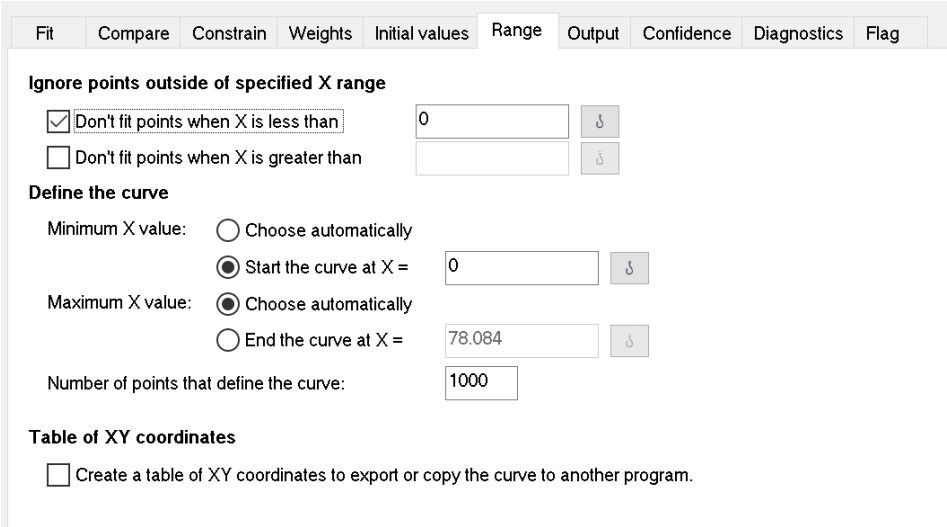

Diffusion constants can now be seen in the results and a corresponding graph with the linear fit will be in the graphs section.

APPENDIX C: NON-DENATURING PAGE AND SILVER STAIN PROTOCOL

The non-denaturing polyacrylamide gel electrophoresis protocol has been modified from standard Laemmli conditions (68). The silver stain protocol was taken from the laboratory notebook of Kathryn Palma, a former student who worked in Dr. Knowles' lab at the University of Denver. Nature protocols has two journal articles for silver stain protocol with detailed explanations for the steps (136, 137).

Non-Denaturing PAGE

1/20th SDS

Running Gel		10.0%
(mL)	**(µL)**	
Combine the following:		
4.1667	4166.7	30% Acrylamide
3.1250	3125.0	1.5 M Tris-HCl pH 8.8
0.0063	6.25	10% SDS
5.0646	5064.6	(to add up to 12.5mL) Water
0.1250	125.0	10% APS (Ammonium Persulfate)
Swirl to Mix		
0.0125	12.5	100% TEMED
Swirl to Mix		
Pour & let set 10-20 min (put thin layer of ethanol on top)		

Stacking Gel		3.2%
(mL)	**(µL)**	
0.2667	266.7	30% Acrylamide
0.3125	312.5	1 M Tris-HCl pH 6.8
0.0013	1.25	10% SDS
1.8646	1864.6	(to add up to 2.5mL) Water
0.0500	50.0	10% APS (Ammonium Persulfate)
0.0050	5.00	100% TEMED
Swirl to Mix		
Pour & let set 20 min		

Store in Ziploc bags in fridge, wrapped in paper towels, soaked in 1.5 M Tris-HCl pH 8.8 buffer

Silver Stain of Native PAGE Procedure

Make the following solutions (filling to total volume with diH2O):

- Fixing Solution (50 mL total)
    - 25 mL of Methanol (final = 50%)
    - 2.5 mL of Acetic Acid (final = 5%)
    - 25 µL of 37% Formaldehyde (final = 0.0185%)
- 50% Methanol (2 × 50 mL total, 25 mL of methanol in each)
- 10% Sodium Thiosulfate ($Na_2S_2O_3$)-need 150 µL minimum (good for 1 week)
    - equivalent of 10 g/ 100 mL or 10 µg/ 100 µL
    - _____ mg x 10 = _____ µL
- Sensitizing Solution (25 mL total)
    - 50 µL of 10% Sodium thiosulfate (final = 0.02%)
- Silver Stain (25mL total)
    - 50 mg Silver Nitrate – $AgNO_3$ (final = 0.2%)
- Developer (25mL total)
    - 50 µL of 32% Formaldehyde (final = 0.074%)
    - 1.5 g Sodium Carbonate (Na_2CO_3) (final = 6%)
    - 100µL of 10% Sodium Thiosulfate (Final = 0.04%
- Stopping Solution (50 mL total)
    - 25 mL Methanol (final = 50%)
    - 2.5 mL Acetic Add (final = 5%)

Use 25mL for each step below (except step 8):

1. Fix (rock in fixing solution) 2×15 min
2. Wash 3×8 min with 50% Methanol
3. Sensitize 60 sec
4. Wash 2×20 sec diH2O
5. Silver stain for 30 min

► Place waste in appropriate container

6. Wash 2×30 sec diH2O
7. Develop until bands show
8. Add stopping solution (50mL)

   Swirl until no more bubbles
9. Wash 10 min with 50% Methanol
10. Final rinse diH2O
11. Image/scan and save file

APPENDIX D: COLOCALIZATION MATLAB ANALYSIS

The steps for MATLAB analysis of microscopy images for colocalization are outlined below. This chapter also includes directions for removing non-cellular nanoparticles when looking for colocalization between nanoparticles and cell membranes. The MATLAB code used for the data analysis is included at the end. The majority of this code was written by Dr. Michelle Knowles, Mitchell Alton, or Dr. Philip Cheney.

Data Analysis

1. Open Olympus Fluoview FV31S-SW
    a. File > Export Multiple Files
    b. Select folder create new “Exported Images” subfolder for saving files
    c. Select no overlay
    d. Output format: Raw Data Extracted, 16-bit Gray Scale, no compression
    e. This will save each image in its own folder and each channel as separate image file
2. Open MATLAB
    a. Find the folder with the image files using the window on the left side of the screen
    b. Type **run_ministk** in the command window and press enter
        i. Choose the red and green channel images
        ii. Choose the name and where to save the images

3. If needed, cut out saturated pixels:
    a. Open the folder that has the *.stk images in MATLAB (Alternatively, open a parent folder and search for .stk and then select each one with CTRL help down and then copy/paste into a new folder named “blue stacks” or “green stacks”. This is useful for large numbers of stacks to be easily processed.)
    b. Type **cutout_saturated** in the command window and press enter
    c. Choose the file that you want to remove saturated slices from
    d. Save the unsaturated image
4. Use ImageJ to concatenate all of the images from a single well for the day
    a. Open all of the stacks you want to concatenate
    b. On the ImageJ toolbox, click the Stk button and then ‘Delete Slice’ to delete the first black slice on each stack
    c. Then click the Stk button again and click concatenate and select all the open files on the window that pops up
    d. Save as > tiff
    e. Save average of the concatenated stack (to use below)
    f. Repeat Concatenation for every day of the experiment with those settings
5. To get the radial average, type the following into MATLAB (with the folder open in MATLAB), changing the red text for the file name(s) as needed (you can have more than one file in the same folder and copy/past multiple text at once).

```
g_rand=TIFFStack('WellD.100nmsputter.MB.Chol.PEG.Concat.tif');
a=make_avgradial(g_rand);
xlswrite('WellD.100nmsputter.MB.Chol.PEG.Concat.AVGradial+stdev+sterr.xls', a);
```

If you forget to change the name in the xlswrite part of the code, then you can rename it in the folder after it is saved.

Removing Non-Cell Nanoparticles from Images

1. Open oib file in ImageJ
2. File > Save As> Image Sequence (new folder for image sequence)
3. Open newly saved .tiff of CellMask (green) channel
4. File >Save As> Tiff – type 8 bit after the name
5. Image > Type> 8 bit
6. Image > Adjust > Threshold (this should highlight the cell/fluorescent regions only – the cutoff values can be adjusted in the window that pops up).
7. Edit > Selection > Create Selection (to get threshold highlighted region outlined)
8. Analyze > Tools > ROI Manager to open the ROI Manager
9. In the ROI Manager, after clicking on the cell mask image click "Add"
10. Open the Nanoparticle .tiff saved in step 2
11. Click on the ROI listed in the ROI manager so it is displayed on the image
12. If some regions that were highlighted are from the background/not clean (most likely), select the following in the ROI manager: More > Split
13. There should now be a large number of ROIs listed (usually hundreds). To find the wanted ROIs, make sure Show all and Label are both checked. This will allow you to click on the ROI you want and find it in the list. The ROIs are listed in order of left to right, top to bottom from the lowest part of the ROI. Try to select the top cell region first and then click on one ROI up above it and hold down shift. Using the mouse, scroll to the top and click on the 2nd ROI (the first should be the entire original ROI). Then hit "Delete". Continue to do this or to school

with the arrows on the keyboard and delete all the unwanted ROIs. This should leave you with 1-4 cell area ROIs.

14. Select each cell ROI (not the top one that was the original with everything) and go to: More > Or (combine)
15. The cell regions that you want to keep should now be selected in the NP channel
16. In the main menu: Edit > Clear Outside
17. File > Save as > Tiff > add “Noncell NPs removed” to the file name.
18. Delete all the ROIs left in the ROI manager after you close the images and then repeat with the other images.

MATLAB Code

run_ministk

```
function [] = run_ministk ( )

%ask for red and green channels
[redfile,redpth] = uigetfile('*.tif','Select the Red Channel');
[grnfile,grnpth] = uigetfile('*.tif','Select the Green or Blue
Channel');

%ask where to save the resulting file
[savefile,savepth] = uiputfile('*.mat','Where to save the Results');

%read in an image
a=imread([redpth,redfile]);
c=imread([grnpth,grnfile]);

%view the image, imagesc autoscales.
colormap('gray'),imagesc(a);

% filter the image, 9 is a size, filter things larger than 9 pixels,
and filter 1 or smaller
b=bpass(a, 1, 9);
colormap('gray'),imagesc(b);
colormap('gray'),image(b);
%seems to make a saturated mask like image when using beads

%use the filtered image to find regions. 100 is the threshold and 9 is
a size of feature
%you are looking for. Should be the same as above. RECORD THESE NUMBERS
IN
%YOUR NOTEBOOK!
pk=pkfnd(b, 100, 9);

%find centroids -  NOT NEEDED for colocalization routine
cnt=cntrd(b, pk, 15);

%overlay regions onto non-filtered image. Adjust the threshold to find
fewer or more
%spots.
colormap('gray'),imagesc(a);
hold on
plot(pk(:,1), pk(:,2), 'ro');
zoom

%once you like the threshold and want to cut out ministacks
%do this with both color channels so that you can check it.
cutout_red = ministk(a, pk, 24, 9);
cutout_grn = ministk(c, pk, 24, 9);
```

```
%a is the image you will be cropping, pk are the regions you would like
to crop, 24 (+1)
%is the size of images you will cut out and if spots are too close
(within 9 pixels of one
%another) you will not count either of them.

%save the file
stkwrite(cutout_red,strcat(savefile,'-red.stk'),savepth);
stkwrite(cutout_grn,strcat(savefile,'-MB.stk'),savepth);

cutout_red_avg = uint16(mean(cutout_red,3));
cutout_grn_avg = uint16(mean(cutout_grn,3));

stkwrite(cutout_red_avg,strcat(savefile,'-red-avg.stk'),savepth);
stkwrite(cutout_grn_avg,strcat(savefile,'-MB-avg.stk'),savepth);

%see what regions were kept and save them. You do NOT need to do this
with both
%image files, since the spot locations will be identical.
finalspt = keptspot(a, pk, 24, 9);
save(fullfile(savepth,savefile));

% you can view what spots were kept and what were ?too close? to others
or the edges.

colormap('gray'),imagesc(a);
hold on
plot(finalspt(:,1), finalspt(:,2), 'ro');
zoom

%Added by Carrie Moon to save image of which NPs were selected
hgexport(gcf, fullfile([savefile '-selected-NPspots.png']),
hgexport('factorystyle'), 'Format', 'png');


%% Make a radial plot of pixel intensity
% This is Mitch Alton's implementation

hold off;

[m, n]=size(cutout_grn_avg);

%finds size of the image
x=[1:n];
l=repmat(x,n,1);

%creates matrix of repeating columns of 1 through how ever many columns
%there are in the image
y=[1:m];
y';
p=repmat(y,m,1);
w=p';
```

```
%creates matrix of repeating rows
x=l-(((n-1)*0.5)+1);
y=w-(((n-1)*0.5)+1);

%makes matrixes -# to +#. Not sure how this will work with even numbers
%though
z=cutout_grn_avg(1:m,1:n);

%creates a matrix of intensities from image
[THETA,RHO,Z]=cart2pol(x,y,z);

%converts three matrixes to a three dimensional polar coordinate matrix
%G=reshape(z,1,625);
%H=reshape(RHO,1,625);

%turns matrix into a list of values
[t,I,J] = unique(RHO);
s = zeros(size(t));
frequencies = zeros(size(t));
for i = 1:max(J)
    I = find(J==i);
    s(i) = mean(Z(I));
    frequencies(i) = length(I);
end
plot(t,s)

% Save the files
radialPlot = cat(2,t,s);
hgexport(gcf, fullfile(grnpth,[savefile '-MB-radial.png']),
hgexport('factorystyle'), 'Format', 'png');
csvwrite(fullfile(grnpth,[savefile '-MB-radial.csv']), radialPlot);



[m, n]=size(cutout_red_avg);

%finds size of the image
x=[1:n];
l=repmat(x,n,1);

%creates matrix of repeating columns of 1 through however many columns
%there are in the image
y=[1:m];
y';
p=repmat(y,m,1);
w=p';

%creates matrix of repeating rows
x=l-(((n-1)*0.5)+1);
y=w-(((n-1)*0.5)+1);
```

```
%makes matrixes -# to +#. Not sure how this will work with even numbers
%though
z=cutout_red_avg(1:m,1:n);

%creates a matrix of intensities from image
[THETA,RHO,Z]=cart2pol(x,y,z);

%converts three matrixes to a three dimentional polar coordinate matrix
%G=reshape(z,1,625);
%H=reshape(RHO,1,625);

%turns matrix into a list of values
[t,I,J] = unique(RHO);
s = zeros(size(t));
frequencies = zeros(size(t));
for i = 1:max(J)
    I = find(J==i);
    s(i) = mean(Z(I));
    frequencies(i) = length(I);
end
plot(t,s)

% Save the files
radialPlot = cat(2,t,s);
hgexport(gcf, fullfile(grnpth,[savefile '-red-radial.png']),
hgexport('factorystyle'), 'Format', 'png');
csvwrite(fullfile(grnpth,[savefile '-red-radial.csv']), radialPlot);

%close
end
```

```
function out=ministk(im,rgn,sz,sepdist)
% out=ministk(im,rgn,sz)
%
% PURPOSE:  to cut out small regions of an image based on spots found
in
% the image or a corresponding image of a different color. This is used
to
% measure colocalization based on the work of Knowles and Barg in two
PNAS
% 2011 papers. Spots are found using the work of tracking routines
% available on Eric Weeks' website (Emory University) and made into
Matlab
% by Eric Dufrense.
% INPUT:
% im: image to cut from
% rgn: spots (x,y) about which regions should be cut
% sz: size of cut out (a square of sz by sz pixels)
% sepdist: is the minimum separation distance between two spots. If two
% spots are within this distance of one another, neither are counted.
%
% OUTPUT:  a sz x sz x N image array
%
% CREATED: Michelle Knowles May 2012

%if sz/2 == floor(sz/2)
%warning('sz must be even so that the spots can be centered on a pixel:
1 pixel added');
%sz = sz+1
%end

%scott's code for a mask
pix=(sz+1)/2;
dim = length(im);
nrgn = length(rgn(:,1));


%create a blank image array that you can fill
msk=zeros([sz+1,sz+1]);
%loop through all regions that locate spots in an image
for i =1:nrgn;
    x = rgn(i,1);
    y = rgn(i,2);
    %don't include regions within pix distance from the edge of the
image.
    if ((x>pix) & ((x+pix)<dim) & (y>pix) & ((y+pix)<dim))
        % don't include regions within "sepdist" pixels of another
region
        % calculate an array that contains the difference between the
        % current particle's position and all others.
        diffy=rgn(:,2)-rgn(i,2);
        diffx=rgn(:,1)-rgn(i,1);
```

```
        mag=((diffx.*diffx)+(diffy.*diffy).^0.5);
        % find all the locations in the magnitude array that are non-
zero.
        % This should remove the comparison between particle i and
itself,
        % which will always be zero.
        w = find(mag);
        mag = mag(w);
        if (min(mag) > sepdist)
          cutout = imcrop(im,[x-pix y-pix sz sz]);
          msk = cat(3, msk, cutout);
        end
    end
end

out=msk;
end
```

cutout_saturated

```
function cutout_saturated(stk)
% out=remove_sat(stk)
%
% PURPOSE:  to remove any images that have an oversaturated pixel. This
is
%used to eliminate any error when using this program if saturated
pixels
%were mistaken for spots in a previous program.
% INPUT:
% stk: stk file to find saturated pixels in
% OUTPUT:  a sz x sz x N image array
%
% CREATED: Mitch Alton 2015

%Phil's code for mask

stk=stkread;
%choose .stk file from browser
ind=find(stk>4094);
%this finds every pixel that has a brightness greater than 4094
frame=fix(ind/625)+1;
%divides the pixel number from ind by total number of pixels in one
image
%and makes it an integer. When added to 1, identifies the image number
of
%stack
x=unique(frame);
%eliminates repeating numbers
b=1:length(stk);
%creates list of numbers from 1 to however number of images is in the
%stack
b(x)=[];
%eliminates image numbers from list of numbers that have saturated
pixel
%mask=ones(size(stk));
%for index=1:size(stk);
   % listMask(1,list(1,index))=0;
%end
%we got rid of this mask
new=stk(:,:,b);
stkwrite(new);
```

make_avgradial

```
function [ avgradial_out ] = make_avgradial(imagestk)
%loop through better_colo to get a radial plot for each image, then
average
%all radial plots. Output average and standard deviation.

dims =  size(imagestk);
radial = zeros(83, dims(:,3));

for i = 1:dims(:,3)
    radial(:,i)=better_colo_V2(imagestk(:,:,i));
end
avgradial_out = zeros(83,3);
avgradial_out(:,1) = mean(radial,2);
avgradial_out(:,2) = std(radial,0, 2);
avgradial_out(:,3) = avgradial_out(:,2)/sqrt(dims(:,3));
end
```

```
function  [ radial_out ] = better_colo_V2(a)
%better_colo plots intensities of a location guided average image as a
%function of distance from the center of the image.
%Not needed at the moment but the program does this: The second half of
the
%program finds the area under the peak of the radial intensity plot. It
%does this by subtracting the area of the rectangle under the peak (the
%peak ends 3 pixels away from the center) using the mean of the data
after
%the third pixel as the height of the rectangle.
%Written by Mitch Alton on 7/1/15
%adapted for no user input and mass throughput of images by MKK
9/27/2016

%finds size of the image
[m,n]=size(a);

%creates matrix of repeating columns of 1 through however many columns
%there are in the image
x=[1:n];
l=repmat(x,n,1);

%creates matrix of repeating rows
y=[1:m];
y';
p=repmat(y,m,1);
w=p';
%makes matrixes -# to +#. Not sure how this will work with even numbers
%though
x=l-(((n-1)*0.5)+1);
y=w-(((n-1)*0.5)+1);
%creates a matrix of intensities from image
z=a(1:m,1:n);

%converts three matrixes to a three dimensional polar coordinate matrix
[THETA,RHO,Z]=cart2pol(x,y,z);

%turns matrix into a list of values
P=reshape(Z,1,[]);
H=reshape(RHO,1,[]);

%this averages the intensities (Z) for single distance (RHO) values
[plt,I,J] = unique(H);
s = zeros(size(plt));
frequencies = zeros(size(plt));
for i = 1:max(J)
    I = find(J==i);
    s(i) = mean(P(I));
    frequencies(i) = length(I);
end
radial_out = s.';
```

APPENDIX E: RESOLUTION OF TOTAL INTERNAL REFLECTION FLUORESCENCE MICROSCOPE

Total internal reflection fluorescence microscopy (TIRFm) requires a change in refractive index between the glass coverslip and the sample. The TIRFm instrument used in the Knowles Lab has two TIRF objectives (60x and 100x). There is a 1.5x zoom that can be applied through the microscope and the option of either a dual view or a 2.5x optical zoom pathway between the microscope and the camera. The following is a table compiled from micrometer measurements taken with the dual view insert at the various settings. Dual view values in the table below were divided by 2.5 to get the approximate resolution with the dual view removed and the 2.5x zoom attached.

Objective	Zoom	DualView?	nm/pixel
60	1	Yes	268.8
60	1	2.5	107.5
60	1.5	Yes	180.5
60	1.5	2.5	72.2
100	1	Yes	133.0
100	1	2.5	53.2
100	1.5	Yes	88.5
100	1.5	2.5	35.4

Steps for micrometer measurements above:

1. ImageJ
    a. Open image
    b. Add a scale bar under Analyze > Tools and then save as .jpeg
    c. Open ROI Manager (Analyze > Tools > ROI Manager)

d. Draw a rectangle over the area with the micrometer (either lower ½ if dual view in or entire image if bypass or 2.5X)
e. Click “Add” in ROI manager
f. Select the newly added ROI
g. More > Multi Plot
h. Save as a .xls

2. Excel
    a. Open (select yes) and select Save As and in dropdown select .xls again (states the current is tab delimited text), and yes to save over current file by that name
    b. Highlight columns A and B > Insert > Scatter Plot (with lines, not points)
    c. Highlight B > Conditional Formatting > Highlight cell rules > Less than > Pick value based on dips in graph (i.e. 400 or 550)
    d. Go through list and highlight in A the cells next to the ones highlighted in B. This will display an average in the lower right of the Excel window. Select the corresponding X value (pixel distance) and highlight it in orange (or do 2 cells if not a whole pixel, i.e. if the average is 5.5, then color 5 and 6). Repeat for all the dips and write the average pixel distance above the graph in individual wells.
    e. The space between the lines is 10 µm. Take each of the values above the graph for the line centers and subtract the consecutive ones from each other to get the pixel distance between the lines. Take the average of this (average pixel distance for 10 µm).

f. Use a formula to do =10000/(average pixel distance)

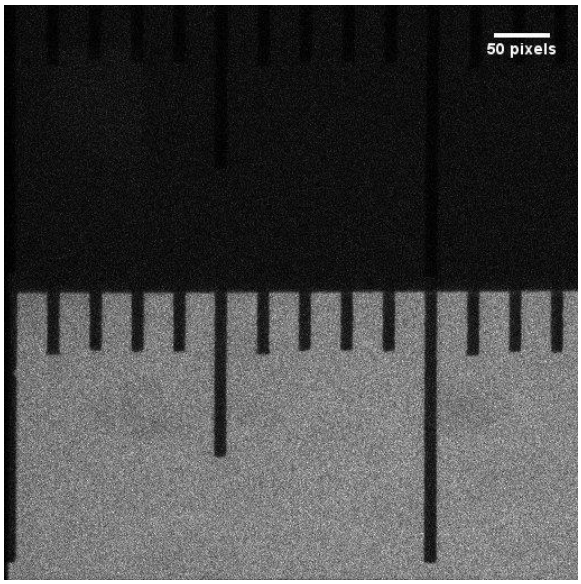

Sample micrometer image taken with the 60X TIRF objective at 1X zoom with the dual view active.

Note: The websites below contain extensive TIRF background and information:

https://www.microscopyu.com/techniques/fluorescence/total-internal-reflection-fluorescence-tirf-microscopy

and

http://www.olympusmicro.com/primer/techniques/fluorescence/tirf/tirfhome.html

APPENDIX F: DEDICATION

To those who taught me many things

From how to read to calculations for biophysical springs

To how to deal with what life brings

To those who have helped me on the way

With support and prayers for every day

To those who believed that I would

Do more than I even thought I could

To those who listened day and night

To those who reviewed a protein binding site

And who patiently looked over each rewrite

To those who answered all my questions

And offered many kind suggestions

To those who mentored me with care

To friends and family everywhere

It means so much that you have seen me through

And I dedicate this tome to you